RICE UNIVERSITY

# Synthesis and application of phosphonate scale inhibitor nanomaterials for oilfield scale control

by

**Ping Zhang**

A THESIS SUBMITTED
IN PARTIAL FULFILLMENT OF THE
REQUIREMENTS FOR THE DEGREE

**Doctor of Philosophy**

**THESIS COMMITTEE:**

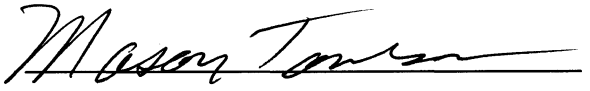

Mason B. Tomson, Professor, Chair
Civil and Environmental Engineering

Philip B. Bedient,
Herman Brown Professor
Civil and Environmental Engineering

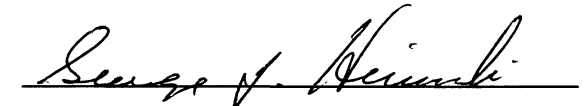

George J. Hirasaki,
A. J. Hartsook Professor
Chemical and Biomolecular Engineering

HOUSTON, TEXAS

December 2010

## ABSTRACT

In this study, several synthesis routes were adopted to prepare nanometer sized metal-phosphonate particles to expand their use in the delivery of phosphonate mineral scale inhibitors into formation porous media for oilfield scale control. An aqueous solution of calcium chloride or zinc chloride was mixed with a basic phosphonate solution to form nanometer sized particles. The physical and chemical properties of the fabricated nanomaterials and their solutions have been carefully evaluated. The obtained nanomaterial suspensions were stable for a certain period of time at 70°C in saline solutions. The nanomaterials demonstrated a good migration performance through formation porous media. Transportability was affected by both the flow velocity and the surface chemistry of the nanomaterials as well as the formation medium. The transport of these nanomaterials can be enhanced, when the formation materials were pre-flushed by surfactant solutions. The potential application of the synthesized nanomaterials for scale treatment in oilfields has been investigated by a series of laboratory squeeze simulation tests. The synthesized nanomaterials were injected into formation medium and retained on the medium surfaces. After a shut-in period, the inhibitor nanomaterials slowly released phosphonates into the produced fluid to prevent scale formation. It has been observed that the prepared nanomaterials are able to return phosphonates in a similar return profile as that of the conventional acidic pills. Moreover, the crystalline phase Ca-DTPMP nanomaterials, developed from their amorphous precursors, demonstrate a long term phosphonate return behavior

with a stable phosphonate return concentration for an extended period of time. The long term flow back performance of metal-phosphonate nanomaterials can be interpreted by their solubility product in brine solutions.

## ACKNOWLEDGEMENTS

I sincerely thank my academic advisor Dr. Mason Tomson for his tremendous guidance, support to my academic and personal life. I would like to give special thank to my thesis committee members, Dr. Philip Bedient and Dr. George Hirasaki for providing valuable insight and assistance for my thesis. Special thanks to Dr. Amy Kan for her time, effort and patience to make me take care of all the details of research. A hearty thanks to Dr. Chunfang Fan, Dr. Haiping Lu, Dr. Wei Shi, Dr. Jie Yu, Dr. Dong Shen and Dr. Gongmin Fu for their kind help to both my lab work and my life. Without them, my life will be less interesting. I also thank other members in Dr. Tomson group, Hamad, Lu, Jonathan, Jesse, Sarah, Nan and Sue for their kindness and great personality. Thanks to my friends, Bin, Annie, Sam, Jason and Steven for sharing their time with me. Last, but not least, I have to thank my parents, Mr. Desheng Zhang, M.D. and Ms. Xiaofei Wen, M.D., for their support and encouragement.

This work has been financially supported by the Rice Brine Chemistry Consortium and the National Science Foundation.

# TABLE OF CONTENTS

# LIST OF TABLES

# LIST OF FIGURES

# CHAPTER ONE
# INTRODUCTION

As oil and gas production progresses, the ratio of produced water to hydrocarbons often increases. Typically, 5 to 20 barrels of brine will be produced with one barrel of oil or gas equivalent. These brines are corrosive and tend to produce calcite or sulfate scales[1]. Along with other forms of scales, calcite (calcium carbonate) is one of the most common types of scale deposits. Precipitation of calcite in production tubing is due to pressure drop and increase in brine pH when carbon dioxide evolves to the gas phase[1, 2]. Scales often form in the formation near the perforations, in the production tubing, and on the surface of facilities. Phosphonates are widely used for scale control[3] and are referred as the threshold scale inhibitors because they prevent scale nucleation and formation at concentrations of several milligrams per liter or less. It has been confirmed by extensive laboratory and field testing that at 0.1 to 1 mg $L^{-1}$ or less, phosphonate inhibitors are often sufficient to prevent scale formation[4]. Even though the mechanism of scale inhibition is still under debate, extensive fundamental and mechanistic studies have been carried out on the topics of scale formation[5, 6], scale inhibition[6, 7], and scale inhibitor interactions and reactions with rock substrates and minerals[8-10].

The mechanism of scale inhibitors interaction with formation materials controls the placement of inhibitors in the formation and the squeeze lifetime. It has been

postulated by Kan and Tomson that[8-10] :1) at low phosphonate inhibitor concentration, inhibitor concentration is determined by a chemical sorption mechanism; 2) at high inhibitor concentration, formation of calcium-phosphonate precipitate dominates the attachment of inhibitors to calcite surface. During a squeeze treatment inhibitors are squeezed into a downhole formation so that they can precipitate with divalent cations, mostly calcium, and slowly release phosphonates into production brine fluid to prevent scale formation[8, 9, 11]. Often the squeeze treatment is an effective means to place inhibitors in hydrocarbon reservoirs[12]. However, some inhibitors may not be placed in the reservoir efficiently. In a conventional squeeze treatment, an acidic pill will dissolve metal ions from the formation that leads to rapid precipitation of inhibitor salts near the wellbore. Neutralized inhibitors can be pushed farther into the formation; they are less effective due to the weak adsorption to the rock[4]. It is desirable to be able to control the migration, placement, and return of scale inhibitors in the formation and hence the goal of this study.

The utilization of scale inhibitor precipitation treatment technology has been investigated previously by several research groups[13, 14]. It has been observed that[14-16], several parameters including the inhibitor concentration, solution pH, the presence of salt, dissolution properties of inhibitors, and binding capability with divalent metals can significantly impact the results of the precipitation treatment and the placement of inhibitors in the downhole formation, indicating that it might

be possible to design a better precipitation treatment to control inhibitor return levels than is presently used[13]. As Jordan et al. stated, compared with the adsorption treatment, the precipitation treatment greatly enhanced the squeeze performance and the precipitate solubility plays an essential role in determining the inhibitor return concentration and precipitate treatment lifetime[13, 17]. On the other hand, some modeling work regarding inhibitor squeeze performance and nucleation with divalent metals has been carried out to predict inhibitor precipitation treatment[18, 19]. Other than conventional metal-phosphonate precipitates, some novel types of inhibitor precipitates, including the enzyme activated and oil-soluble inhibitors have been fabricated for precipitate treatment[20, 21]. The major concern regarding the industrial application of precipitate squeeze treatment is the formation blockage and damage caused by the inhibitor precipitation in the near wellbore area.

Based on the above arguments, as indicated by Shen et al[22], it may be possible to fabricate a nanomaterial suspension (nanofluid) comprised of Ca-phosphonate nanoparticles and place such nanomaterials in the formation matrix for the purpose of extending squeeze life. Nanometer scaled metal-phosphonates have potential applications in industry such as sensors, catalysts, ion conductors, and optical materials[23, 24]. For oilfield scale control (Fig. 1.1), it is of value to explore the proper methods to fabricate such nanomaterials. These materials should be able to migrate deep into reservoirs and attach to the surface of the formation

rocks during the shut-in period and release phosphonates into the production water at a concentration higher than the minimum inhibitor concentration required to inhibit scale formation for a long period of time. Therefore, it is important to study the transport behavior of fabricated inhibitor nanomaterials in formation media.

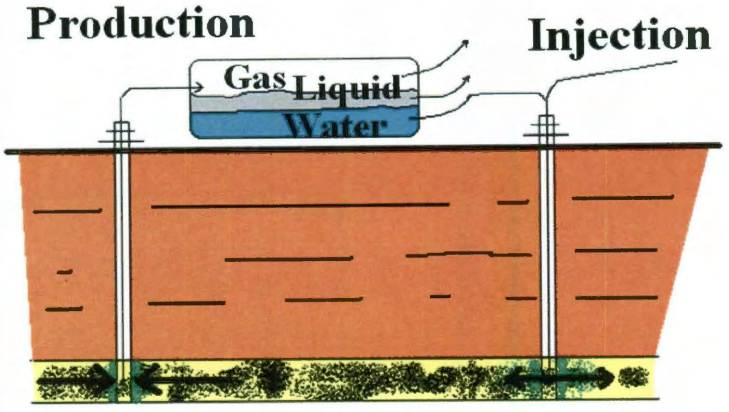


Figure 1.1. Schematic of a typical oil production site. In order to facilitate hydrocarbon production, brine or diesel is injected through the injection well into the downhole formation to maintain the pressure and to push the hydrocarbon to flow out of the production well.

Surfactant-assisted methods are widely applied in the preparation of nanometer sized materials, such as cobalt-phenylphosphonate particles[23], CdSe nanorods[25, 26], disk-shaped Co nanocrystals[27], and nanoscale zero valence iron[28]. In the process of nanoparticle synthesis, surfactants play an important role in determining the morphology and size of the products. Surfactants are able to control surface charges of particles and inhibit aggregation and attachment to surfaces by means of providing electrostatic double layer repulsions[28]. Moreover, surfactants can self-assemble to different conformations and supply a soft template for formation of different nanostructures[23]. On the other hand, since silica nanoparticles can provide various porous frameworks with a wide range of pore sizes, well-defined

morphologies, and various chemical functionalities[29, 30]. The silica template-based synthesis approach has been recently reported as a promising strategy in producing a variety of nanostructures, including ordered mesoporous carbon thick films[29], cross-linked polymeric nanocapsules[31], palladium nanowires[32] and macroporous platinum[33]. During these synthesis reactions, silica plays an important role in determining the fabricated nanoparticles structure and morphology as a structure directing agent.

In previous work[22], a simple method was introduced to produce a nanofluid containing calcium-DTPMP nanoparticles by employing a polyacrylate polymer as dispersant to stabilize the nanoparticles with a combination of high energy sonication treatment. The aggregation of the obtained nanoparticles was controlled by adding surface coating material of polyacrylate so that the nanoparticles could travel through porous media instead of being filtered and removed by formation materials. As a continuation of previous work in our research group at Rice University, a similar strategy was followed in this study to fabricate the metal-phosphonate nanomaterials. A stable nanofluid, which is resistant to high temperature of 70 $^{o}$C and high salinity of 2% KCl, can be obtained. Moreover, the transition metal $Zn^{2+}$ was employed to fabricate Zn-phosphonate, since the inhibitor placement and return can be greatly enhanced by adding $Zn^{2+}$ in the inhibitor pill[11]. The designed nanofluids were loaded into different formation core materials to study their mobility in these porous media. Finally, squeeze

simulation experiments were carried out to test the potential application of such nanomaterials for scale treatment in oilfields.

The present dissertation is organized in the following manner. Background information and literature review is presented in Chapter 2, including oilfield scale control, conventional scale control strategy, scale inhibitor chemistry, interaction of scale inhibitor with formation materials as well as particle transport and deposition mechanism in porous medium. Chapter 3 is on the topic of surfactant-assisted synthesis of scale inhibitor nanomaterials and their transport, return in formation materials (published in *SPE J.*). Chapter 4 illustrated the synthesis and laboratory testing of zinc-phosphonate inhibitor nanomaterials and their transport and long-term return performance (published in *SPE J.*). Chapter 5 presented the synthesis of crystalline phase Ca-DTPMP nanomaterials and their transport in formation core materials (published in *Ind. Eng. Chem. Res.*). Chapter 6 is about the enhanced transport of the crystalline Ca-DTPMP nanomaterials in formation materials and their long-term flow back in laboratory squeeze simulation tests.

# CHAPTER TWO
# BACKGROUND AND LITERATURE REVIEW

## 2.1 Solubility and solubility product principle:

### 2.1.1 Solubility and scale formation:

Solubility is defined as the limiting amount of a solute which can be dissolved in a solvent under a given set of physical conditions[1]. Certain combination of chemical species will yield compounds with little solubility, and the capacity for water to dissolve these species in water is limited and precipitates can form once this solubility capability is exceeded by over saturation. The solid precipitates will form scales on the surface in contact with water, like the pipelines and reservoir formation in the hydrocarbon production processes. The formation of scale is troublesome and expensive to remove. Scale may form on the surfaces of various types of water treatment equipments, including the distribution line, domestic hot water heaters, cooling equipment, boilers, heat exchanger, etc[2]. The buildup of scale on the surfaces may lead to a significant flow reduction. The buildup of scale on metal surfaces may serve as insulation and cause decreased efficiency and also uneven scale deposition might lead to pitting corrosion[2].

### 2.1.2 Water-formed scale deposits in hydrocarbon productions:

Scales are basically inorganic deposits from water. Scale formation is one of the major problems in the oilfield together with corrosion and brine disposal[4]. With the progress of oil production, increasing amounts of brine water will be produced

and the brines are corrosive and tend to produce scales. In the hydrocarbon production activities, scale formation normally restricts hydrocarbon and brine water through injection, flow lines and tubing strings, leading to serious flow reduction. Hence, scale control should be one of the primary objectives in oilfield water handling operations. Typically, the three major types of scales formed in the oilfield productions are calcite (calcium carbonate), calcium sulfates and barite (barium sulfate). Detailed information regarding the formation mechanism of each type of scales can be found in many references[1, 2].

### 2.1.3 Solubility product principle:

The tendency of scale formation can be predicted by means of scale materials solubility calculations. When a sparingly soluble salt like barium sulfate ($BaSO_4$) is added to water, $Ba^{2+}$ and $SO_4^{2-}$ ions dissolve into the solution until equilibrium between ions in the solid crystals and in solution is established, indicating that the solution is saturated:

$$BaSO_{4,crystal} \leftrightarrow Ba^{2+} + SO_4^{2-}$$

At a given temperature and pressure, the amount of barite dissolved and thereby the product of the concentrations of the ions in the saturated solution should be constant. This constant is called the solubility product constant, written as:

$$K_{sp} = (Ba^{2+})_s(SO_4^-)_s \qquad \text{at saturation} \qquad (2.1)$$

where $K_{sp}$ denotes the solubility product constant, $(Ba^{+})_s$ and $(SO_4^{2-})_s$ refer to barium and sulfate activities at saturation. The value of $K_{sp}$ is only a function of temperature and pressure[34]. Activity is defined as the product of the activity coefficient and the concentration and can be expressed as:

$$(i) = [i]\gamma_i \tag{2.2}$$

The activity of $i^{th}$ species (i) is related to the concentration (molality) of the $i^{th}$ species [i] through the activity coefficient, $\gamma_i$. The activity coefficient is dependent on temperature (T), pressure (P), ionic strength (IS) and specific solution composition and is typically estimated from extra-thermodynamic models. The references state for activity is a one molal solution extrapolated from infinite dilution. The activity of a species at concentration [i] deviates from its ideal condition. The activity coefficient is a measure of the degree to which the concentration of species i deviates from its activity.

The supersaturation ratio (SR) can be regarded as the ratio of the ion activity product (IAP) to the solubility product constant:

$$\mathrm{SR(barite)} = \frac{\mathrm{IAP}}{K_{sp}} = \frac{(Ba^{2+})(SO_4^{-})}{K_{sp}(T,P)} \tag{2.3}$$

where SR and IAP denotes supersaturation ratio and ion activity product, respectively and $(Ba^{2+})$ and $(SO_4^{2-})$ refer to the barium and sulfate activities in solution in molal units. When the SR is larger than one, the solution is supersaturated and precipitation may take place.

## 2.2 Scale prediction and treatment:

### 2.2.1 Scaling tendency and saturation Index:

Based on the introduction of supersaturation ratio, the term saturation index (SI) can be introduced as the base-10 logarithm of the SR:

$$SI = \log_{10}(SR) = \log_{10}\frac{(Ba^{2+})(SO_4^-)}{K_{sp}(T,P)} \tag{2.4}$$

$K_{sp}$(T,P) indicates that the solubility product is a function of both temperature and pressure. It follows that:

1) SI=zero, the solution is in equilibrium (saturated) with the scale mineral, barite in this example;

2) SI<zero, the solution is undersaturated with the scale mineral and dissolution may take place but precipitation is not possible and

3) SI>zero, the solution is supersaturated with the scale minerals and scale can form but it might be kinetically delayed.

Oddo and Tomson developed[35] a semi-empirical approach for scaling prediction. Basically, the saturation ratio (SR) can be expressed as:

$$SR = \frac{IMP}{K_{sp}(T,P,IS)} \tag{2.5}$$

where IMP denotes the ion molality product and $K_{sp}$ becomes the conditional solubility product constant, dependent upon the specific composition. Hence, in this method, there is no need to consider the activity coefficients and the conditional equilibrium constants can be stated as a function of T, P and IS based

on experimentally obtained data. The conditional equilibrium constants from calcium carbonate and sulfate scales can be written as:

$$-\log_{10}(K_c) = a + bT + cT^2 + dP + eIS^{0.5} + fIS + gIS^{1.5} + hTIS^{0.5} \qquad (2.6a)$$

$K_c$ is the conditional constant and parameters a to h are curve-fitted constants.

He, Kan and Tomson[36] derived an inhibition model for barium sulfate scale prediction, which consists the following equations:

$$\begin{aligned} \log t_0 &= \alpha_0 + \frac{\alpha_1}{SI} + \frac{\alpha_2}{T} + \frac{\alpha_3}{SI \cdot T} \\ C_{inh} &= \frac{1}{b_{inh}} \log(f \frac{t_{inh}}{t_0}) \\ \log b_{inh} &= \beta_0 + \beta_1 SI + \beta_2 SI + \beta_3 pH + \beta_4 \log R \end{aligned} \qquad (2.6b)$$

The first equation is to make predications of the scale nucleation time ($t_0$) as a function of saturation index (SI) and temperature (T). The second equation is to calculate the concentration of inhibitor need ($C_{inh}$) as a function of required protection time ($t_{inh}$) and f is a safety factor. The $b_{inh}$ term in the second equation is related to the inhibition efficiency of a particular inhibitor and is a function of the saturation index, temperature, pH and the molar ratio of lattice anions in the brine ($R=[Ba^{2+}]/[SO_4^{2-}]$). The parameters ($\alpha_1$ to $\alpha_4$ and $\beta_1$ to $\beta_4$) are to be determined by curve fitting a large number of experimentally obtained data to the first and third equation.

### 2.2.2 Rate of scale formation:

Normally, the rate of the scale formation is of significance to oilfield scaling control. It commonly takes from a week to several months for a scale problem to be significant in the production, tubing and surface flow lines. The scale formation rate depends on flow rate, radius and length and the specific brine chemistry[4]. As for the case of calcite formation, Tomson et al proposed that four separate regions can be recognized, based on the solution saturation index (Fig. 2.1)[4]. Basically, at region where SI is negative, calcite cannot precipitate and calcite, if any is present, will dissolve toward equilibrium. When SI is between 0.00 to about 0.4, brines can be produced for long periods without scale formation. This is the region in which many early stage gas and oil wells operate. The region where SI is between 0.4 and around 2.3 is the transition from "no scale formation" to "rapid scale formation". Production of calcite scale will spontaneously take place within minutes, depending on the specific supersaturation. If SI is larger that the value of approximately 2.3, scale formation is uninhibitable regardless of the amount of inhibitors applied and massive and rapid scale formation is expected.

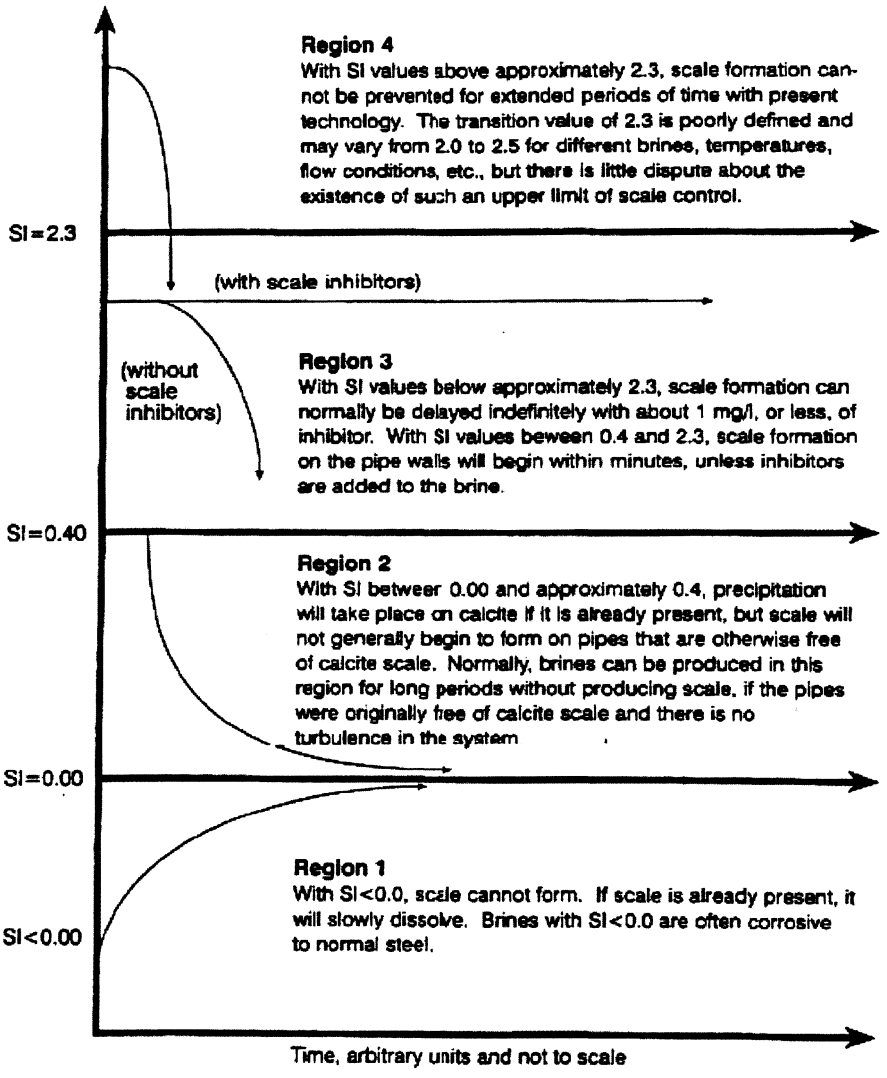


Figure 2.1 Four region of calcite SI values (copy from Tomson et al[4])

The rate of calcite formation on a steel pipes can be further calculated based on the mass transfer principles in a plug flow reactor. The following relation can be derived[4]:

$$\text{Flux} = \frac{SQ}{2\pi r}\{1-\exp(-\frac{2\pi r k_m}{Q}x)\} \qquad (2.7)$$

Flux refers to the mass of calcium carbonate deposited per unit time per unit area of pipe wall and S refers to the slope of equilibrium calcium concentration versus distance down the pipe($S = (d[Ca^{2+}]_{eq} / dx)$). Q is the volume of brine per unit time and r is the pipe radius. $k_m$ denotes the mass transfer constant and x is the distance from the well bottom.

### 2.2.3 Scale control methods:

Based on the above discussion, scale formation, as well as the rate of scale formation, is controlled by the degree of supersaturation, pH, temperature and other brine chemistry. Hence, by controlling these variables, scale deposit can be greatly reduced in the production system. Often, in the oilfield production, a threshold scale inhibitor is used for scale inhibition via a squeeze treatment. This is the most frequently used method of scale prevention in the petroleum industry. It has been confirmed by extensive laboratory and field testing that, generally 0.1 mg/L to 1 mg/L of phosphonate inhibitors is sufficient to prevent scale formation[4].

In order to apply the squeeze treatment[1, 37, 38], a pre-flush solution is injected to clean the production tubing and the formation. The inhibitor pill is prepared in a mixing tank by diluting the concentrated inhibitor solution to 0.5 to 5 percent by using production water, synthetic brine or natural brine and the pill is injected into the formation through perforation, after which, an overflush volume between 100

to 1000 bbl is injected in order to push the inhibitor pill into the formation. The well is then shut down for several hours to two days. During the shut-in period, the inhibitor pill is allowed to form a metal-inhibitor precipitate and adsorb on the surface of the rock. After this shut-in period, the well is put back on stream again and the inhibitor will be dissolved into the formation water and eventually flushed out of the production well. Typically, an initially large release of inhibitors is followed by a slow release of several milligrams per liter, which concentration is usually sufficient to prevent scale formation. The treatment frequency might vary from several weeks to several years.

### 2.2.4 Common oilfield mineral scale inhibitors:

Scale inhibitors are capable of preventing or retarding the formation of inorganic scales. Some authors[39] subcategorize the scale inhibitors into two types: 1) nucleation inhibitors, like polymers: they adsorb onto the formed crystal surfaces and the lattice, leading to a slowly crystal growth[40, 41]; 2) crystal growth inhibitors, like aminophosphonates: this type of inhibitors tends to be capable of preventing scale crystal growth by blocking the surface active sites.

#### 2.2.4.1 Phosphino polymers:

The most commonly used phosphino polymer in the oilfield for scale control is polyphosphinocarboxylic acid (PPCA) (Fig.2.2). The presence of the phosphorus atom makes it easier to analyze PPCA and enhance the inhibition performance,

calcium compatibility and the attachment of PPCA to formation rocks, resulting in an extended squeeze lifetime[39].

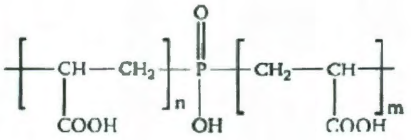


Fig. 2.2 Structure of polyphosphinocarboxylic acid

**2.2.4.2 Aminophosphonate:**

The introduction of an amine group into a phosphonate molecule increases the metal binding capability due to the amine and phosphonate interactions. There are many different types of phosphonates commonly utilized in the oilfield. The molecular structures of a few of the more common phosphonates are shown in Fig. 2.3. Aminotris (methylene phosphonic acid) (NTMP) can bind to metal ions via all three phosphonic acid groups and the lone pair on the nitrogen atom. Diethylenetriamine penta(methylene phosphonic acid) (DTPMP) is able to inhibit various types of scale formation and probably the most widely used phosphonate scale inhibitor in the oil industry. Bis-hexamethylenetriamine penta(methylenephosphonic acid (BHPMP) is another scale inhibitor, which has improved calcium tolerance and is useful for high-temperature application of 120 to >140°C conditions[39]. In this study, the aminophosphonate, especially DTPMP will be utilized as the scale inhibitors for nanomaterials synthesis.

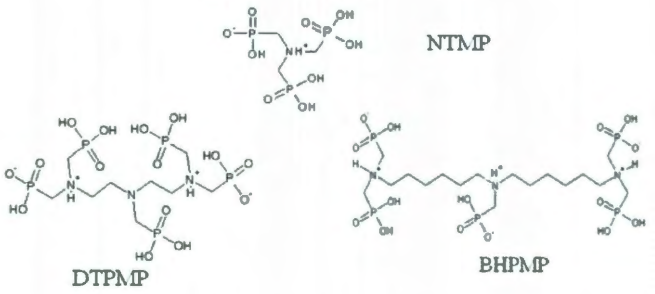


Figure 2.3 Structures of three commons oilfield scale inhibitors.

### 2.2.5 Mechanisms of scale inhibition using inhibitors:

Extensive studies have been carried out to understand the mechanism and functionality of scale inhibitors, e.g., phosphonate in inhibiting scale formation, including calcite and barite scales. One of the classical theories in predicting the kinetics of scale inhibitors on scale formation is Burton-Cabrera-Frank (BCF) spiral growth mechanism[42]. According to the physical picture of the BCF theory, as the crystal growth proceeds, the adsorbed ions will diffuse along the surface and incorporate preferentially into the crystal lattice at kink sites, leading to a winding-up step in a surface spiral, which process is also named as screw dislocation growth[43, 44]. The process of inhibition induced by the presence of inhibitors is regarded as the blocking of the spiral growth at the active sites on crystal surfaces by adsorbed inhibitors[45]. Several other research efforts indicated that the inhibitors must adsorb at the surface active growth sites in order to interfere the growth process[43, 46] and that the solution chemistry including the divalent metal concentrations and the solution pH will affect the phosphonate

scale inhibitor efficiency[47, 48]. Tomson et al.[45] investigated the inhibition of several phosphonates on calcite and barite scale formation via a series of adsorption, desorption and nucleation experiments in terms of kinetics and thermodynamics. It was observed that the approximately 16% of surface coverage for any mineral is needed in order to completely inhibit crystal nucleation, which sets the maximum inhibitor concentration; while the minimum inhibitor concentration needed is related to the flow rate in a well. It was also proposed by the authors that the primary driving force for inhibitor adsorption to mineral surfaces is hydrophobic repulsion of a macromolecule from its aqueous solution.

### 2.3 Phosphonate inhibitor retention: adsorption and precipitation

The mechanism of the scale inhibitor interaction with formation predominately controls the placement of inhibitor in the formation and the squeeze lifetime, which is of great importance for enhancing the performance of inhibitors in the squeeze treatment. Even though the mechanism of scaling inhibition by scale inhibitors is still under debate, extensive amount of fundamental and mechanistic studies has been carried out on the topics of scale formation[5, 49, 50], scale inhibition[49, 50] and scale inhibitor interactions and reactions with rock substrates and minerals[22, 51-53], summarized by Yuan[54]. Generally speaking, adsorption and precipitation are the two major mechanisms proposed to control the placement of phosphonate inhibitors in the rock formation. It has been postulated by Kan and Tomson that[51-53] 1) under low phosphonate inhibitor concentration, inhibitor

concentration was determined by chemical sorption mechanisms, characterized by a Langmuir type adsorption for NTMP to calcite surface and 2) under high inhibitor concentration, formation of calcium-phosphonate precipitate dominates the attachment of inhibitor to calcite surface.

### 2.3.1 Adsorption mechanism:

Sorption is referred as the process in which chemicals become associated with solid phases. It is adsorption if the molecules attach to a two-dimensional surface and absorption if the molecules form a three-dimensional homogeneous phase[55]. The adsorbent(s) is a particular solid or mixture of solids with which a chemical associates while the chemical is called the adsorbate. According to the binding mechanisms of adsorbates to adsorbent, adsorption can be differentiated into physical adsorption and chemical adsorption. Chemical adsorption, which is considered to be permanent or irreversible, is due to the strong specific intermolecular forces, comparable with those leading to the formation of chemical compounds[56]. The adsorbate will form a monolayer thick coverage over the surface of adsorbent and adsorbed materials are not considered to be able to move freely on the surface. When the adsorbent surface is covered by the adsorbate molecules, the adsorption capacity of the adsorbent is greatly compromised. On the other hand, physical adsorption is nonspecific and generates from the weak forces of attraction or van der Waals' forces between molecules. Therefore, the adsorbed molecule is not fixed to the adsorbent surface and is free to move over

the surface. Moreover, the adsorbed material may form a multilayered structure on the surface of adsorbent. Physical adsorption is reversible and when the concentration of the adsorbate materials decreases, the adsorbates will be desorbed from the adsorbent surface. As for the inhibitor retention by the rock materials, physical adsorption is more desirable since the scale inhibitor can be gradually desorbed from the rock surface and return at a level to prevent scale formation. An overflush volume is needed to push inhibitor farther into the formation, so that a longer squeeze life can be accomplished. It has been proposed that the adsorption of phosphonate scale inhibitors on a mineral surface was driven by the mechanism of hydrophobic repulsion rather than some specific inhibitor molecules-surface interaction[45].

### 2.3.2 Precipitation mechanism:

The precipitation squeeze is the process where phosphonate inhibitors form a salt in the formation, followed by a dissolution process controlling the slow release of inhibitors into the production brine. Basically, the acid in the phosphoantes will react with the formation calcite and divalent cations in the water during the shut-in period, forming metal (mainly $Ca^{2+}$) -phosphonate complexes, which precipitate on the rock surface. When production resumes, these precipitates will gradually dissolve into the production water to prevent scale formation[8, 9]. The inhibitor concentration is periodically monitored and once the inhibitor concentration drops below the pre-determined level, the inhibitor treatment must be repeated to

maintain the required level of scale inhibitor. It was concluded that, other than rock mineralogy, inhibitor and solution chemistry are important determinants for inhibitor retention and release.

Delivery of phosphonate inhibitors to a production well is commonly applied through an inhibitor squeeze treatment, wherein inhibitors are squeezed into a downhole formation so that they can precipitate with divalent cations, mostly calcium, and be slowly released into production brine fluid to prevent scale formation [52, 53, 57]. Often the squeeze treatment is an effective means to place inhibitors in the reservoir[12]. However, some inhibitors may not be placed in the reservoir efficiently. In the conventional squeeze treatment, the acidic pill will dissolve metal ions from the formation that leads to precipitation of the inhibitor salt near the wellbore. Even though neutralized inhibitors can be pushed into formation, they are less effective due to weak adsorption to the rock[4], [22]. It is desirable to be able to control the migration, placement, and return of a large amount of scale inhibitors in the formation. As indicated by various authors, it is possible to form pre-precipitate materials and to inject these materials into the downhole formation through perforation for scale control and utilization of scale inhibitor precipitation treatment technology has been investigated previously by several research groups[13, 14]. It has been observed that[14-16], several parameters including the inhibitor concentration, solution pH, the presence of salt, dissolution property of inhibitors and binding capability with divalent metals will

significantly impact the results of the precipitation treatment and the placement of inhibitors in the downhole formation, indicating that it might be possible to design the precipitation treatment to control the inhibitor return level[13]. As Jordan *et al* stated, compared with the adsorption treatment, the precipitation treatment greatly enhanced the squeeze performance and the precipitate solubility together with the field brine chemistry plays an essential role in determining the inhibitor return concentration and precipitate treatment lifetime[13, 17]. On the other hand, some modeling work regarding the inhibitor squeeze performance and nucleation with divalent metals has been carried out so as to make prediction of the inhibitor precipitation treatment[18, 19]. Other than conventional metal-phosphonate precipitates, some novel types of inhibitor precipitates, including the enzyme activated and oil-soluble inhibitors have been fabricated for precipitate treatment[20, 21]. The concern regarding the industrial application of a precipitation squeeze is the formation blockage and damage caused by the inhibitor precipitation in the near wellbore area. Therefore, it is important to study the transport behavior of the fabricated inhibitor precipitates in the formation media.

### 2.3.3 Phase transition of calcium-DTPMP precipitates and its significance:

According to the above inhibitor precipitation theory, the retention and release of the phosphonates is governed through precipitation and dissolution of calcium-phosphonate (Ca-Phn) precipitates: calcium ion is the primary divalent ion abundant in the brine solution due to the equilibrium of brine with calcite in the

oil-bearing formation. The injected phosphonates will form calcium-phosphonate precipitates near the wellbore, which process also affixes the inhibitors on mineral surfaces. The phosphonate return concentration in the producing water should approach the thermodynamic solubility of the Ca-Phn under certain physiochemical conditions. Kan et al.[58] utilized a combined method of dialysis and filtration to prepare and develop the amorphous Ca-DTPMP precipitates with a synthetic brine solution. It was found that the initially amorphous phase Ca-DTPMP can be developed into a crystalline phase with needle shape structure. The obtained crystalline materials bear a solubility several order of magnitude lower than the precursors, calculated using the calculation strategy developed by Tomson et al[59] at the same ionic strength and temperature conditions. This phenomenon suggests that the return performance of the phosphonates in the resumed production process is controlled by a two-step mechanism: first, a higher inhibitor return concentration is encountered as a result of the dissolution of the amorphous phase highly soluble precipitates. As the process proceeds, the amorphous materials will be gradually developed into a well-developed crystalline phase, which is responsible for the long term inhibitor return with lower return concentrations[9]. Similarly, these authors found that another commonly used scale inhibitor NTMP can form two types of Ca-NTMP solid phases, one amorphous and one crystalline phases and the long term phosphonate return was controlled initially by the amorphous phase which gave a higher return concentration and later by the crystalline materials, leading to much lower return concentrations[9].

### 2.3.4 ScalesoftPitzer software package for scale control prediction:

The ScalesoftPitzer (SSP) software package is an Excel based software program to predict scale formation for numerous minerals and it dates back to May 1994 when Oddo and Tomson presented the first version of SSP for saturation index prediction for calcite and common sulfate scales[60]. SSP software is designed to calculate the pH, scaling tendency, and inhibitor needs of oil and gas wells for commonly encountered minerals[61, 62]. Based on Pitzer theory of electrolytes[63] and Peng Robinson equation of state for gas fugacity coefficient[64], SSP software adopted the Pitzer parameters for the interaction between carbonate species and other ions, derived from the $CO_2$ solubility and the first and second stoichiometric dissociation constants of carbonic acid by He et al[65]. SSP also considers the effect of the presence of hydrate inhibitors (mainly alcohols). According to Kan et al[66], consider the case when both alcohol and saltwater are present in the solution, the free energy change of the ion due to solution composition can be expressed as:

$$\begin{aligned}\Delta G^{ex} &= RT \ln \gamma_{total} \\ &= \Delta G^{ex}_{al/w} + \Delta G^{ex}_{salt} \\ &= RT \ln \gamma_{al/w} + RT \ln \gamma_{salt}\end{aligned}$$

Where $\Delta G^{ex}$ is the molar excess free energy change due to the total change in solution composition from pure water to alcohol/water and then to salt solution in the alcohol/water mixture. $\Delta G^{ex}_{al/w}$ and $\Delta G^{ex}_{salt}$ are the molar excess free energy changes for the reference state ion transfer from pure water to the pure alcohol/water mixture and from the alcohol/water mixture to the alcohol/water/salt

solution, and $\gamma_{al/w}$ and $\gamma_{salt}$ are the corresponding activity coefficients. The software also considers some other effects including hydrate inhibitors, commingling brines, seawater mixing and limit of sulfate tolerance and reservoir scaling tendency, etc. In November 2009, Tomson presented an updated version of SSP (SSP 2009) including a few mass transfer calculations.

### 2.3.5 Environmental significance:

Phosphonates are used in an increasing amount in a wide range of application, including scale and corrosion inhibition; oil drilling; cleansing and laundry operations; and agriculture. It has been found that phosphonates can not be biodegraded during conventional wastewater treatment[67, 68] but rather are removed by adsorption onto biosolids and sludge[69, 70]. Moreover, in many oil fields, as gas and oil production progresses, the ratio of produced brine water to hydrocarbons often increases. Typically, 10 to 20 barrels of brine will be produced with one barrel of oil or gas equivalent and these brines are corrosive and tend to produce calcite or sulfate scales. Therefore, it is of great environmental interest to control the scale formation as well as the fate and transport and distribution of phosphonate and its metal complex in the environmental media.

## 2.4 Acid/base and divalent metal complexation chemistry of phosphonate inhibitors

Effort has been made to develop the modeling calculation of the protons and metals with phosphonate in order to develop the molecular mechanisms and predict the temperature and ionic strength effects. However, this problem is complicated by the fact that there are multiple ionizable protons on the molecular backbone of the phosphonate; hence there are multiple charged groups in a single molecule (Fig. 2.3). Tomson et al derived the speciation model based on the electrostatic effect and the assumption that the protonation constants are a linear function of charge and also reported the temperature and ionic strength dependence of proton ionization and metal complex formation[59]. Experimentally obtained results were compared with the modeling result in order to verify the validity of the model. Moreover, this model was employed to study the ferrous iron phosphonate complex and ferrous calcium phase in the oilfield brine[38].

### 2.4.1 Derivation of the speciation equations for phosphonate

According to Tomson et al[59], the first association constant is expressed as:

$$Phn^{n-} + H^{+} \leftrightarrow HPhn^{(n-1)-}$$

and

$$K_1^N = \frac{(HPhn^{(n-1)-})}{\{H^{+}\}(Phn^{n-})} \qquad (2.8)$$

where parentheses refer to concentration in molality and $H^+$ refers to the activity of proton in solution. "n" is the value of the total number of ionizable protons of phosphonate (for DTPMP n=10; for NTMP, n=6).The superscript N denote that

this constant refers to the association with an $sp^3$ hybridized basic nitrogen atom, similar to ammonia. Tikhonova[71] confirmed that the first two protons of DTPMP and the first proton of NTMP are associated with nitrogen atoms. Thus, the concentration of the deprotonated species ($HPhn^{(n-1)-}$) can be expressed as:

$$(HPhn^{(n-1)-}) = K_1^N \{H^+\}(Phn^{n-}) \tag{2.9}$$

Define $K_2$, $K_3$ to $K_i$ are the proton association constants for the 2nd 3rd to i$^{th}$ species and:

$$H_{i-1}Phn^{(n+1-i)-} + H^+ \leftrightarrow H_iPhn^{(n-i)-}$$

$$K_i = \frac{(H_iPhn^{(n-i)-})}{\{H^+\}(H_{i-1}Phn^{(n+1-i)-})} \tag{2.10}$$

Hence, an arbitrary species ($H_iPhn^{(n-i)-}$) can be expressed in terms of equilibrium constants, free phosphonate ($Phn^{n-}$) and pH:

$$(H_iPhn^{(n-i)-}) = K_1^N K_2^N K_3 ... K_i \{H^+\}^i (Phn^{n-}) \quad for \quad i \geq 2 \tag{2.11}$$

For simplicity, the term "beta" is a cumulative formation constant notation:

$$\beta_i \equiv K_1^N K_2^N K_3 ... K_i, \quad for \quad i \geq 3 \tag{2.12}$$

By assuming that the proton association constant is a linear function of the charge, the following equation was postulated:

$$\log K_i = a_{H^+} + b_{H^+}|q_{i-1}| \tag{2.13}$$

where $a_{H^+}$ and $b_{H^+}$ are constants to be determined by using the titration data and $|q_{i-1}|$ denotes the absolute value of the charge of the (i-1)$^{th}$ species. The value of $b_{H^+}$ can be obtained from the combination of the mass balance for total

phosphonate with the electroneutrality condition. The mass balance for total phosphonate can be given by:

$$C_{Phn} = (Phn^{n-}) + \sum_{i=1}^{n} (H_i Phn^{(n-i)-}) \tag{2.14}$$

Substituting equation 2.11 and 2.12 into 2.14 and yield:

$$(Phn^{n-}) = C_{Phn} \Big/ (1 + \sum_{i=1}^{n} \beta_i \{H^+\}^i) \tag{2.15}$$

The electroneutrality condition at any point of titration of phosphonate with NaOH is given by:

$$(Na^+) + (H^+) = n(Phn^{n-}) + \sum_{i=1}^{n} (n-i)(H_i Phn^{n-1}) + (OH^-) + (Cl^-) \tag{2.16}$$

Finally, substituting equations 2.11, 2.12, 2.14 and 2.15 into 2.16 and rearranging, the concentration of base need to reach a certain pH can be calculated by:

$$(Na^+)_{cal} = \frac{nC_{Phn}}{1 + \sum_{i=1}^{n} \beta_i \{H^+\}^i} + \sum_{i=1}^{n} (n-i)\beta_i \{H^+\}^i \frac{nC_{Phn}}{1 + \sum_{i=1}^{n} \beta_i \{H^+\}^i} (Phn^{n-}) + (OH^-) + (Cl^-) - (H^+) \tag{2.17}$$

In order to acquire the value of $\beta_i$, which is a function of $a_{H^+}$ and $b_{H^+}$, at least two titration points are needed to solve the above equations.

### 2.4.2 Derivation of speciation equations for complexation with divalent metals

A similar approach was utilized to model the complexation of phosphonate with divalent metal ions. The general complexation reaction is given by:

$$M_{j-1} H_i Phn^{(n-i-2(j-1))-} + M^{2+} \leftrightarrow M_j H_i Phn^{(n-i-2j)-} \tag{2.18}$$

The corresponding equilibrium constant $K_{ij}$ is given by

$$K_{ij} = \frac{(M_{j-1}H_iPhn^{(n-i-2(j-1))-})}{(M^{2+})(M_jH_iPhn^{(n-i-2j)-})} \quad for \quad i \geq 2, j \geq 2 \tag{2.19}$$

where $M^{2+}$ denotes the divalent metal. The concentration of an arbitrary metal-phosphonate complex is given by:

$$(M_jH_iPhn^{(n-i-2j)-}) = \beta_{ij}(M^{2+})^j\{H^+\}^i(Phn^{n-}) \tag{2.20}$$

where $\beta_{ij}$ is the cumulative formation constant for the complex species:

$$\beta_{ij} \equiv K_1^N K_2 K_3 ... K_i K_{i1} K_{i2} ... K_{ij} = \beta_i K_{i1} K_{i2} ... K_{ij} \tag{2.21}$$

Assuming that the complexation constant is a linear function of charge, thus, the complexation constants can be given by:

$$\log K_{ij} = a_{M^{2+}} + b_{M^{2+}}\left|q_{2j-2+i}\right| \quad for \quad i > 1, j > 1 \tag{2.22}$$

Following the above mathematical method for phosphonate proton association, but with an added mass balance equation for divalent metals present in the system, the mass balance equations can be expressed as:

$$C_{Phn} = (Phn^{n-}) + \sum_{i=1}^{n}(H_iPhn^{n-1}) + \sum_{i=1}^{n}\sum_{j=0}^{(n-i)/2}(M_jH_iPhn^{n-2j-i}) \tag{2.23}$$

and

$$C_M = (M^{2+}) + \sum_{i=1}^{n}\sum_{j=0}^{(n-i)/2}(j)(M_jH_iPhn^{n-2j-i}) \tag{2.24}$$

The electroneutrality condition is given by:

$$(Na^+) + (H^+) = \sum_{i=1}^{n}(n-i)(H_iPhn^{n-1}) + \sum_{i=1}^{n}\sum_{j=0}^{(n-i)/2}(n-2j-i)(M_jH_iPhn^{n-2j-i})$$
$$+ (Cl^-) + (OH^-) - 2(M^{2+}) - (H^+) \tag{2.25}$$

by substituting and rearranging, the mass balance can be written in terms of free phosphonate and free metals:

$$(Phn^{n-}) = \frac{C_{Phn}}{1+\sum_{i=1}^{n}\beta_i\{H^+\}^i + \sum_{i=2}^{n}\sum_{j=0}^{(n-i)/2}\beta_{ij}(M^{2+})^j\{H^+\}^i} \tag{2.26}$$

$$C_{M^{2+}} = (M^{2+}) + \frac{\sum_{i=2}^{n}\sum_{j=0}^{(n-i)/2}(j)\beta_{ij}(M^{2+})^j\{H^+\}^i C_{Phn}}{1+\sum_{i=1}^{n}\beta_i\{H^+\}^i + \sum_{i=2}^{n}\sum_{j=0}^{(n-i)/2}\beta_{ij}(M^{2+})^j\{H^+\}^i} \tag{2.27}$$

For known total concentration of metal and phosphonate at a given pH, the concentration of free metal and phosphonate can be calculated based ON the above equations. The complexation factors $a_{M^{2+}}$ and $b_{M^{2+}}$ can be determined from the electroneutrality, normally $a_{M^{2+}} \approx 0$.

## 2.5 Colloidal and nanosized particle transport in porous media:

Conventionally, nanoparticle transport in porous media can be described by combining the advection-dispersion theory and the filtration theory.

### 2.5.1 Classic advection-dispersion theory:

The one-dimensional advection-dispersion equation (ADE) [72-74] is generally used to model the flow of non-reactive particles through porous media, like sandy materials.

$$\frac{\partial C_v}{\partial t} = D\frac{\partial^2 C_v}{\partial x^2} - v\frac{\partial C_v}{\partial x} \tag{2.28}$$

where, $C_v$ is the volume-averaged concentration defined as the mass of solute per unit volume of fluid contained in an elementary volume at a given time-mg $L^{-1}$ or mg $ml^{-1}$; t is the time-sec; D is the dispersion coefficient-$cm^2$ $sec^{-1}$; x is the downstream distance-cm and v is the linear velocity or pore velocity-cm $sec^{-1}$. To account the removal of particles to the porous media, a term is added to equation 2.9 and yields:

$$\frac{\partial C_V}{\partial t} = D\frac{\partial^2 C_V}{\partial x^2} - v\frac{\partial C_V}{\partial x} - \frac{\rho}{\varepsilon}\frac{\partial S}{\partial t} \tag{2.29}$$

where S is the concentration of particles sorbed by the porous media (mg $g^{-1}$); ρ is the bulk density of the media (g $ml^{-1}$) and ε is the porosity of the media (dimensionless). When the amount of particles sorbed by the porous media, S is directly proportional to the solution concentration, $C_v$, then equation 2.29 can be written as [75, 76]:

$$R\frac{\partial C_V}{\partial t} = D\frac{\partial^2 C_V}{\partial x^2} - v\frac{\partial C_V}{\partial x} \tag{2.30a}$$

and

$$R = 1 + \frac{\rho}{\varepsilon}K_d \tag{2.30b}$$

where a retardation factor R is included in the above equation to account for the retardation effect due to the sorption of nanoparticles by the porous media and kd is the linear partitioning coefficient. The above development is predicated on two assumptions [72, 77]: a linear sorption isotherm and local equilibrium partitioning of the particles between the flowing solution and the porous media. Since the R value

is characteristic of the sorptive behavior of the nanomaterials to the medium surfaces, it should be independent of the pore flow velocity.

Other than sorption to the porous medium surfaces, colloidal particles can be retained by the porous medium via first-order kinetic removal mechanism at a constant removal rate. An additional term can be added to account the first order removal[78, 79]:

$$R\frac{\partial C_V}{\partial t} = D\frac{\partial^2 C_V}{\partial x^2} - v\frac{\partial C_V}{\partial x} - J_d C \qquad (2.31a)$$

where $J_d$ ($h^{-1}$) is the removal rate coefficient. Based on the filtration theory, the first-order rate constant $J_d$ can be calculated by[80, 81]:

$$J_d = -\frac{v}{L}\ln(C_e / C_o) \qquad (2.31b)$$

where L is the length of the porous media (m) and $C_e$ denotes the steady-state effluent concentration of the nanoparticles and $C_o$ is the influent nanoparticles concentration. The term of $J_d$ can be elucidated from Derjaguin-Landau-Verwey-Overbeek (DLVO) theory[82, 83]. According to DLVO theory, a primary energy barrier exists between the particles and the surfaces, which inhibits the attachment of the particles to the surface. The colloidal particles have to be able to overcome the energy barrier in order to attach to primary energy minimum. The deposition rate is related to the height of this energy barrier by increasing exponentially with decreasing height of the energy barrier[84]. The solution ionic strength will greatly

affect the deposition kinetics since the increase of ionic strength will diminish the energy barrier due to the compression of the double layer, resulting in an accelerated deposition rates. According to Ruckenstein and Prieve[85], the deposition rate increases exponentially with the decrease of height of energy barrier under theoretical consideration:

$$J_d \propto \exp(-\frac{\Delta V_d}{k_B T}) \tag{2.32}$$

where $\Delta V_d$ (J) is the height of energy barrier, $k_B$ is Boltzman constant ($1.38\times10^{-23}$ J $K^{-1}$) and T (K) is the absolute temperature. Since the pore flow velocity has no contribution on the height of the primary energy barrier, the flow velocity should not affect the deposition kinetics (the $J_d$ value). On the basis of the above arguments, both R and $J_d$ values should be independent of pore flow velocity.

### 2.5.2 Simulating contaminant transport using the CXTFIT model:

Solutions of the advection-dispersion equation 2.28 can take the form of an analytical solution or a numerical solution. It is necessary to differentiate the volume-averaged concentrations and flux-averaged concentrations for column displacement experiments in order to maintain the mass balance and solute flux continuity at the column inlet [77, 86]. Mathematical transformation of the advection-dispersion equation from volume-averaged to flux-averaged concentration was presented by Parker and van Genuchten [86] by using the definition of the flux-averaged concentration:

$$C_f = C_V - \frac{D}{v}\frac{\partial C_V}{\partial x} \tag{2.33}$$

where $C_f$ is the flux-averaged concentration (mg $L^{-1}$)

$C_v$ is the volume-averaged concentration (mg $L^{-1}$)

v is the pore velocity (cm $hr^{-1}$)

The volume averaged concentration ($C_v$) is defined as the mass of solute dissolved in s specified unit volume of solution. The flux-average concentration ($C_f$) represents the "mass of solute per unit volume of fluid passing a given cross section during an elementary time interval[87]". In many instances, the experimentally obtained or measured concentrations are flux-averaged rather than volume-averaged, like effluent concentration of flushing a tracer in a column (Fig. 2.4).

a

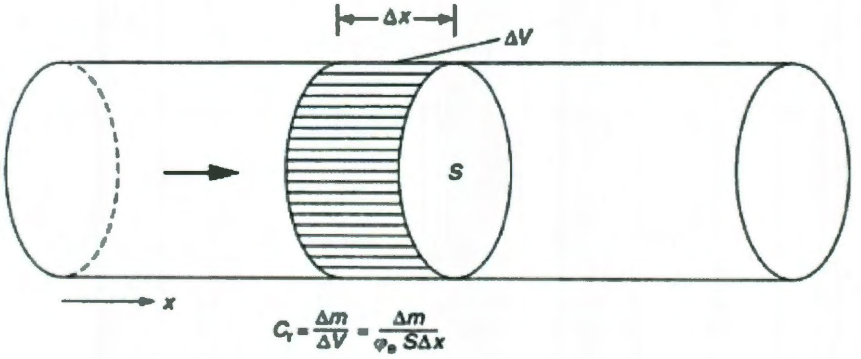

b

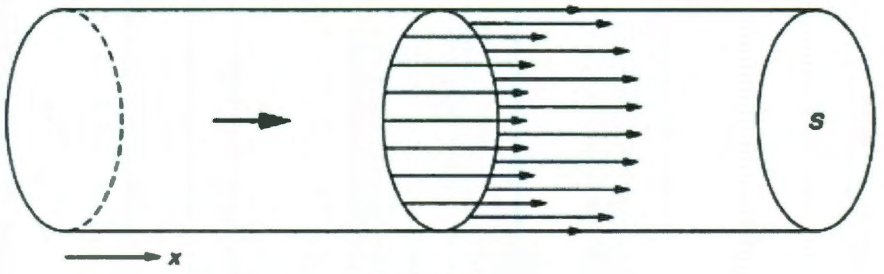


$$C_f = \frac{F_x S\Delta t}{Q\Delta t} = \frac{F_x S}{Q}$$

$F_x$ = Mass flux of solute (mass per unit area per unit time)

$Q$ = Volumetric flow rate

$S$ = Cross-sectional area of the tube

Figure 2.4 (a) The definition of volume-averaged concentration; (b) the definition of flux-averaged concentration (Copy from Batu et al.[88])

Equation 2.28 can be transformed into:

$$\frac{\partial C_f}{\partial t} = D\frac{\partial^2 C_f}{\partial x^2} - v\frac{\partial C_f}{\partial x} \tag{2.34}$$

which is mathematically identical to equation 2.28 with $C_v$ replaced by $C_f$. Assuming a semi-infinite column and the transformed initial and boundary conditions as follows [77]:

$$\text{initially condition: } C_f(x,0) = 0$$

$$\text{lower boundary condition: } \frac{\partial C_f}{\partial x}(\infty,t) = 0$$

$$\text{upper boundary condition: } C_f(0,t) = C_0$$

the solution for equation 2.34 is:

$$C_f(x,t) = \frac{1}{2}erfc\left(\frac{x-vt}{2(Dt)^{1/2}}\right) + \frac{1}{2}\exp\left(\frac{vx}{D}\right)erfc\left(\frac{x+vt}{2(Dt)^{1/2}}\right) \tag{2.35}$$

Above solution can be expressed in the following form [77, 86]:

$$C_f(x,t) = \frac{1}{2} erfc\left(\frac{x - v_c t}{2(D_c t)^{1/2}}\right) + \frac{1}{2}\exp\left(\frac{v_c x}{D_c}\right) erfc\left(\frac{x + v_c t}{2(D_c t)^{1/2}}\right) \qquad (2.36)$$

where pore water velocity (v) is replaced by the velocity of the contaminant in the water ($v_c$) divided by the retardation factor (Eq. 2.30b):

$$v_c = \frac{v}{R} \qquad (2.37)$$

and the dispersion coefficient for the linear equilibrium sorption case can be defined as:

$$D_c = \frac{D}{R} \qquad (2.38)$$

The CXTFIT model developed by Parker and van Genuchten (1984) [86] is a nonlinear least squares inversion method for determining the parameters of a number of 1-D solute transport models. And two important assumptions for CXTFIT model were linear equilibrium adsorption with production and decay terms and a two site/two region non-equilibrium model [77]. In this thesis study, CXTFIT model will be utilized as an analytical solution to fit the experimentally obtained data.

### 2.5.3 Classic colloidal filtration theory (CFT):

In another effort, based on the particle deposition theory, the transport of colloidal particles in the porous matrix is dominated by the collision of the particles with a matrix surface as well as the attachment of the particles to the matrix surface[89],

modeled by the CFT model. The CFT model can be employed to quantify the nanoparticles deposition with respect to different transport mechanisms: Brownian diffusion, interception and gravitational sedimentation (Fig. 2.5). The deposition of nanoparticles on porous media involves two consecutive steps: (i) transport of particles to the matrix surfaces by Brownian diffusion, interception, and/or gravitational sedimentation, and (ii) deposition of particles to the matrix surface (the collector)[90, 91]. Physical parameters such as particle size, density, pore fluid velocity, pore structure, and the accessible surface area of the matrix can affect the mass transfer of the particles, whereas the solution and surface chemistry will govern the kinetics of particle deposition.

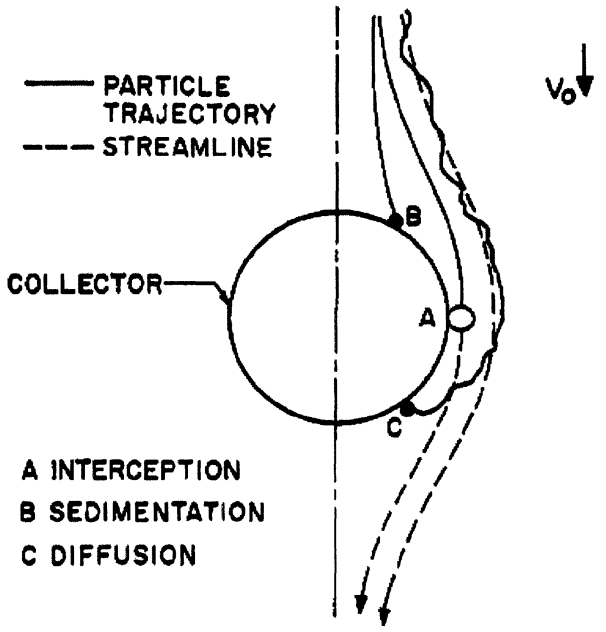


Figure 2.5 Transport mechanisms of particles deposition on a collector surface. (from Yao et al[92])

The parameters of single collector efficiency (η) and the particle attachment efficiency (α) were introduced to describe the above transport process. According to Tufenkji and Elimelech[93], the overall single-collector efficiency is the summation of the single collector efficiency due to diffusion, interception and gravitational sedimentation. The attachment efficiency is introduced to represent the fraction of the collision between particles and collectors that lead to attachment and can be calculated as:

$$\alpha = -\frac{2d_c}{3(1-\varepsilon)L\eta}\ln(\frac{C}{C_0}) \qquad (2.39)$$

where $d_c$ represents the diameter of a collector. L stands for the length of the porous media, ε is the porosity of the media and $C/C_0$ is the normalized effluent

concentration where C and $C_o$ are the particle concentration present at distance L and L=0. Typically, Brownian diffusion is identified as the predominant mechanism for the removal of nanoparticles by porous media by extensive study[90, 94, 95]. Moreover, for some high-density particles, like iron oxide, the gravitational sedimentation is also important for particle removal.

According to CFT, the removal of particles from liquid phase is controlled by a kinetic attachment mechanism which includes processes of mass transfer and attachment. The attachment is typically considered to be irreversible. Moreover, based on equation 2.29, the kinetics of attachment can be expressed by the first order deposition rate coefficient, $k_{att}$

$$\frac{\rho}{\varepsilon}\frac{\partial S}{\partial t} = k_{att} C \tag{2.40}$$

The deposition rate constant $k_{att}$ can be expressed as

$$k_{att} = -\frac{3(1-\varepsilon)v}{2d_c}\eta\alpha \tag{2.41}$$

The maximum transport distance ($L_{max}$) is defined as the travel distance over which 99% removal of nanoparticles occurs and can be calculated via:

$$L_{\max} = -\frac{2}{3}\frac{d_c}{(1-f)\alpha\eta}\ln(0.01) \tag{2.42}$$

# CHAPTER THREE
# SURFACTANT-ASSISTED SYNTHESIS OF SCALE INHIBITOR NANOMATERIALS*

## 3.1 Materials and methods:

**3.1.1 Chemicals** Commercial grade phosphonate scale inhibitors used in the study are diethylenetriaminepentakis (methylenephosphonic acid) (DTPMP) and bis-hexamethylenetriamine penta (methylene phophonic acid) (BHPMP), both of which are with 50% activity. Chemicals such as calcium chloride dihydrate, potassium chloride, nitric acid and sodium hydroxide, sodium tetradodecylammonium bromide (TTAB), and sodium dodecyl sulfate (SDS) surfactants are reagent grade and are purchased from Fisher Scientific unless otherwise specified. Tritiated water is purchased from Sigma-Aldrich (Amersham Co. Arlington Height, IL) for the measurement of porosity of porous media. Deionized water is prepared by reverse osmosis followed by a four stage ion exchange water purification process, consisting of a Barnstead high capacity cation/anion column, two Barnstead ultra pure ion exchange columns and then a Barnstead organic removal column.

**3.1.2 Preparation of Metal-Phosphonate nanoparticles** In a typical nanoparticle fabrication process, about 1.5 gram TTAB surfactant was added into 40 ml 0.25 M $CaCl_2$ solution, followed by constant stirring for 15 min till total dissolution of

*The content of this chapter has been published at *SPE J.* 2010 15 (3) 610-617. It was reproduced here as submitted and the only changes here are the numbering of tables and figures, which have been renumbered to adhere to the format of this thesis.

TTAB into the aqueous phase. A clear transparent solution of calcium-TTAB was obtained with pH of 6.0. Then, 25ml solution of 0.1 M DTPMP with potassium chloride (pH=9.0 neutralized by KOH) was added drop wise to the above solution in a two-neck flask under constant stirring. Upon injection of phosphonates into calcium solution, a white milky precipitate formed immediately. Typically, the solution pH and dissolved calcium and phosphonate concentration was stable after 15 min and remained so for days. After moderate stirring for 1 hour, the white slurry was transferred to a Teflon-lined glass vial and aged at 80 $^{o}$C in water bath for 12 hours. After being filtered through 2μm filter to remove the large particles, a white suspension with 2% KCl and final pH of 6.5 was acquired, denoted as Ca-DTPMP. The synthesis of zinc-DTPMP and zinc-BHPMP nanoslurry followed the same route as that of Ca-DTPMP except that surfactant TTAB was replaced by SDS in the reaction and denoted as Zn-DTPMP and Zn-BHPMP, respectively. For comparison, unmodified Ca-DTPMP and Zn-phosphonate precipitates were also synthesized in the absence of surfactant. Once fabricated, these nanofluids were utilized for column flow-through experiments, described below. The dry solid nanoparticles of each type of metal-phosphonate were obtained from a portion of the corresponding nanosuspension by centrifuging the suspension at 6000 rpm for 15 minutes. After the supernatant was discarded, the solid samples were dried in oven at 100 $^{o}$C overnight to remove the interstitial water and characterized by the following methods.

**3.1.3 Characterization method** The dried solids obtained from the centrifugation of the nanosuspension of Ca/Zn-phosphonate were characterized by X-ray diffraction (XRD) and Fourier Transform Infrared (FT-IR) and scanning electron microscopy (SEM). XRD patterns were recorded on a Ragaku D/max Ultra II Powder Diffractometer equipped with a Cu Kα radiation source at 40 KV and 40 mA. FT-IR spectra were obtained using a Nicolet FT-IR spectrometer with KBr pellet technique. The spectrometer range was 4000 to 400 $cm^{-1}$. The stoichiometric ratio of metal to phosphonate in each metal-phosphonate solid sample was determined by dissolving the pre-washed precipitates in 1N HCl and measuring the aqueous phase metal and phosphorus concentrations. SEM was carried out on FEI Quanta 400 ESEM FEG at 15KeV for particle morphology examination. As for the aqueous nanofluid, samples for transition electron microscopy (TEM) analysis were prepared by dispersing a certain amount of metal-phosphonate in deionized (DI) water and then dipping sample suspension onto a copper grid coated with amorphous carbon-holey film, which was air-dried overnight in room temperature. TEM analyses were carried out on a JEOL 2000 FX electron microscope at 130 KV to measure the particle size and to characterize the morphology of nanoparticle clusters.

**3.1.4 Nanoparticle column breakthrough experiments** Approximately, 12.5 gram calcite (Iceland spar, Creel Chihuahua, Mexico, 180-250 μm) or 12.4 gram Ottawa sand (Gibbstown, NJ) was packed into a Pharmacia glass column (GE

company), 10 cm by 1.0 cm ID. Total pore volume (PV) was calculated to be around 3.25 ml. Two 10 μm stainless steel screens (Vici Instrument Co.) were place at the front and end fitting of this column. A Gilson 305 HPLC pump (Gilson Inc.) was used to load the prepared nanofluids of metal-phosphonate with 2% KCl electrolyte into the column. The flow rate was about 60 ml/hr, which corresponded to a linear velocity of 45 m/day. In a typical run, roughly 25 ml of nanofluids containing 1.5% (wt/wt) phosphonate inhibitors was injected into the calcite column. The physicochemical parameters for migration of nanoparticles in column experiments are listed in Table 3.1.

Table 3.1 Summery of parameters for migration of nanoparticle in column experiments

| Parameters | Values |
|---|---|
| nanoparticle diameter | 150 nm |
| porosity | 0.4 |
| pH of nanofluid | 7.5 |
| electrolyte composition | 2% KCl |
| calcite particle radius | 180-250 um |
| column dimension | 10 cm by 1cm |
| flow rate | 45 m/day |

**3.1.5 Nanoparticles squeeze simulation** The laboratory squeeze simulation of nanoparticle placement was conducted similar to the procedure outlined by Shen et al[1]. Briefly, half of a pore volume (PV) of the prepared metal-phosphonate nanofluid (0.9%wt/wt as phosphonates) with 2% KCl was injected into a calcite column (8cm length, 1.6 cm ID) pre-saturated by solution composed of 1M NaCl and 0.01 M $NaHCO_3$, followed by 0.5 PV overflush with 1M NaCl. After 18 hr shut-in period in which the nanoparticle suspension left in the column attached onto the mineral surface, the column was eluted with synthetic brine (0.025M

$CaCl_2$, 0.015 M $NaHCO_3$ and 1M NaCl, sparged with 100% $CO_2$) from the opposite direction. The column experiments were conducted at 70°C and a linear flow velocity of 45 m/day. The effluent solution was collected and analyzed for phosphonate, calcium and zinc concentrations to establish the breakthrough curve (BTC) or flow back return curves.

**3.1.6 Analytical methods** Metals and phosphonates were analyzed by Inductively Couples Plasma-Optical Emission Spectrometer (ICP-OES) (Optima 4300 Dv, Perkin Elmer). The aqueous samples were diluted 10 fold for ICP measurement. Phosphonate was also measured spectrophotomically, where phosphonate was UV-persulfate oxidized to orthophosphate and formed a molybdophosphorus complex, which was reduced to phosphomolybdenum blue complex with ascorbic acid and measured spectrophotomically at 890 nm. The spectrophotometic method is able to measure phosphonate at 0.02 to 2.5 mg/L as phosphate, which corresponds to 0.024 to 3 mg/L as DTPMP and 0.029 to 3.6 mg/L as BHPMP.

## 3.2 Results and discussions:

### 3.2.1 Nanoparticle synthesis:

The morphology of both solid Ca and Zn-phosphonate nanoparticles have amorphous microporous structure composed of small particles of various irregular shapes (Fig. 3.1).

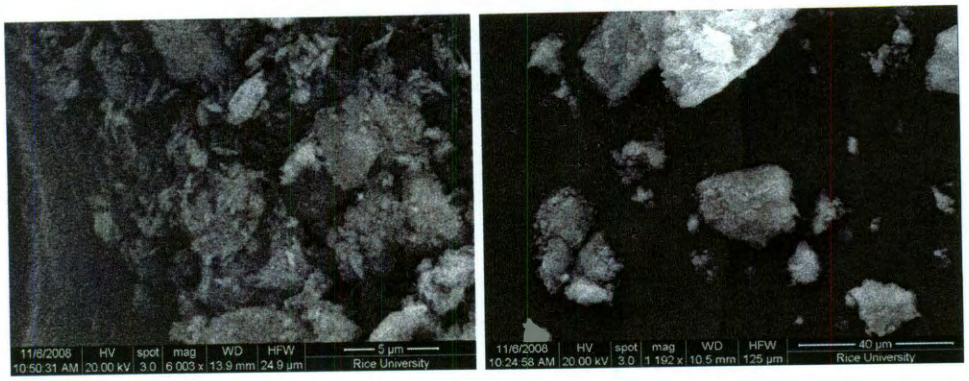


(a) (b)

Figure 3.1 (a) SEM image of the fabricated Ca-DTPMP nanoparticles in the presence of TTAB cationic surfactant; (b).SEM image of the fabricated Zn-DTPMP nanoparticles in the presence of SDS anionic surfactant.

The micromorphology and particle size were characterized by TEM images (Figure 3.2), where the morphology of the synthesized particles in the presence and absence of surfactant were compared. According to Fig. 3.2a, the morphology of Ca-DTPMP particles in the absence of surfactant was highly irregular and the particles tended to aggregate. By adding TTAB to the nanosuspension, particle size was reduced to 80-150 nm (Fig. 3.2b). The cationic surfactant controlled the hydrodynamic diameter of Ca-DTPMP, possibly due to increased electrostatic repulsion and reduced interfacial tension. The function of surfactant limiting the particle size was also found in the case of Zn-phosphonate. The surfactant free particles were in irregular shape with micron size (Fig. 3.2c); while SDS coated Zn-phosphonate nanoparticles were observed in spherical shape (Fig. 3.2d).

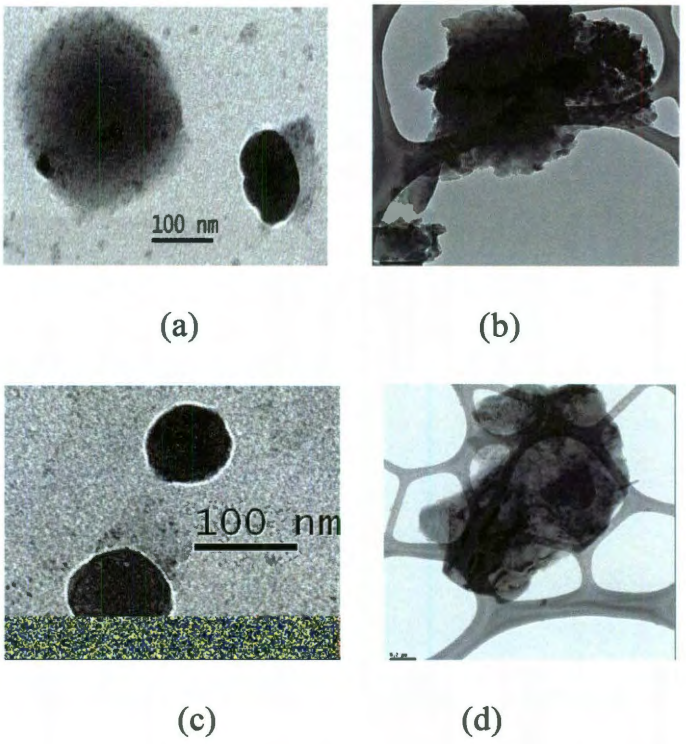


Figure 3.2 TEM microimages of synthesized Ca-DTPMP (a) Ca-DTPMP nanoparticles in the presence of TTAB cationic surfactant; (b) Ca-DTPMP precipitate without surfactant presence; (c) Zn-DTPMP nanoparticles in the presence of SDS anionic surfactant; (d) Zn-DTPMP precipitate without surfactant presence.

The fabricated metal-phosphonate nanoparticles were further studied by means of XRD and FT-IR analyses. Different from previous work[22], where the obtained precipitate was in amorphous state, the XRD patterns of both TTAB modified Ca-DTPMP and SDS modified Zn-DTPMP (Fig. 3.3), fabricated by surfactant assisted route, exhibited peaks at 2θ value of 31.7°, 45.5 °, 56.5 ° and 74.5 °. The crystalline size can be calculated according to the Scherrer formula[96]:

$$D_V = KL/(\beta \cdot \cos\theta) \qquad (3.1)$$

where $D_v$ represents the volume weighted crystalline size; K is the Scherrer constant in the range of 0.87-1.0; L denotes the wavelength of the radiation, which

is 1.54Å in this work and β is the integral breadth of a reflection located at 2θ. The crystallite sizes of the fabricated nanoparticles were calculated to be 17.9 nm and 18.3 nm for TTAB modified Ca-DTPMP and SDS modified Zn-DTPMP respectively. Compared with the reported crystal size of titania-phosphonate (EDTMP and DTPMP)[97], the crystallites acquired in this work were larger, probably due to the difference of coordination property between titanium and calcium/zinc and the effect of presence of surfactant. The fabricated solid of Ca and Zn-phosphonate nanoparticles were dissolved in 1N HCl to measure the stoichiometric ratio of cation to phosphonate and the results showed a ratio of 3.95 for Ca to DTPMP and 4.05 for Zn to DTPMP or BHPMP, suggesting that each solid was probably $M_4H_2$DTPMP (or BHPMP).

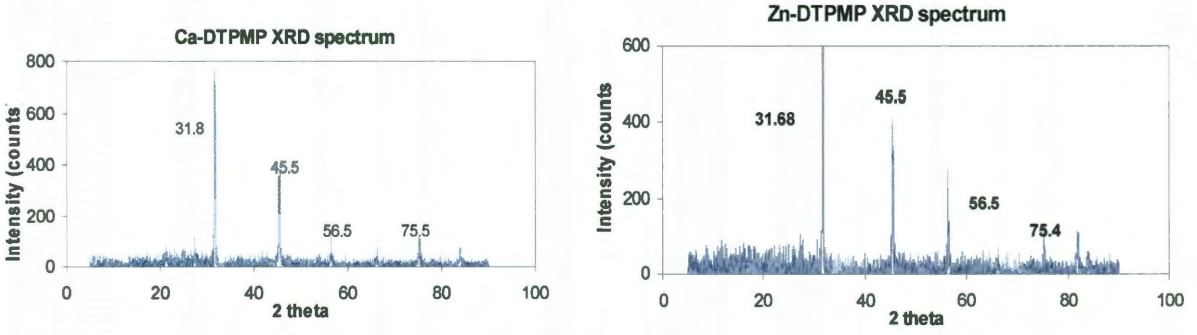


Figure 3.3 XRD patterns of (a) Ca-DTPMP nanoparticles; (b) Zn-DTPMP nanoparticles

During the synthesis process, surfactants play an important role in controlling the morphology of the obtained particles due to the fact that surfactants adsorb onto the particle surface and alter the interfacial tension[98, 99]. The initial stage of the

metal phosphonate precipitate formation is essentially a nucleation process, which according to the classic nucleation theory[44, 98] can be divided into three steps (illustrated in Figure 3.4): (i) the formation of a critical nucleus by interaction of molecules; (ii) the deposition of nuclei and the formation of crystallite and (iii) the formation of large crystals by crystal ripening. Heterogeneous nucleation is the predominant formation process for crystals in natural waters, because a large supersaturation is needed for homogeneous nucleation. As stated by Stumm and Morgan[44], among many factors attributing to influence the nucleation process, the interfacial energy is the most important factor determining both thermodynamics and kinetics.

$$X + X \leftrightarrow X_2$$
$$X_2 + X \leftrightarrow X_3$$
$$X_{m-1} + X \leftrightarrow X_m \,(\text{critial cluster})$$
$$X_m + X \rightarrow X_{m+1} \,(\text{nucleation})$$
$$X_{m+1} + X \rightarrow \text{crytal growth}$$

Figure 3.4 Illustration of the nucleation and crystal growth process (revised from Stumm and Morgan [100])

Also, surfactants can serve as surface coating materials to nanoparticles, in which their surfaces can be modified, leading to an improved transport performance of nanoparticles in porous media[28, 101]. As discussed by Rosen[99], the dispersion of a solid into a liquid can be described as a three-stage process, including (1) the wetting of the powder; (2) deaggregation of fragmentation of the particle clusters; (3) prevention of reaggregation of the dispersed particles. In the second step,

surfactants, if properly chosen, can adsorb in "microcracks in the solid" or cause the particle cluster to acquire an electrical charge; and, in the third step they can greatly reduce the solid-liquid interfacial tension, leading to a reduction of the tendency for dispersed particles to aggregate. Anionic surfactant can increase the surface charge of the iron particles and provide electrostatic repulsions between particles to inhibit aggregation[28], whereas non-ionic surfactant can supply enough steric barriers on the surface to stabilize the nanoparticles[101].

The FT-IR investigation of the nanoparticles can reveal the skeletal structure of the samples in solid state. The good overlapping of IR spectra of Ca-DTPMP samples with and without surfactant presence in the synthesis procedure testified that there was no significant surfactant residue left in the solid sample (Fig. 3.5). The band at 1633 $cm^{-1}$ and 1460 $cm^{-1}$ were assigned to the surface adsorbed hydroxyl group[102] and the C-H bending in $-CH_2-$ groups, respectively. The strong band at 1090 corresponds to the phosphonate $P-O\cdots M$ stretching[97]. The band at 936$cm^{-1}$ is due to the P-OH stretching, indicative of the existence of available coordination sites for phosphoryl oxygen with metal ion, which is in agreement with the available hydrogen presence in the formula of $Ca_4H_2$DTPMP, as discussed above. Such results are different from that of the titania-phosphonate hybrid, where the extensive condensation and coordination of phosphoryl oxygen leads to bidentate units[97].

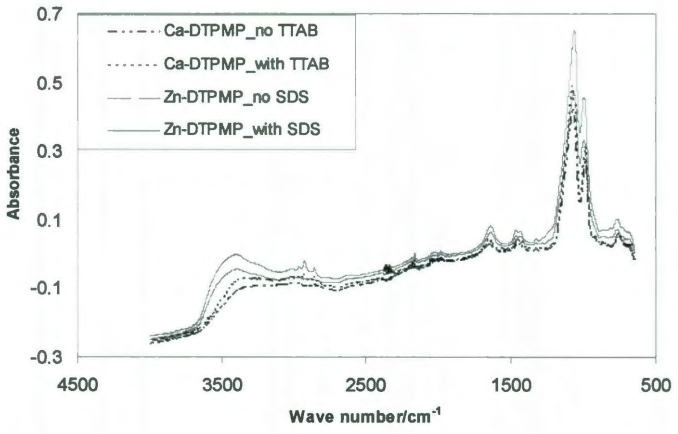


Figure 3.5 FT-IR spectrum of surfactant modified Ca-DTPMP and Zn-DTPMP nanoparticles

### 3.2.2 Nanoparticle transport in porous media:

The mobility of the surfactant coated and surfactant free Ca-DTPMP nanoparticles was investigated by a laboratory column study, in which the nanofluids were pumped through the porous media of sand, the predominant composition of sandstone, and calcite, which is assumed to be the most reactive component among the formation materials. Initially, a tritiated water tracer experiment was conducted to determine the pore volume of the packed column. The results revealed a porosity of approximately 0.4 for both sand and calcite columns. A typical flow through experiment was initiated by conditioning the column with 1 M NaCl solution until the effluent solution reached stable pH and then approximately 15 milliliters of metal-inhibitor nanofluids with 2% KCl were pumped through the column. The change in the normalized effluent particle concentration ($C/C_o$) as a function of number of pore volumes of the nanofluids flowed through the column is plotted in Fig. 3.6. The transport of unmodified Ca-

DTPMP and surfactant modified nanoparticles in calcite column was different (Fig. 3.6). There was no breakthrough for the unmodified Ca-DTPMP particles. Whereas, the surfactant TTAB modified Ca-DTPMP nanoparticles showed 100% breakthrough after around 1 PV of flow. Similar BTCs can be observed for Ca-DTPMP nanoparticles passing through sand column, indicating that the retardation of nanoparticles through the porous media was negligible. This argument can be further verified by fitting the experimentally obtained data to a one-dimensional advection/dispersion equation using CXTFIT program, assuming a local equilibrium and linear isotherm developed by Parker and van Genuchten[103]. Table 3.2 summarized the retardation factor and dispersivity values obtained from the CXTFIT program. The breakthrough curves of Ca-DTPMP in two types of porous media (Figure 3.6) showed that, with flow rate of 45 m/day, the Ca-DTPMP nanoparticles transport can be characterized with a retardation factor of 1.04 to 1.09 and dispersivity of 0.4 to 0.47 cm in sand and calcite media. Therefore, this type of nanoparticles shows a promise for the field application where nanoparticles can be injected into the formation materials and transport further away from the injection point.

Table 3.2 Summery of the retardation factor and dispersivity value obtained from the analytical modeling using CXTFIT code

| Conditions | R | Dispersivity (cm)* |
|---|---|---|
| $^3H_2O$ Tracer in calcite | 1 | 0.03868±0.0156 |
| Nanoparticles in sand media | 1.043±0.034 | 0.401±0.218 |
| Nanoparticles in calcite media | 1.091±0.029 | 0.474±0.162 |

* Dispersivity ( $\alpha \equiv D/v$ ) is characteristics of the porous medium.

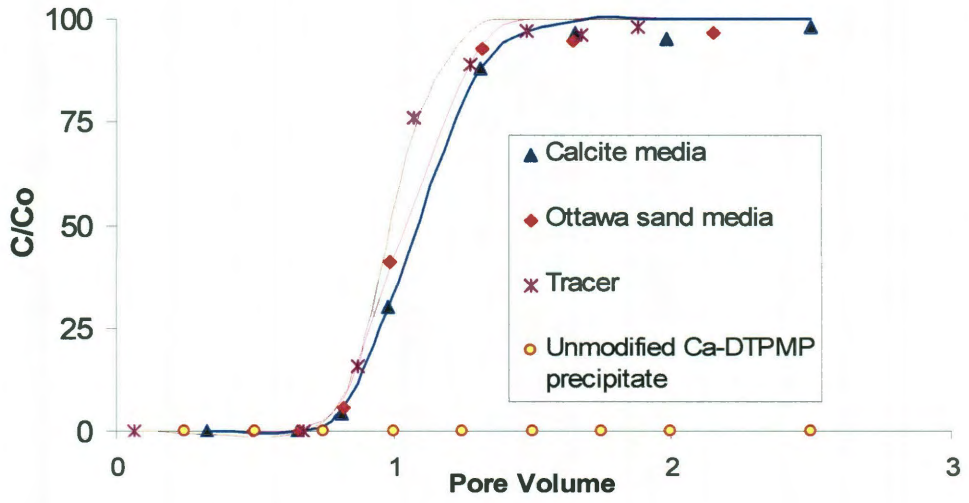


Figure 3.6 TTAB coated Ca-DTPMP nanoparticle breakthrough curves in calcite and sand porous media together with unmodified Ca-DTPMP precipitate in calcite media.

In another effort, based on the particle deposition theory, the transport of colloidal particles in the porous matrix is dominated by the collision of the particles with a matrix surface as well as the attachment of the particles to the matrix surface[104]. The parameters of single collector efficiency (η) and the particle attachment efficiency (α) were introduced to describe the above transport process. The attachment efficiency α, for the metal-phosphonate particle in the calcite and sand can be calculated from the observed normalized concentration of $C/C_o$ in the column test by the following equation[92]:

$$\alpha = -\frac{2d_c}{3(1-f)L\eta}\ln(C/C_o) \qquad (3.2)$$

where $d_c$ represents the diameter of a collector, which is assumed to be spherical. In this work, the diameter of the collectors of calcite and sand were roughly 200 μm. L stands for the length of the porous media (L=10 cm in this work), f is the

porosity of the media (f=0.4 in this work) and $C/C_o$ is the normalized effluent concentration where C and $C_o$ are the particle concentration present at distance L and L=0. The single collector efficiency ($\eta$) is a function of various physical parameters, including the flow velocity, porosity, collector grain size and temperature[93]. Several online calculators are available to calculate $\eta$ [105] and the value of $\eta$ as 0.0322 was obtained for the transport of fabricated nanoparticles through calcite with grain size of around 200 μm. Typically, for particles with size of hundreds nanometers, the predominant process in determining the fate of the particles is the brownian diffusion[44]. Based on equation (3.2) and the BTCs in Fig. 3.6, the values of $\alpha$ were calculated to be 0.0028 and 0.0014 for surfactant modified Ca-DTPMP nanoparticles through calcite and sand, respectively and 2.7 for non surfactant modified Ca-DTPMP in calcite. The fact that $\alpha$ for non surfactant modified Ca-DTPMP is larger than one is probably attributed to the uncertainty in the calculation of $\eta$ in this case. Obviously, the surfactant exerted a deciding influence in inhibiting the nanoparticles from being collected and removed by calcite media. In order to maintain the stability of clay materials in the downhole formation and avoid the formation damage, certain salinity is required to be added to the injection solution. The stability of the fabricated nanofluids with surfactant assisted synthesis route is greatly enhanced. The surfactant containing nanofluids with 2% KCl can be stable for one week. Furthermore, KCl did not limit the migration of nanoparticles, indicated by the above transport data.

### 3.2.3 Nanoparticle squeeze simulation:

The laboratory squeeze simulation is aimed at studying inhibitor placement in the formation by monitoring inhibitor return concentrations. Kan et al reported that a longer squeeze life was observed in acidic squeeze treatment, where most of the acidic inhibitors were retained near the wellbore, whereas more neutral inhibitors were able to migrate farther away from the wellbore but the squeeze life is shorter[9]. In Fig. 3.7a is plotted three inhibitor return curves: one of Ca-DTPMP nanoslurry of this study, one of Ca-DTPMP nanoslurry and one of acidic DTPMP pill in the previous work[22]. These three return experiments were carried out by injecting half a PV of scale inhibitor solution in 2% KCl and at active DTPMP concentrations of 0.9%, 0.9% and 0.8%, respectively. The difference between the return curves of Ca-DTPMP nanoslurry of this work and that of previous work may be attributed to the difference of formation matrix (calcite for this work and Frio formation sandstone for previous work) and also the surface coating materials (TTAB in this work versus polyphosphino-carboxylic acid in the previous work). When the acidic pill was injected into a sandstone media, only 450 pore volumes of flow were returned with phosphonate concentration above 0.5 mg/L. When Ca-DTPMP nanoparticles was injected, phosphonate return concentrations were above 1mg/L for over 1000 PV and 0.5 mg/L for over 2000 PV (Fig. 3.7a). It showed the similar patterns for the squeeze simulation of the fabricated Zn-phosphonate nanoparticles (Fig. 3.7b), where the initial effluent concentration was only around a few hundred milligrams per liter, indicating that majority of the

loaded nanoparticles attached to the surface of calcite minerals. BHPMP is one of the most effective barite inhibitors. However, BHPMP shows a much shorter squeeze life than that of DTPMP and other inhibitors[8]. In Figure 3.7b, we demonstrate that the squeeze life of SDS modified Zn-BHPMP nanoparticles was comparable to that of modified Zn-DTPMP nanoparticles. The slow release of the inhibitors from metal-phosphonate particles is controlled by a dissolution process, which leads to a phase transition phenomenon. Based on the solution speciation model proposed by Tomson et al[59], the negative logarithm ion product of $Ca_3H_4Phn$ (pIP=-log ($[Ca]^3[H]^4[Phn]$) is illustrated in Fig. 3.8. Clearly, DTPMP was transitioned from an amorphous solid to a crystalline phase with pIP similar to that reported previously by the author's research group. There was a long transition period between these two phases, where the amorphous precipitate gradually transformed to the crystalline state with much lower solubility. This accounts for the slow dissolution of the nanoparticles in the squeeze simulation process.

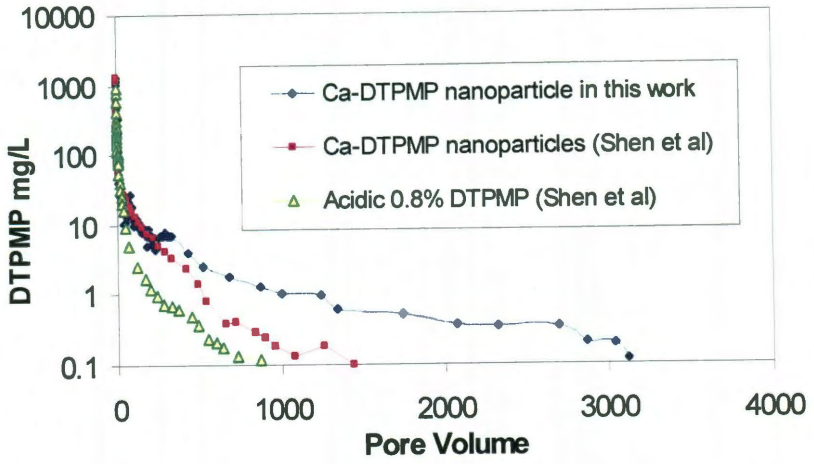


(a)

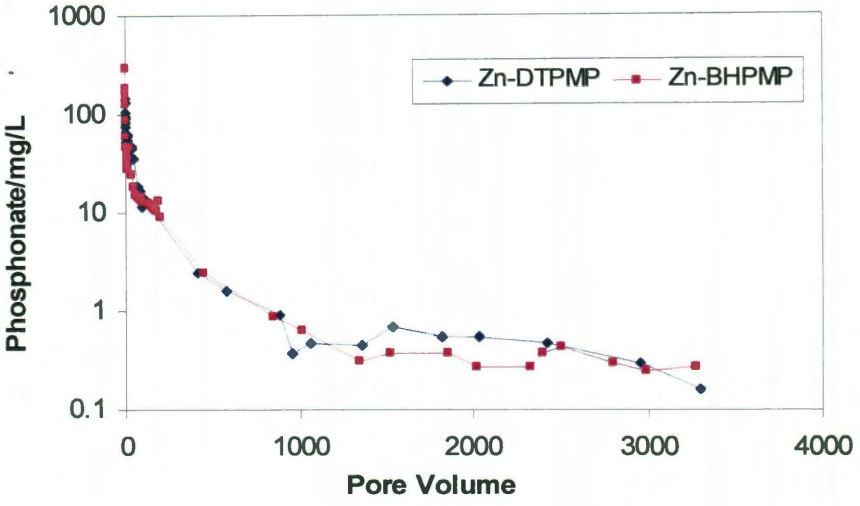


(b)

Figure 3.7 (a) The return curves of TTAB coated Ca-DTPMP nanoparticles in calcite media in this work; acidic DTPMP pill and PPCA coated Ca-DTPMP nanoparticles in sandstone media from Shen et al[22]; (b) The return curves of SDS coated Zn-DTPMP and Zn-BHPMP nanoparticles in calcite column in this study

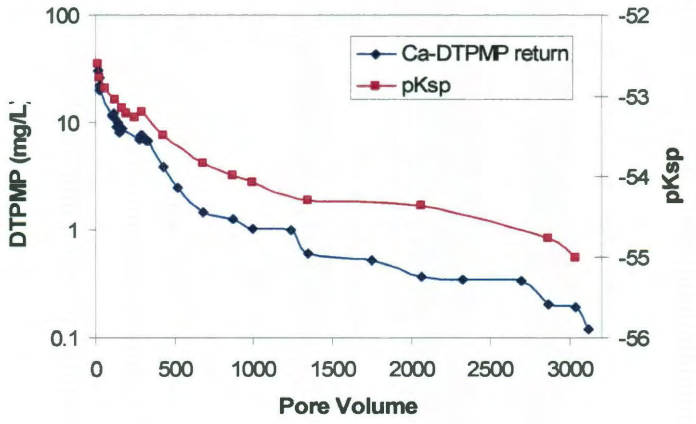


Figure 3.8 DTPMP concentration and calculated solubility product vs. number of pore volumes from the return of TTAB coated Ca-DTPMP nanoparticles in calcite column.

### 3.3 Conclusions:

In this work, surfactants modified nanoparticles of Ca-DTPMP, Zn-DTPMP and Zn-BHPMP were fabricated in a simple and economical manner where no external sonication energy input was needed. Surface characterization of the morphology of the above particles indicated that they were porous structured materials. The addition of surfactants as surface coating materials plays an important role in regulating the nanoparticles stability and morphology. Also, the adsorption of surfactants to particles enhanced their mobility in both calcite and sand based porous media, where nanoparticles showed similar migration ability as inert tracer. The potential application of synthesized nanoparticles in oil fields was tested by laboratory squeeze simulations, where phosphonate nanoparticles were delivered further away from the injection point and flow back at reasonable concentrations required to inhibit most scale formation for a large volume of production brine.

# CHAPTER FOUR
# SILICA-BASED ZINC-DTPMP INHIBITOR NANOMATERIALS[†]


## Abstract:

In this study, a silica templated synthesis route was adopted for fabrication of zinc-phosphonate nanoparticles to expand their use in the delivery of phosphonate inhibitors into formation core materials for scale control. Transition divalent metal $Zn^{2+}$ was chosen due to its ability to significantly increase inhibitor retention and effectiveness. Zinc chloride was first adsorbed onto the surface of 22 nm silica particles, followed by gradual addition of diethylenetriaminepentakis (methylenephosphonic acid) (DTPMP) to form nanometer sized particles in the presence of sodium dodecylbenzene sulfonate (SDBS) surfactant. The physical and chemical properties of the synthesized Si-Zn-DTPMP nanoparticle slurry (nanofluid) have been carefully evaluated. The nanofluid was stable at 70°C in 1 % KCl at pH 6.7 for over 12 hours. The transport of the synthesized nanofluid through calcite and sandstone formation porous media has been investigated using column breakthrough experiments and modeled with a 1-D advection-dispersion equation. The nanofluid was transportable through these media and near total breakthrough could be obtained by pre-flushing the media with an anionic SDBS surfactant solution. The diafiltration experiment was designated to transform the nanoslurry into a less soluble phase, and such materials demonstrated a much


[†] The content of this chapter has been accepted at *SPE J.* 2011. It was reproduced here as submitted and the only changes here are the numbering of tables and figures, which have been renumbered to adhere to the format of this thesis.

longer inhibitor lifetime compared to the untreated ones. The long-term flow back performance of the fabricated nanofluid was examined via a laboratory squeeze simulation test where the nanoparticles gradually returned phosphonate inhibitors in the flow back brine solution, and the normalized return volume was comparable to conventional squeeze treatment.

**4.1 Introduction:**

Scales are inorganic deposits resulting from brine solutions and scale formation is a significant problem in the oil and gas industry[1, 2, 4, 13, 45, 106]. The causes of scale formation depend on the scale of interest. For example, the precipitation of calcite (calcium carbonate) scale is due to pressure depletion that causes $CO_2$ degassing, while the primary causes of barite (barium sulfate) scale results from the mixing of incompatible waters in the reservoir[1, 2]. The most common and effective method to prevent scale formation is to deliver threshold scale inhibitors, e.g., phosphonates into the downhole formation via squeeze treatment. The squeeze treatment performance could be greatly improved by precipitation treatment, which is carried out by adjusting the solution chemistry to form inhibitor complexes. The precipitate solubility and the rate of release of inhibitors to the production brine control the inhibitor return concentration as well as the squeeze lifetime[13, 19]. However, the concern for the precipitation squeeze is the formation blockage induced by inhibitor salt formation near the wellbore[19]. Some recent advances in oilfield scale control technologies include the utilization of viscosified fluids and non-aqueous inhibitor solutions[54]. Viscosified fluids were investigated

to place scale inhibitors in target formation via bullheaded application[107, 108]. Non-aqueous scale inhibitor solutions were developed in order to avoid damages induced by the aqueous squeeze treatment[109-112].

As easily accessible hydrocarbons become less available, developments in offshore deepwater become more important for hydrocarbon production[113]. In the offshore deepwater production, scale formation is a serious flow assurance challenge with significant production reduction and high cost. The principle scale formation mechanisms in offshore production include: 1) the decrease in pressure at increased brine temperatures; 2) the mixing of two incompatible fluids and 3) the salt concentration increases induced by brine evaporation[8, 45, 114]. It will be of great advantage to develop a novel strategy to deliver the inhibitors into the downhole formation, control their placement and manage the return concentration with improved reliability, effectiveness and inhibitor lifetime. As an alternative to the conventional precipitation squeeze, the phosphonate inhibitors can be potentially delivered into the formation porous media via a nanofluid injection approach[22, 115]. The nanofluid is comprised of nanometer sized particles containing phosphonate inhibitors. In previous studies, two different synthesis strategies were deployed to fabricate metal-phosphonate nanoslurries by employing one polyarylate polymer and one surfactant as surface coating materials to regulate the surface morphology of the nanoparticles[22, 115]. The surface coating materials controlled size and altered the surface chemistry of the particles to inhibit particle

aggregation. The nanoparticles could then travel through the calcite porous medium to deliver the phosphonates to the target zones in column experiments. Moreover, the potential application of the fabricated nanoparticles was evaluated via laboratory squeeze simulation, where phosphonate inhibitors were returned slowly as flow back with synthetic brine.

Kan et al.[116] reported that the addition of the first transition element cations, e.g. zinc, in the phosphonate inhibitor pill solution could improve the inhibition efficiency and significantly enhance the squeeze lifetime of BHPMP inhibitors. The improved scale inhibition effect might be caused by the complex of transition metal with the amine group of the phosphonates. Zinc (borderline Lewis acid) with $3d^{10}$ subshell electrons could form complexes with phosphate, carboxylate and amine groups, the primary functional groups in the phosphonates. Regarding the metal ligand complexation: 1) the stability constants for zinc with the amines are much higher than that of phosphate or acetate[116, 117]; and 2) the stability constants of zinc with amines (glycine and ethylenediamine) are much higher than that of the alkaline earth ions, indicating the stronger covalancy in the complexes of zinc and the amines. Experimentally obtained data[118-121] confirms that the stability constants for the transition metal ions with three phosphonates of AMP, NTMP and EDTMP are much higher than for alkaline earth metal ions because of the presence of the amine groups in the molecular structure of these compounds. The strong interaction between the phosphonates and zinc may affect both the

properties of phosphonate inhibitors and the squeeze lifetime. Subsequently, zinc-phosphonate nanoparticles were prepared in this study in order to take advantage of the strong interaction between zinc and the amine groups of the phosphonates.

In oilfield scale treatment operations, a squeeze treatment is generally initiated by a preflush treatment where a surfactant solution is injected to increase the wetness of the formation and to condition the formation rock by altering the wettability to enhance the scale inhibitor retention[99, 122]. Moreover, due to its property of adsorption on rock surfaces, the surfactant is employed for foam propagation for enhanced oil recovery (EOR) applications. EOR foams are normally examined at surfactant concentrations in the range of 0.1–1%, which are above the critical micelle concentration (cmc) for most foaming surfactants in brine. It has been observed that the surfactant preflush could affect the inhibitor return concentrations. A scale inhibitor squeeze modeling study was carried out to simulate the surfactant preflush effect by considering the process reversibility, volumes of surfactant injected, and the adsorption of the surfactant to the rock surface[123]. In this study, the effect of anionic surfactant preflush to enhance inhibitor nanoparticles transport in formation core porous media will be discussed.

Recently, the silica template-based synthesis approach has been reported as a promising strategy in producing a variety of nanostructured materials, e.g., ordered mesoporous carbon thick films[29], cross-linked polymeric nanocapsules[31], palladium nanowires[32] and macroporous platinum[33]. During these synthesis

reactions, silica plays an important role in determining the structure and morphology of the fabricated nanoparticles as a structure directing agent. Silica nanoparticles can provide various porous frameworks with a wide range of pore sizes, well-defined morphology, and various chemical functionalities[29, 30]. As a continuation of our previous work, in this study a similar route was followed to fabricate the zinc-phosphonate nanoparticles by means of a silica templating method. The obtained nanofluids were flushed through calcite and sandstone core materials to evaluate their transport performance in these porous media. The designed silica-based zinc-phosphonate nanoslurry was further developed into a less soluble phase through diafiltration treatment. Finally, a laboratory squeeze simulation was carried out to test the potential application of the developed zinc-phosphonate nanoslurry.

## 4.2 Materials and methods:

**4.2.1 Chemicals** Commercial grade diethylenetriamine pentakis (methylenephosphonic acid) (DTPMP) with 50% activity was chosen as the scale inhibitor. Silica nanoslurry (30% wt/wt) with particle size of 22 nm and surface area of 135 $m^2/g$ was purchased from Nyacol Inc. (Ashland, MA). Chemicals such as zinc chloride, sodium chloride, nitric acid, sodium hydroxide, piperazine-1,4-bis (2-ethanesulfonic acid) sodium salt (PIPES) and sodium dodecylbenzene sulfonate (SDBS) were reagent grade and purchased from Fisher Scientific unless otherwise specified. Tritiated water was purchased from Sigma-Aldrich

(Amersham Co. Arlington Height, IL). Deionized water (DI water) was prepared by reverse osmosis followed by a four stage ion exchange water purification process, consisting of a high capacity cation/anion column, two ultra pure ion exchange columns and an organics removal column (Barnstead Internationals, Dubuque, IA).

**4.2.2 Silica-zinc-DTPMP nanofluid synthesis** In a typical synthesis experiment, a silica nanoslurry (5% wt/wt) was prepared by diluting a silica stock slurry with DI water and the slurry pH was adjusted to 4 with 1 N HCl. $ZnCl_2$ (0.3 M) was prepared in DI water and solution pH was adjust to 4.5 with 1 N HCl. The $ZnCl_2$ solution (16 ml) was added dropwise to the silica nanoslurry (50 ml) while the solution was vigorously stirred by a magnetic stirrer. The mixed Zn-silica slurry was heated to 70°C in a water bath and stirred for 15 min. A DTPMP solution (0.1 M) was prepared by diluting the DTPMP stock solution with DI water and the solution pH was adjusted to 9 with KOH. While the Zn-silica slurry was stirred, DTPMP (12 ml) was gradually added to the slurry using a syringe pump (Harvard Apparatus Inc., Holliston, MA). Immediately upon injection of DTPMP into the Zn-silica slurry, white Zn-DTPMP precipitates formed. Once the addition of DTPMP was completed, a SDBS solution (10% wt/wt, 3 ml) and PIPES powder (1 gram) were slowly added to the above mixture with continuously stirring. The formed Zn-DTPMP slurry was at ~6.7 pH with 1% KCl. Typically, the solution pH and the concentrations of dissolved $Zn^{2+}$ and DTPMP became stable after 15

minutes and remained constant for days. In order to further disperse the precipitates and stabilize the nanoslurry, the above Zn-DTPMP slurry was sonicated by a probe ultrasonicator (Sonics & Materials Inc., Newtown, CT) for 5 minutes to form a stable nanofluid. Once fabricated, the silica-zinc-DTPMP (Si-Zn-DTPMP) nanofluid was employed for the column flow-through experiments described below. The Si-Zn-DTPMP solids were separated by centrifuging the nanofluid at 8500 rpm for 15 minutes and then dried in an oven at 100°C overnight to remove the interstitial water and characterized by the following methods.

**4.2.3 Characterization method** Transition electron microscopy (TEM) analysis was carried out on a JEOL 2000 FX electron microscope at 130 KV. Samples for TEM analysis were prepared by dispersing a certain amount of nanofluids in DI water and then dripping sample suspension onto a copper grid coated with amorphous carbon-holey film. The dried solids obtained from the centrifugation of the Si-Zn-DTPMP nanoslurry were characterized by X-ray diffraction (XRD), Fourier Transform Infrared (FT-IR) and scanning electron microscopy (SEM). XRD patterns were studied on a Ragaku D/max Ultra II Powder Diffractometer equipped with a Cu Kα radiation source at 40 KV and 40 mA. FT-IR spectra were acquired on a Nicolet FT-IR spectrometer with KBr pellet technique with the spectrometer range of 4000 to 400 $cm^{-1}$. SEM was carried out on FEI Quanta 400 ESEM FEG at 15KeV for particle morphology examination.

**4.2.4 Nanoparticle column breakthrough experiments** Transport behavior of Si-Zn-DTPMP nanoparticles through core porous media was investigated through a series of column experiments. The experimental setup included a glass column, a syringe pump and a fraction collector similar to that of previous studies[22, 115]. The core materials in this study included calcite (Iceland spar, Creel Chihuahua, Mexico) and Berea sandstone (Vermillion, Ohio), both in the grain size range of 180-250 μm. These materials were first washed by 1mM acetic acid to remove fine particles and impurities, followed by DI water rinsing. The treated core materials were packed into an Omnifit column 0.66 cm ID, 7 cm length (Bio-Chem Fluidics, Boonton, NJ). Two 10 μm stainless steel screens (VICI Instrument Co., Houston TX) were placed at the front and end of this column to maintain core material particles inside the column. In order to achieve a uniform column packing and to prevent air entrapment, the column was saturated with 1M NaCl solution from the bottom and the porous medium was added from the top into the solution while the column was constantly tapped by a rubber rod until the column was fully packed. A non reactive tracer (tritiated water, $^3H_2O$) solution was injected into the column for ~3 pore volumes (PV). Following the tracer test, a Si-Zn-DTPMP nanoslurry transport experiment was carried out by flushing ~4 PVs of the inhibitor nanofluid through the column. The flow rates varied from 3 ml $hr^{-1}$ to 54 ml $hr^{-1}$, which correspond to linear flow velocities of 10 to 180 ft/day.

**4.2.5 Development of the prepared nanoslurry** Following the initial nanoslurry synthesis reaction, the Si-Zn-DTPMP precipitates were transferred to an Amicon stirred diafiltration cell (Amicon, Inc. Beverly, MA). The Amicon cell was equipped with a 100,000 molecular weight cutoff ultrafiltration membrane (Amicon YM 100) and a mounted suspended magnetic stirring bar for constant stirring. A stock solution of 0.8 M sodium chloride, 0.08 M sodium acetate and 0.1 M calcium chloride (5.5 pH) was prepared. The nanoslurry was diafiltered with 0.75 L of the calcium brine at 90 ml/hr flow rate and 70°C. During the diafiltration process, the solution in the diafiltration cell was forced through the ultrafiltration membrane at constant flow rate under pressure of around 5 psi. The solution inside the diafiltration cell was constantly refilled with the stock solution from a reservoir. In another experiment, a stock brine solution of 0.8 M sodium chloride, 0.08 M sodium acetate and 750 mg/L zinc as zinc chloride (5.5 pH) was prepared. A comparable amount of nanoslurry was added into the diafiltration cell and continuously diafiltered with 1.25 L of the zinc brine at a flow rate of 90 mL/h and 70°C in order to produce precipitates in a less soluble phase. The resulting materials were stored at 70°C as a suspension for the laboratory squeeze simulation experiment.

**4.2.6 Nanoparticles squeeze simulation** The developed Si-Zn-DTPMP nanoslurry from the diafiltration experiment was dispersed in a SDBS solution

(0.3% wt/wt) by a probe ultrasonicator (Sonics & Materials Inc., Newtown, CT) for 5 min. The laboratory squeeze simulation of nanoparticle placement was conducted in a procedure outlined in our previous study[115]. Briefly, at 70°C a calcite column (0.66 cm ID, 7 cm length) was saturated by a solution of 1M NaCl and 0.01 M $NaHCO_3$. Then, the column was flushed with a SDBS solution (0.3% wt/wt) for several PVs. Half of a PV of Si-Zn-DTPMP nanoslurry was injected into the column, followed by 0.5 PV overflush brine of 1M NaCl. After 24 hr shut-in period in which nanoparticles in the column were allowed to attach onto the mineral surface, the column was eluted with synthetic brine (0.025M $CaCl_2$, 0.015 M $NaHCO_3$ and 1M NaCl, sparged with 100% $CO_2$) from the opposite direction. The column experiments were conducted at 70°C and at a linear flow velocity of 135 ft/day. The effluent solution was collected and analyzed for solution pH, phosphonate, calcium and zinc concentrations.

**4.2.7 Analytical methods** Metals and phosphonates were analyzed by Inductively Coupled Plasma-Optical Emission Spectrometer (ICP-OES) (Optima 4300 Dv, Perkin Elmer). The aqueous samples were diluted for ICP measurement. Phosphonates were also oxidized to orthophosphate and formed phosphomolybdenum blue complex with ascorbic acid and measured spectrophotometrically at 890 nm wavelength[58]. Spectrophotometric method is able to measure phosphonate from 0.02 to 2.5 mg/L as phosphate, which corresponds to 0.024 to 3 mg/L as DTPMP.

## 4.3 Results and discussions:

### 4.3.1. Synthesis of Si-Zn-DTPMP nanofluid:

Variations in particle size and zeta potential in each step of the nanofluid synthesis procedure are illustrated in Fig. 4.1. The final nanoparticles were around 100 nm in diameter with a zeta potential of -55 mV. The surfactant modified nanofluid was stable for more than 12 hours. Silica nanoparticles were chosen as the template materials for metal-phosphonate nanofluid preparation due to low cost, absence of toxicity, low point-of-zero charge (pzc) of 2.5[124], and stability in aqueous solution. Initially, the diluted silica nanoparticles were 22 nm with a zeta potential of -25 mV (step 0, Fig. 4.1). The addition of HCl to the silica nanoslurry increased the particle zeta potential by neutralizing the negative charge on the particle surface (step 1, Fig. 4.1). When the $ZnCl_2$ solution was added to the silica nanoslurry, the $Zn^{2+}$ ions adsorbed onto the surface of the silica particles, indicated by the increase of zeta potential (step 2, Fig. 4.1). Formation of Zn-DTPMP precipitates was achieved by slowly adding DTPMP solution into the Zn-silica mixture (step 3, Fig. 4.1). The particle size of the Si-Zn-DTPMP nanoparticles was controlled by adding a SDBS surfactant solution into the above mixture (step 4, Fig. 4.1). Addition of SDBS surfactants not only regulated the particle size but also considerably reduced the zeta potential of the nanoparticles to below -50 mV (Fig. 4.1), which was stable against coagulation. The size of nanoparticles was further reduced to ~100 nm by ultrasonication treatment (step 5,

Fig. 4.1). Similar to the effect of the cationic and anionic surfactants on the fabricated metal-phosphonate nanoparticles in our previous study[115], the anionic SDBS surfactants controlled the hydrodynamic diameter of the Si-Zn-DTPMP particles by increasing the electrostatic repulsive interaction, and by reducing the interfacial tension of the fabricated nanoparticles[44, 99].

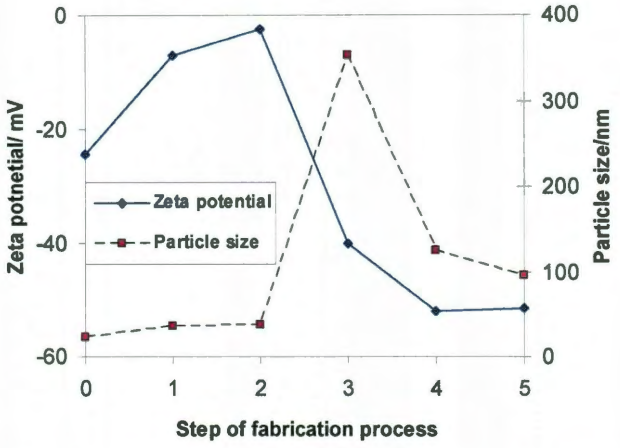


Figure 4.1 Zeta potential and particle size variations in five steps of nanoslurry synthesis
Step 0: Prepare 5% silica nanoslurry; Step 1: Adjust the silica nanoslurry pH to 4 with 1 N HCl; Step 2: Add $ZnCl_2$ solution to silica slurry; Step 3: Slowly add DTPMP solution to zinc-silica slurry; Step 4: Add SDBS solution and PIPES powder to the Si-Zn-DTPMP mixture; Step 5: Sonicate the Si-Zn-DTPMP slurry with an ultrasonic probe.

In Fig. 4.2 is plotted the TEM microimages of the Si-Zn-DTPMP precipitates. The Si-Zn-DTPMP precipitates in the absence of the surfactants were irregular in shape and particles tended to aggregate, while the surfactant modified nanoparticles were spherical and monodispersed. According to the SEM and XRD analysis (Fig. 4.3), the nanoparticle precipitates were amorphous solids. The skeletal structure of the obtained nanoparticle solids was investigated by FT-IR. In Fig. 4.4 is plotted the FT-IR spectra of the Si-Zn-DTPMP precipitates in the presence and absence of the surfactants and of Zn-DTPMP nanoparticle precipitates prepared previously[115]. The FT-IR spectra of different samples were similar, indicating that there was no substantial amount of surfactants left in the

solids and that the presence of silica did not affect the structure of the Zn-DTPMP precipitates.

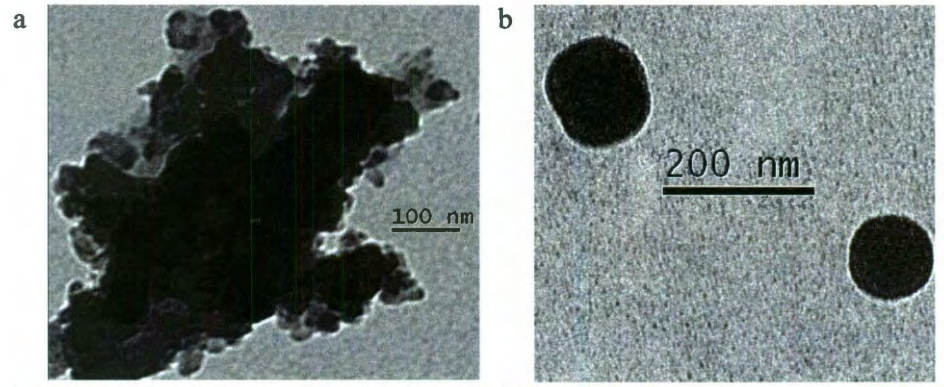


Figure 4.2 TEM microimages of the fabricated Si-Zn-DTPMP precipitates: (a) Si-Zn-DTPMP precipitates without SDBS surfactant; (b) Si-Zn-DTPMP nanoparticles in the presence of SDBS.

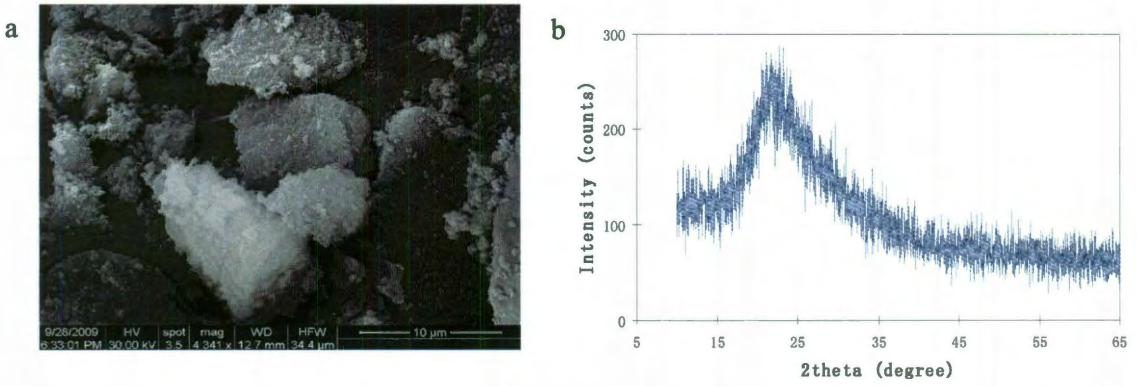


Figure 4.3 (a) SEM microimage of the Si-Zn-DTPMP solid; (b) XRD profile of the Si-Zn-DTPMP solid.

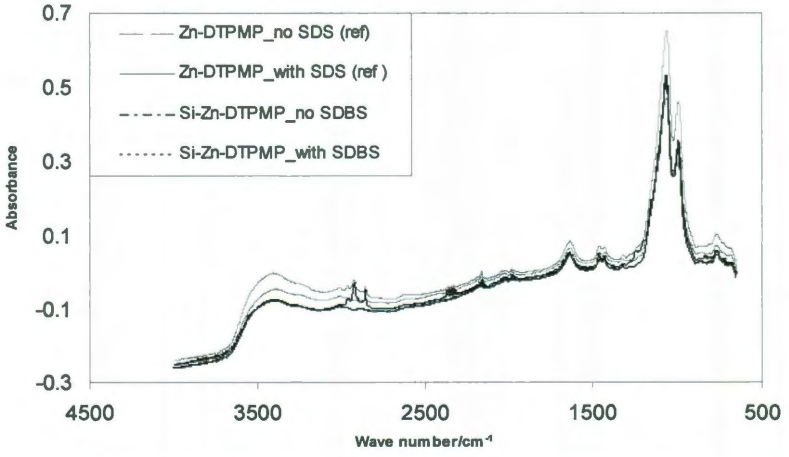


Figure 4.4 FT-IR spectrum of Si-Zn-DTPMP precipitates

### 4.3.2 Nanoparticles transport in porous media:

Initially, a tracer test was carried out to determine the PV and other physical parameters of the packed column. In Fig. 4.5a is plotted the breakthrough curves of the tritiated water (the tracer) through calcite and sandstone porous media. Table 4.1 summarizes the physical parameters of the porous media obtained from the tracer breakthrough tests. The hydrodynamic dispersion coefficient (D) in each porous medium was acquired by fitting the 1-D advection-dispersion equation (ADE) to the experimentally obtained data using CXTFIT code, assuming the retardation factor of one. The pore velocity was approximately 3.5 cm $min^{-1}$ in the two porous media. The dispersion coefficient (D) in the calcite medium was lower than that in the sandstone medium, indicative of lower dispersion in calcite. The calculated D values in this study were comparable to the results reported in the study of the transport of carboxymethyl cellulose stabilized iron nanoparticles through several glass beads and sandy materials with similar linear flow rates[90].

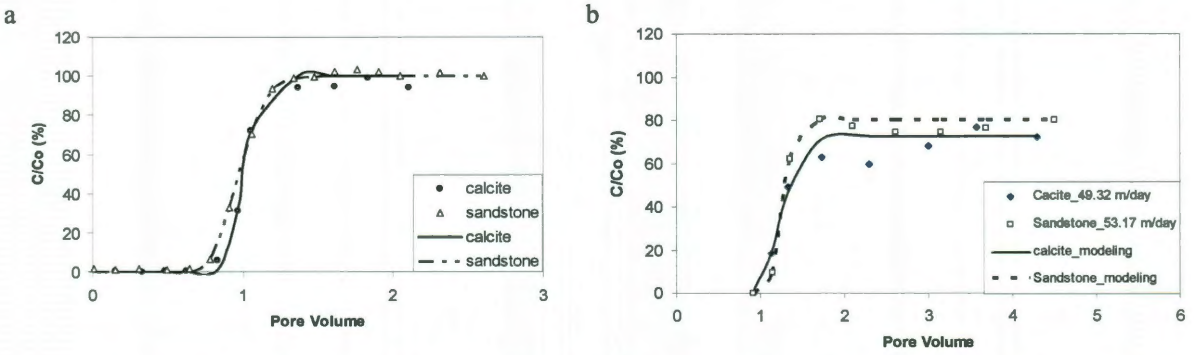


Figure 4.5 Breakthrough curves of (a) $^3H_2O$ tracer and (b) Si-Zn-DTPMP nanoparticles in calcite and sandstone porous media. Curves are CXTFIT model results.

Table 4.1 Properties of the porous media and parameters from the tracer tests

| Porous medium | Particle size (μm) | Porosity, ε | Pore Velocity, v (cm $min^{-1}$) | dispersion coefficient, D ($cm^2$ $min^{-1}$) | $r^2$ |
|---|---|---|---|---|---|
| Calcite | 180-250 | 0.427 | 3.425 | 0.0877±0.056 | 0.994 |
| Sandstone | 180-250 | 0.451 | 3.692 | 0.280±0.051 | 0.999 |

The nanoparticle breakthrough curves (BTC) can be established by plotting the change in the normalized effluent nanoparticle concentrations as a function of the number of PVs. The nanoparticle concentrations were reported by measuring the total phosphorous concentrations in the aqueous solution as determined by ICP. Based on the BTCs of the Si-Zn-DTPMP nanoparticles through two types of porous media under similar flow rates (Fig. 4.5b), the effluent nanoparticle concentrations reached a plateau at around 2.5 PVs with different breakthrough levels ($C/C_o$). Such behavior indicates that the nanoparticles were removed at a constant rate in each medium and the removal is controlled by a first-order kinetic mechanism[78, 80, 90].

The transport of particles through porous media has been studied extensively and several modeling work has been accomplished to quantify such processes[80, 92, 125-127]. In this study, the transport of nanoparticles through the porous medium can be described by the following ADE with an additional term to express for the first-order removal[78, 79, 128]:

$$R\frac{\partial C}{\partial t} = D\frac{\partial^2 C}{\partial x^2} - v\frac{\partial C}{\partial x} - J_d C \qquad (4.1)$$

where C (mg $L^{-1}$) is the nanoparticle concentration at a given time; t (min) is the time; D ($cm^2$ $min^{-1}$) is the dispersion coefficient; x (cm) represents the distance

downstream; v (cm $min^{-1}$) is the linear velocity or pore velocity; and $J_d$ ($min^{-1}$) denotes the removal rate coefficient. A retardation factor R is included in Eq. 4.1 to account for the retardation effect arising from the adsorption of nanoparticles to the porous medium:

$$R = 1 + \frac{\rho}{\varepsilon} K_d \tag{4.2}$$

where ρ (g $ml^{-1}$) is the density of the porous medium; $K_d$ ($cm^3$ $g^{-1}$) denotes the distribution coefficient of the nanoparticles between the solid and aqueous phases; and ε represents the porosity of the medium. While migrating through the porous medium, the nanoparticles were removed by the porous medium at a constant removal rate, $J_d$ ($min^{-1}$), which can be calculated based on the filtration theory[80, 81]:

$$J_d = -\frac{v}{L} \ln(C_e / C_o) \tag{4.3}$$

where L (cm) is the length of the porous medium; $C_e$ (mg $L^{-1}$) is the steady-state effluent concentration of the nanoparticles; and $C_o$ (mg $L^{-1}$) is the influent nanoparticle concentration. Based on the linear flow rate values listed in Table 4.1 and the $J_d$ values from Eq. 4.3, the R values were determined by fitting Eq. 4.1 to the nanoparticle BTCs via CXTFIT code. The values of each parameter obtained from CXTFIT fitting are listed in Table 4.2a.

According to Table 4.2a, at similar pore velocities, the transport of Si-Zn-DTPMP nanoparticles reached a higher breakthrough level in the sandstone medium. The nanoparticles also experienced a lower level of retardation effect in sandstone,

even though the R value for the other media was comparable. The $J_d$ values were also lower in sandstone than in calcite, indicative of less hindrance in the sandstone medium. Calcite is the most reactive component in the downhole formation[4]. The experimentally used sandstone was a mixture of different types of minerals, including quartz, feldspar, ankerite, clay and kaolinite[106]. Based on the reported data of the dissolution rates of different minerals[44, 129, 130], it can be stated that the dissolution rate of calcite is considerably higher (four to five orders of magnitude) than that of silicates at pH=7. Therefore, it can be assumed that the calcite medium released more mobile calcium ions into the pore space solution when flushing the Si-Zn-DTPMP nanofluid through the core materials. The released calcium ions then formed precipitates with the aqueous phase phosphonate species, which delayed the migration of the nanoparticles in the calcite medium.

Table 4.2a. Parameters for the breakthrough experiments and modeling fitting results without surfactant preflush

| Porous medium | Flow rate ($ml\ hr^{-1}$) | Pore velocity, v ($cm\ min^{-1}$) | Dispersion coefficient, D ($cm^2\ min^{-1}$) | BT levels, $C/C_o$ | Retardation factor, R | Removal rate , $J_d$ ($min^{-1}$) | $r^2$ |
|---|---|---|---|---|---|---|---|
| Calcite | 37.54 | 3.425 | 0.303 | 0.724 | 1.576 | 0.157 | 0.963 |
| Sandstone | 34.51 | 3.693 | 0.0914 | 0.799 | 1.276 | 0.119 | 0.990 |

Table 4.2b. Parameters for the breakthrough experiments and modeling fitting results of surfactant preflush effect

| Porous medium | Flow rate ($ml\ hr^{-1}$) | Pore velocity, v ($cm\ min^{-1}$) | Dispersion coefficient, D ($cm^2\ min^{-1}$) | Breakthrough levels, $C/C_o$ | Retardation factor, R | removal rate , $J_d$ ($min^{-1}$) | $r^2$ |
|---|---|---|---|---|---|---|---|
| Calcite | 38.07 | 4.347 | 0.315±0.258 | 0.971 | 1.327±0.169 | 0.0024 | 0.962 |
| Sandstone | 27.18 | 2.908 | 0.200±0.066 | 0.996 | 1.007±0.016 | 0.0002 | 0.993 |

### 4.3.3 Enhanced nanoparticle breakthrough by surfactant preflush

The effect of surfactant preflush on nanoparticle transport in porous media was examined in column experiments by flushing the porous media with a 0.3% (wt/wt) SDBS surfactant solution for ~7 PVs prior to the nanoparticle injection (Fig. 4.6). The experimental data were fitted with the ADE using CXTFIT code and the modeling results are summarized in Table 4.2b. Compared to the transport experiments without a SDBS preflush wherein the breakthrough levels were 0.72 and 0.79 (Table 4.2a), nearly total breakthrough in each porous medium could be obtained after surfactant preflush. The surface charge of the minerals in aqueous solution is affected by many experimental conditions, including solution pH, partial pressure of $CO_2$, the presence of metal ions and ionic strength. The pzc of calcite is around 8 pH and the pzc for sandstone is about 6 pH at the condition of $P_{CO2}=10^{-3.5}$ atm and 0.1 M ionic strength[131-133]. At the experimental condition of 6.7 pH, the calcite surface should be positively charged and sandstone surface charge would be close to neutral. The anionic surfactant SDBS adsorbed to the mineral surface and modified the mineral surface chemistry, with charge reversal occurring. This charge reversal enhanced the electrostatically repulsive interaction between the surface and the nanoparticles, which were also negatively charged (Fig. 4.1). Similarly, Shen et al.[22] observed that the transport of Ca-DTPMP nanoparticles through the calcite porous medium was considerably enhanced in the presence of anionic PPCA, while the majority of the precipitates were collected by calcite at the front side of the column in the absence of PPCA. It was

assumed that the surface charge of calcite reversed from positive to negative as a result of adsorption of PPCA, which improved the repulsive interaction between the nanoparticles and the surface and decreased the deposition rate of Ca-DTPMP in the porous media.

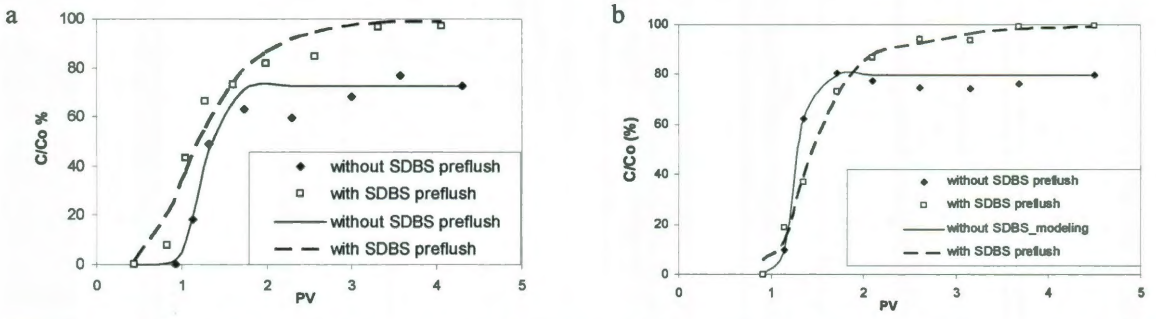


Figure 4.6. Surfactant preflush enhanced nanoparticles transport in two porous media of (a) calcite, (b) sandstone. Curves are CXTFIT model results.

On the other hand, hydrophobic moieties of fatty acids or surfactants may block the surface groups at the mineral surface, thus retarding mineral dissolution[44]. Hoskin et al.[134] proposed that the polyalkoxy sulfonate surfactants can be utilized as scale inhibitors and the surfactant molecules adsorbed onto the active sites on the surface of scale nuclei to prevent scale formation. Moreover, extensive studies[8, 9] on NTMP inhibitors interaction with formation rocks revealed that approximately twenty layers of phosphonate coverage on calcite surface can retard calcite dissolution. The retarded calcite dissolution leads to less divalent metal ions released into solution and the formation of more soluble calcium phosphonate solids. In this study, the SDBS surfactants may have adsorbed onto the surface of the porous media and inhibited the mineral dissolution, leading to less metal ions released into the pore space solution.

### 4.3.4 Diafiltration and transformation of Si-Zn-DTPMP nanoslurry:

It has been reported that the highly soluble Ca-DTPMP precipitates obtained via a precipitation experiment could be transformed into a much less soluble phase through a diafiltration process[58]. In this study, a similar strategy was followed to develop the Si-Zn-DTPMP precipitates into a less soluble phase by means of diafiltration with brine solution. Table 4.3 summarizes the physicochemical conditions of each diafiltration experiment. The brine solution pH was adjusted to 5.5, controlled by acetate buffer, and the temperature was controlled at 70°C by a water bath. The Si-Zn-DTPMP nanoslurry prepared by the silica-templated synthesis route without diafiltration treatment is denoted as Type I slurry. In Exp. #1, a Type I Si-Zn-DTPMP slurry containing 17.3 mg DTPMP was diafiltered by a $Ca^{2+}$ brine solution (0.8 M NaCl, 0.08 M NaAc and 0.1 M $CaCl_2$ at 5.5 pH). According to the diafiltration profile of the Type I nanoslurry (Fig. 4.7a), the effluent phosphonate concentrations kept at ~100 mg/L level for about 0.2 L of brine flushing and then drop swiftly to a sub-mg $L^{-1}$ level. After diafiltration for 0.2 L of brine, about 13.8 mg of DTPMP was washed out of the diafiltration cell, which accounts for 80% of the inhibitors added to the cell.

Table 4.3. Conditions and the results of each diafiltration experiment

| Exp # | Diafiltration conditions | | | | | | After diafiltration | | | |
|---|---|---|---|---|---|---|---|---|---|---|
| | Flow rate (ml/hr) | $Ca^{2+}$ conc. (M)[a] | $Zn^{2+}$ conc. (mg/L)[a] | S Solution pH | Temperature (°C) | DTPMP added (mg) | $V_{30}$[b] (L) | $V_{50}$[b] (L) | $V_{80}$[b] (L) | % of inhibitor left |
| 1 | 90 | 0.1 | 0 | 5.5 | 70 | 17.30 | 0.065 | 0.11 | 0.20 | <7% |
| 2 | 90 | 0 | 750 | 5.5 | 70 | 16.72 | | | | >90% |
| 3 | 90 | 0.1 | 0 | 5.5 | 70 | 17.67 | 0.19 | 0.31 | 0.45 | <5% |

[a]Both $Ca^{2+}$ and $Zn^{2+}$ concentrations listed here are the species concentrations in the stock brine solutions;
[b]$V_{30}$, $V_{50}$ and $V_{80}$ denote the volumes of brine solution flushed when 30%, 50% and 80% of total added phosphonates flushed out of the cell.

The results indicated that Si-Zn-DTPMP precipitates in Type I slurry demonstrated a fairly high solubility in the $Ca^{2+}$ brine solution, and a considerable amount of the solids was washed away by the brine solution. After the diafiltration experiment, more than 93% of the total added phosphonates were dissolved and flushed out of the diafiltration cell, indicated by the fact that initially turbid slurry inside the diafiltration cell turned clear and transparent. The release of the phosphonate inhibitors from the metal-phosphonate precipitates in the brine solution was controlled by a dissolution process[1, 2]. The nanoslurry contained zinc-DTPMP solids with a stoichiometry of $Zn_4H_2DTPMP$, hence the corresponding negative logarithm of ion product (pIP) should be:

$$pIP = -\log_{10}[(Zn^{2+})^4\{H^+\}^2(DTPMP^{10-})] \qquad (4.4)$$

where parentheses refer to molar concentration and braces for activity. $Zn^{2+}$ and $DTPMP^{10-}$ species concentrations were calculated from the total concentration of zinc and phosphonate through a speciation model[116]. In Fig. 4.7a is plotted the calculated seventh root of the negative logarithm of ion product as a function of the volumes of brine flushing in order to facilitate comparing numerical values for solids with different number of ions in the formula. The monoionized ion product value $pIP_n$ can be defined as the $n^{th}$ root of the IP:

$$pIP_n \equiv IP^{1/n} \qquad (4.5)$$

where "n" is the total number of ions in the product.

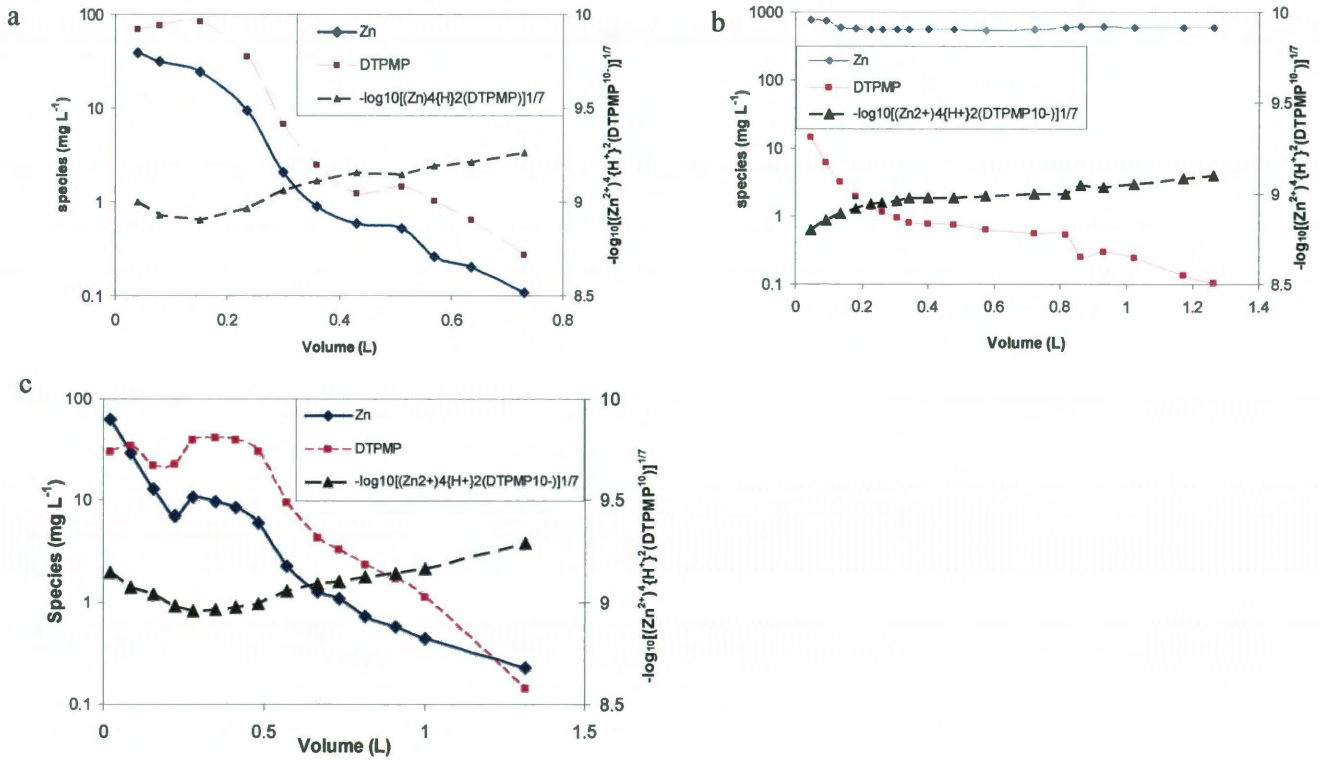


Figure 4.7. Diafiltration profiles of Si-Zn-DTPMP nanoslurries (a) Type I slurry flushed with $Ca^{2+}$ brine; (b) Development of Type I slurry with $Zn^{2+}$ brine to Type II slurry; (c) Type II slurry flushed with $Ca^{2+}$ brine.

In a separate experiment (Exp. #2), Type I nanoslurry with a similar dose of phosphonates was diafiltered by a synthetic $Zn^{2+}$ brine solution (0.8 M NaCl, 0.08 M NaAc and 750 mg/L $Zn^{2+}$ as $ZnCl_2$ at 5.5 pH) (Fig. 4.7b). During the diafiltration process, the filtrate phosphonate concentrations decreased exponentially as diafiltration proceeded. Contrary to Exp. #1, after 1.25 L of the filtrate was collected, the amount of phosphonates dissolved in the brine solution was only 10% of the input amount. The remaining slurry in the diafiltration cell after the experiment was still milky and turbid, indicating a substantial amount of solids with lower solubility. Based on the concentrations of $Zn^{2+}$ and the phosphonates, the pIP values with the progress of the diafiltration were calculated, displayed in Fig. 4.7b. In the course of the experiment, the seventh root of pIP values increased from 8.7 to 9.2, indicating that the solid gradually developed into a less soluble phase with ion product two orders of magnitude lower than that of the initial phase. This nanofluid is denoted as Type II slurry. The above results indicate that there are two different types of Si-Zn-DTPMP solids with different solubilities. A similar phase transition phenomenon was also observed by Kan et al[58], where amorphous phase Ca-DTMP slurry was diafiltered by a large volume of $Ca^{2+}$ brine. The solid developed into a crystalline phase with solubility product two to three orders of magnitude lower.

In Exp. #3, a Type II slurry obtained from Exp. #2 was diafiltered by the $Ca^{2+}$ brine for comparison to the dissolution of Type I slurry in Exp. #1. Comparable

amounts of phosphonates were employed in these two studies. The diafiltration profile (Fig. 4.7c) illustrated that, compared with the Type I slurry, the aqueous phase DTPMP concentrations in the initial stage (0~0.3 L flushing) were much lower than those in Exp. #1, indicating that the solubility of the Type II solids in $Ca^{2+}$ brine was much lower than that of the Type I solids. In Table 4.3, the volumes of the brine solution needed to dissolve certain amounts of phosphonates were compared. The brine solutions needed to dissolve 30%, 50% and 80% of the totally added phosphonates were 0.065 L, 0.11 L and 0.20 L for Type I slurry and 0.19 L, 0.31 L and 0.45 L for Type II slurry, respectively. Moreover, it took twice the amount of brine solution to reduce the phosphonate concentration to 0.1 mg/L compared with Exp #1, indicative of a much longer inhibitor lifetime in brine solution. The flow back performance and inhibitor lifetime of the developed nanofluid in calcite core materials will be further discussed in detail below.

### 4.3.5 Laboratory squeeze simulation:

Long-term flow back performance of Type II Si-Zn-DTPMP nanoparticles was evaluated by a laboratory squeeze simulation test where the inhibitor nanofluid was placed in the core materials and the phosphonate return concentrations were monitored. Table 4.4 summarizes the experimental results of the Type II Si-Zn-DTPMP nanofluid in this work and the Zn-DTPMP nanofluid in the previous study[115] for comparison. Parameters including the total mass injected, the mass returned in the first 3 PVs, and the total mass returned at the end of the experiment

were recorded in Table 4.4. In Fig. 4.8 is plotted the inhibitor return curves of both Si-Zn-DTPMP and Zn-DTPMP nanofluids. The inhibitor return curves in the initial 600 PVs are plotted in Fig. 4.8a and the entire return curves in Fig. 4.8b. These two nanoparticle return experiments were accomplished by loading half of a PV of phosphonate inhibitor nanofluids into calcite porous media and returning the inhibitors with the synthetic brine solution. The percentage retention is defined as the percentage of inhibitor retained after 3 PVs return, compared in Table 4.4, where more than 99% of DTPMP were retained in this study and 95% in the previous study. Moreover, according to the comparison of the nanofluids return in the first 600 PVs (Fig. 4.8a), the Zn-DTPMP nanoparticles in the previous study returned phosphonate inhibitors at initial effluent concentrations around threefold of that of the Si-Zn-DTPMP nanoslurry. The slow release phenomenon of the squeezed Si-Zn-DTPMP nanoparticles indicated that the majority of the nanoparticles were affixed to the calcite surface. The return profiles between 100 to 600 PVs showed that the return concentrations of Zn-DTPMP nanoparticles rapidly dropped to around 1mg/L, while Si-Zn-DTPMP returned phosphonates at 20 mg/L for another 200 PVs and then gradually descended to several mg/L as inhibitor return proceeded. With regard to the long-term flow back performance of nanoparticles (Fig. 4.8b), the phosphonate return concentrations of the Si-Zn-DTPMP nanoparticles were above 1 mg/L for over 2000 PVs and to 0.5 mg/L for over 3800 PVs, whereas, in the previous study, the phosphonate concentrations dropped to 1mg/L within only 500 PVs and to 0.5 mg/L for ~1000 PVs. If the

minimum inhibitor concentration (MIC) was assumed to be 0.5 mg/L, which is commonly encountered in the oilfield, a normalized squeeze lifetime (NSL) can be calculated from the ratio of effective return volumes and the mass of inhibitors injected, as defined in the literature[116]. According to Table 4.4, the NSL for Zn-Si-DTPMP nanofluid was greatly enhanced compared with its counterpart. The return performance of the Type II nanoslurry in the squeeze simulation test was consistent with that in diafiltration experiments. In both cases, developed Si-Zn-DTPMP precipitates displayed a much lower solubility than the undeveloped Zn-DTPMP precipitates.

Table 4.4. Summary of the squeeze simulation tests

| Nanofluids | Mass injected (mg) | Mass returned in 3 PV (mg) | Total Vol. returned (L) | % retention | % returned at the end | NSL (bbl/kg)[b] |
|---|---|---|---|---|---|---|
| Si-Zn-DTPMP | 14.96 | 0.072 | 4.27 | 99.50 | 95.98 | 1635 |
| Zn-DTPMP[a] | 31.96 | 1.53 | 17.56 | 95.20 | 90.89 | 924 |

[a]Data from Zhang et al.[115]

[b]NSL was calculated by assuming the MIC of 0.5 mg/L.

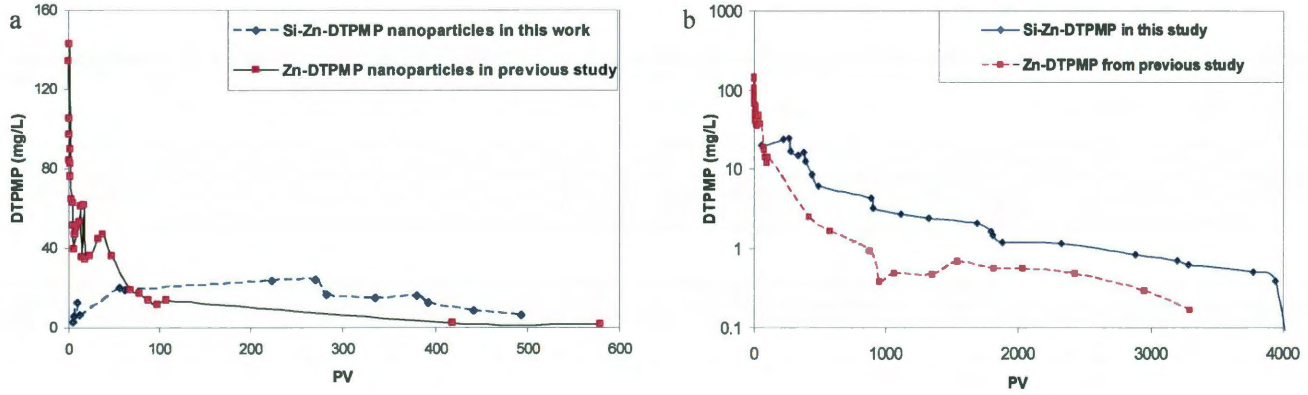


Figure 4.8. Squeeze simulation return profiles of two types of nanofluids in calcite columns: (a) return curves within the initial 600 PVs; (b) entire return curves up to 4000 PVs.

The release of phosphonate inhibitors from nanoparticles is controlled by the dissolution process of metal-phosphonate precipitates, which can be illustrated using a solution speciation model[116]. According to Fig. 4.9, with the progress of inhibitor return, the seventh root of pIP was not apparently altered with an average value of around 9.25, demonstrating no obvious phase transition phenomenon. In the previous study[115], an amorphous phase Ca-DTPMP nanoslurry was injected into a calcite core for squeeze simulation test. The Ca-DTPMP precipitate was gradually transformed into a crystalline phase indicated by the decrease of pIP in inhibitor return. However, in this study the Si-Zn-DTPMP nanoparticles employed in the return experiment were pre-developed via the diafiltration with $Zn^{2+}$ brine into a less soluble phase, which was at a thermodynamically favorable state. In the course of inhibitor return, the stable form of Si-Zn-DTPMP slowly dissolved phosphonate inhibitors into the brine solution until the end of the squeeze simulation process.

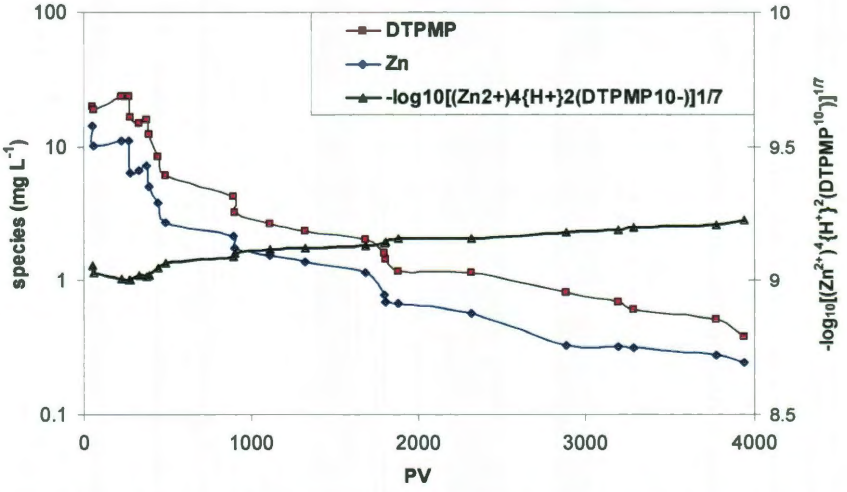


Figure 4.9. DTPMP and $Zn^{2+}$ return concentrations and the calculated seventh root of negative logarithm of ion product versus the number of PVs of synthetic brine return.

## 4.4 Conclusions:

The Si-Zn-DTPMP nanoparticles were fabricated by means of silica templated route. The transport of the nanoparticles in calcite and sandstone porous media was investigated by column tests; these nanoparticles exhibited reasonable migration performance in these core materials. The transport of nanoparticles in porous media can be enhanced by pre-flushing the media materials with a surfactant solution. Moreover, the obtained nanoparticles can be further developed into a less soluble phase via diafiltration with a large volume of zinc brine solution. The diafiltration experiments showed that the nanoparticles with lower solubility demonstrated a better flow back performance compared to the undeveloped materials. The squeeze simulation test of the developed nanoslurry indicated that the inhibitor long-term flow back performance and squeeze lifetime have been improved as well.

# CHAPTER FIVE
# CRYSTALLINE CALCIUM-DTPMP NANOMATERIALS: TRANSPORT IN CARBONATE AND SANDSTONE POROUS MEDIA[‡]

**Abstract:**

Phosphonates are widely used scale inhibitors in oilfield for scale control. In this study, crystalline phase calcium-phosphonate nanomaterials were prepared from an amorphous silica templated calcium-phosphonate precipitates, which were matured into crystalline phases via a simple diafiltration process. The crystalline solids were further dispersed into a surfactant solution to form a nanomaterial suspension (nanofluid) by ultrasonic treatment to expand its use in the delivery of phosphonate inhibitors into formation core materials for scale control. The physical and chemical properties of the synthesized crystalline nanomaterials have been characterized by chemical analysis, electron microscopy, X-ray diffraction, infrared microscopy and thermogravimetric analyses. The transport of the synthesized nanofluids through calcite and sandstone media has been investigated using laboratory column breakthrough experiments. The nanofluids were transported through these media with different breakthrough levels. The experimental transport data were correlated using an advection-diffusion equation as well as the colloid filtration theory with emphasis on the flow velocity effect on the particle transport. The maximum transport distance of the nanomaterials in

[‡] The content of this chapter has been accepted at *Ind. Eng. Chem. Res.* (2011). It was reproduced here as submitted and the only changes here are the numbering of tables and figures, which have been renumbered to adhere to the format of this thesis.

porous media was estimated based on the flow velocity and the particle attachment efficiency.

## 5.1 Introduction:

Scale formation is often a persistent problem in petroleum-production operations. Mineral scale deposits form in the formation near the perforation and on the surfaces of tubings and facilities, leading to significant hydrocarbon production reduction and financial cost[1, 2]. Scaling issues are more challenging as oil and gas production is from deeper and tighter formations to fulfill the increasing worldwide demand of hydrocarbons. For example, in offshore deepwater developments scale formation may become a serious flow assurance challenge[113, 114]. Of many available techniques to control scale formation, chemical treatment utilizing scale inhibitors has been widely applied and proven to be successful and economical. Phosphonates are one of the most commonly used threshold scale inhibitors in that they are capable of efficiently preventing scale formation at concentrations of several milligrams per liter or less. Phosphonates are delivered into downhole formation via a chemical squeeze protocol wherein inhibitor pill solutions are squeezed into formation rocks, followed by brine or diesel overflush to place the inhibitors farther into the formation to attach to the mineral surface by sorption or precipitation[8, 45]. During production phosphonates are gradually released into production water to prevent scale formation. The success of scale inhibitor treatments largely depends on the interaction of the inhibitors with

formation rocks[8, 45], which governs the migration, placement and return of the inhibitors and hence the success of squeeze operations. As proposed by Kan and Tomson[8-10, 45], the interaction mechanism is sorptive at low phosphonate concentrations and becomes precipitation of inhibitor salts at higher inhibitor concentrations. Several downhole physiochemical conditions, including inhibitor concentrations, solution pH and binding capacity with divalent cations can affect the squeeze treatment results[15, 16, 135]. Jordan el al[13, 17]and Tomson et al[8, 9, 45] concluded that the precipitate solubility plays an essential role in determining the inhibitor return concentrations and the treatment lifetime. In a conventional squeeze, an acidic pill solution will dissolve metal ions from the formation minerals, mainly calcium carbonate. The dissolved carbonate will react with the solution protons and thereby raise the pH. The dissolved calcium ions at higher pH will rapidly precipitate with phosphonate inhibitors near the wellbore, leading to limited transportability of the inhibitors into the formation.

In order to enhance the mobility of the phosphonate inhibitors in the formation matrix and to manage the inhibitor flow back performance, several methods have been developed to prepare metal-phosphonate nanomaterial suspensions and to utilize them for laboratory scale control tests in porous media[22, 115, 136]. The synthesized nanomaterials were stabilized by employing either a polymer-based surface active material or several types of surfactants, as surface coating materials. These materials can control the morphology and modify the surface chemistry of

the nanomaterials by altering the surface charge and interfacial tension of the metal-phosphonate particles. The nanofluids flowed through carbonate and sandstone porous media and delivered the phosphonate inhibitors into the target zone in column experiments. The release of the phosphonates was controlled by a dissolution mechanism and the phosphonates were gradually dissolved from the metal-phosphonate complexes into the brine solution for scale control. In this study, calcium ions precipitated with a common phosphonate inhibitor, diethylenetriamine pentakis (methylene phosphonic acid) (DTPMP), to produce calcium-DTPMP nanomaterials by using silica nanomaterials as templates. Silica nanomaterials were chosen due to the low point-of-zero charge of 2.5[124], and stability in aqueous solutions. The resultant nanomaterials were surface modified by an anionic surfactant, sodium dodecylbenzene sulfonate (SDBS), to modify the surface chemistry of the inhibitor particles.

The transport of inhibitor nanomaterials through porous media is of great significance since such processes determine the fate and placement of inhibitors in the formation. The capture of nanomaterials from bulk fluid to the matrix surface is due to (1) chemical reactions within the aqueous phase (e.g., adsorption, complexation, precipitation, dissolution) and (2) the transfer of nanomaterials to the medium surfaces. In the present paper, the transport of inhibitor nanomaterials through calcite and sandstone was evaluated via a series of laboratory column flow-through experiments. The experimental transport data were interpreted using

advection-diffusion and filtration theories to gain insight into the interaction of nanomaterials with the formation core materials.

The crystallization process is generally composed of three major steps: nucleation, crystal growth and ripening[43, 44]. Nucleation corresponds to the formation of critical clusters (nuclei) and subsequently lattice ions deposit on these nuclei and form crystallites via crystal growth. The large crystals form from fine crystals by a ripening process. Reddy and Nancollas[137] investigated the crystallization of calcium carbonate in the presence of magnesium and observed that the initially formed amorphous calcium carbonate (ACC) transformed into aragonite and calcite crystals. It was proposed that the initial short-lived hydrated ACC phase transformed into an intermediate transient form of ACC, and finally matured into the biogenic crystalline calcite phase in a tortuous path through preexisting amorphous units via a secondary nucleation mechanism. Similarly, it is widely accepted that amorphous calcium phosphate is the metastable precursor for the formation of thermodynamically more stable hydroxyapatite at neutral pH and moderate supersaturations[138-141]. Similar to the crystallization process of calcium phosphates, Kan et al[58] reported that the amorphous phase Ca-DTPMP precipitates acquired from a precipitation experiment could be transformed into crystalline solids with more than two orders of magnitude lower solubility via a diafiltration process. Following a similar experimental procedure, the silica based Ca-DTPMP precipitates were developed with a synthetic brine to produce the crystalline phase

solids. The conversion of amorphous phase silica-based Ca-DTPMP solids into crystalline materials through a diafiltration process is reported.

## 5.2 Experimental Section:

**5.2.1 Chemicals** Commercial grade diethylenetriamine pentakis (methylene phosphonic acid) (DTPMP) with 50% activity was used as the scale inhibitor, depicted in Fig. 5.1. Silica nanoslurry (30% wt/wt) with silica nanoparticle size of 22 nm and surface area of 135 $m^2 g^{-1}$ was purchased from Nyacol Inc. (Ashland, MA). Chemicals such as calcium chloride, sodium chloride, sodium acetate, hydrochloric acid, potassium hydroxide, piperazine-1,4-bis (2-ethanesulfonic acid) sodium salt (PIPES) and sodium dodecylbenzene sulfonate were reagent grade and purchased from Fisher Scientific. Tritiated water was purchased from Sigma-Aldrich. Deionized water (DI water) was prepared by reverse osmosis followed by a four stage ion exchange water purification process, consisting of a high capacity cation/anion column, two ultra pure ion exchange columns and an organics removal column (Barnstead Internationals, Dubuque, IA).

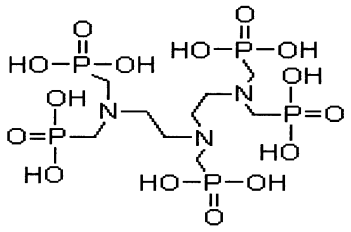

Figure 5.1 Structure of DTPMP molecule with the fully protonated form.

### 5.2.2 Silica-calcium-DTPMP nanofluid synthesis:

**5.2.2.1 Formation of silica-calcium-DTPMP slurry** In a typical synthesis experiment, a silica nanoslurry (5% wt/wt) was prepared by diluting a silica stock slurry with DI water and the slurry pH was adjusted to 4.5 with 1N HCl. $CaCl_2$ (0.4 M) was prepared in DI water and solution pH was also adjusted to 4.5 with 1N HCl. The $CaCl_2$ solution (15 ml) was added dropwise to the silica nanoslurry (10 ml) while the solution was vigorously stirred by a magnetic stirrer at room temperature. The mixed Ca-silica slurry was heated to 70°C in a water bath and stirred for 15 min. A DTPMP solution (0.1 M) was prepared by diluting the acidic DTPMP stock solution with DI water and the solution pH was adjusted to 9 with 10 M KOH. While the Ca-silica slurry was stirred at 70°C, 15 ml of DTPMP stock solution was gradually added to the slurry using a syringe pump (Harvard Apparatus Inc., Holliston, MA). Immediately upon injection of DTPMP into the Ca-silica slurry, white Ca-DTPMP precipitates formed. Once the addition of DTPMP was completed, a biological pH buffer, PIPES powder (0.5 gram) was slowly added to the above mixture with continuous stirring to adjust the solution pH to approximately 6.7. Typically, the solution pH and the concentrations of dissolved $Ca^{2+}$ and DTPMP became stable after 30 minutes and remained constant for several days. The resultant nanosuspension was stored at 70°C for 30 min.

**5.2.2.2 Development of the crystalline phase slurry** Following the initial slurry synthesis reaction, the obtained silica-calcium-DTPMP slurry was transferred to

an Amicon stirred diafiltration cell (Amicon, Inc. Beverly, MA). The diafiltration is a combination of dialysis and filtration. The Amicon cell was equipped with a 100,000 molecular weight cutoff ultrafiltration membrane (Amicon YM 100) and a mounted suspended magnetic stirring bar for constant stirring. A stock solution with composition of 0.8 M sodium chloride, 0.08 M sodium acetate and 0.1 M calcium chloride (5.5 pH) was prepared and used as a reservoir. During the diafiltration process, the solution in the diafiltration cell was forced through the ultrafiltration membrane at a constant flow rate of 95 ml $hr^{-1}$ under pressure of around 5 psi at 70°C. The solution inside the diafiltration cell was constantly refilled with the stock solution from the reservoir. After the diafiltration process, about 70% of the initially added calcium phosphonate solids were developed into a more stable phase, which was confirmed by X-ray to be crystalline solid. Detailed discussion regarding this process is in the following section. The crystalline suspension was centrifuged at 8500 rpm for 20 min. The supernatant was discarded and the solid samples were washed thoroughly with DI water to remove the residual salt and saved as a wet paste.

**5.2.2.3 Nanoslurry formation via ultrasonic dispersion** The nanomaterial suspension was obtained by dispersing the resulting solids, acquired from the centrifugation step, into a surfactant solution via ultrasonic dispersion. A solution containing 20 mM SDBS, 35 mM KCl and 10 mM PIPES was prepared. The crystalline solid (1 g) was dispersed in 50 ml of the above solution by a probe

ultrasonicator (Sonics & Materials Inc., Newtown, CT) at 100 Watt for 30 minutes to form a stable suspension. The silica-calcium-DTPMP (Si-Ca-DTPMP) nanofluid was equilibrated by rotation in a tumbler for three days. Before characterization or transport studies, the nanofluid was sonicated for 15 minutes. A portion of the Si-Ca-DTPMP solids were separated by centrifuging the nanofluid at 8500 rpm for 20 minutes and then dried in an oven at 60°C overnight to remove the interstitial water and were characterized by the following methods.

**5.2.3 Characterization methods** The dried solids obtained from the centrifugation of the Si-Ca-DTPMP nanoslurry were characterized by various means including X-ray diffraction (XRD), Fourier transform infrared (FT-IR) spectroscopy, scanning electron microscopy (SEM) and thermogravimetric analysis (TGA). The XRD characterization was carried out on a Ragaku D/max Ultra II Powder Diffractometer equipped with a Cu Kα radiation source at 40 KV and 40 mA. The FT-IR spectrum was analyzed using KBr pellet technique with the spectrometer range of 4000 to 400 $cm^{-1}$ using a Nicolet FT-IR spectrometer. The SEM microimages were collected on FEI Quanta 400 ESEM FEG, equipped with energy-dispersive X-ray spectrometer (EDAX). TGA was carried out using a thermal analysis instrument SDT 2960. Samples were heated at rate of 10°C $min^{-1}$ from 25°C to 1100°C in an atmosphere of flowing argon (100 ml $min^{-1}$). Eletrophoretic mobility of the Si-Ca-DTPMP nanofluid was measured using a Zeta-PALS instrument (Brookhaven Instruments Corporation, Holtsville, NY).

Zeta-potential was obtained by fitting the eletrophoretic mobility via the Smoluchowski equation[142]. The nanomaterial particle concentrations were determined by dissolving the nanomaterials in nitric acid solution and measuring the total phosphorus concentration in the aqueous solutions. Calcium, silica and phosphonate concentrations were analyzed by inductively coupled plasma-optical emission spectrometer (ICP-OES) (Optima 4300 Dv, Perkin Elmer). The wavelengths for calcium, silica and phosphorus measurements are 317.933, 251.611 and 213.617 nm, respectively. A solution containing 5 mg $L^{-1}$ yttrium (371.029 nm) was used as internal standard solution. Each sample measurement was repeated five times and the mean value of these measurements was reported. The standard deviation for each sample measurement was less than 1 %.

**5.2.4 Laboratory column breakthrough experiments** Transport of the Si-Ca-DTPMP nanomaterials through formation porous media was investigated through a series of column experiments. The experimental setup included a glass column, a syringe pump and a fraction collector similar to that of previous studies[22, 115]. The porous solid materials employed in this study were calcite (Iceland spar, Creel Chihuahua, Mexico) and Louise sandstone, both in the grain size range of 106-180 μm. Louise sandstone was collected at Louise Well, Frio formation located in Galveston County, TX (9107-9110 ft). The composition of the Louise sandstone was less than 1% calcite, several percentage clay and over 90% quartz[143]. These materials were washed by 1 mM acetic acid to remove fine particles and

impurities, followed by DI water rinsing. The medium materials were packed into an Omnifit column 0.66 cm ID, 7 cm length (Bio-Chem Fluidics, Boonton, NJ). Two stainless steel screens with pore size of 10 μm (VICI Instrument Co., Houston TX) were placed at the front and end of this column to maintain the porous medium particles inside the column. In order to achieve a uniform column packing and to prevent air entrapment, the column was saturated with 1M NaCl solution from the bottom and the porous medium was added from the top into the solution while the column was constantly tapped by a rod until the column was fully packed. A non reactive tracer (tritiated water, $^3H_2O$) solution was injected into the column for approximately 2 pore volumes (PV). Following the tracer test, a Si-Ca-DTPMP nanoslurry transport experiment was carried out by flushing about 4 PV of the inhibitor nanofluid through the column. The phosphonate concentrations in the inhibitor nanofluid for transport experiments were between 0.2-0.3 % (wt/wt). The flow rates varied from 0.064 to 1.45 ml $min^{-1}$, corresponding to linear pore velocities of 0.45 to 9.4 cm $min^{-1}$.

## 5.3 Results and discussion:

### 5.3.1 Diafiltration and transformation of Si-Ca-DTPMP slurry:

Table 5.1a summarizes the physicochemical conditions of the diafiltration experiments. The brine solution temperature was controlled at 70°C by a water bath and pH was adjusted to 5.5 in the presence of acetate buffer, which is considered to be inert with respect to complexation with calcium ions. The

elemental ratio of the acquired crystalline Si-Ca-DTPMP solids from ICP-OES analysis is Si:Ca:P=4:3:5 and hence, the stoichiometry of the developed solid is $Si_4$-$Ca_3H_4$DTPMP, which is comparable with the result of EDAX analysis of Si:Ca:P of 2:1:2 (Fig. 5-SI1 in supporting information), considering the semiquantitative nature of the EDAX analysis. Such observations are similar to the previous study, where the developed Ca-DTPMP crystalline solid was in the form of $Ca_3H_4$DTPMP[58].

Table 5.1a Experimental conditions of the diafiltration experiment

| Experimental conditions | |
|---|---|
| flow rate (ml/hr) | 95 |
| NaCl conc. (M) | 0.8 |
| $Ca^{2+}$ conc. (M)[a] | 0.1 |
| acetate conc. (M) | 0.08 |
| solution pH | 5.5 |
| temperature (°C) | 70 |
| DTPMP added (mg) | 400.38 |

[a] $Ca^{2+}$ concentration is dictated by the calcium concentration in the stock brine solution (0.1 M).

In light of the fact that the silica nanoparticles were utilized as the templating materials in the synthesis process, they are not considered to be involved in the acid/base dissolution reaction of the calcium-DTPMP solids. The release of the phosphonate inhibitors from the calcium-phosphonate precipitates in the brine solution was controlled by a dissolution process[1, 2], which can be characterized by the ion product. With regard to Ca-DTPMP in this study, the calculated negative logarithm of ion product (pIP) is:

$$pIP = -\log_{10}[(Ca^{2+})^3\{H^+\}^4(DTPMP^{10-})] \quad (5.1)$$

where parentheses refer to molar concentration and braces to activity. The $DTPMP^{10-}$ species concentrations were obtained from the total aqueous phase

phosphonate concentrations through a speciation model, which considers the acid/base and complex solution chemistry as a function of pH, temperature and ionic strength[116]. During the diafiltration process, the effluent concentrations of DTPMP decreased by two orders of magnitude from ~580 to 5 mg $L^{-1}$ (Fig. 5.2), leading to an increase of the corresponding pIP values from 50.18 to 52.22, which was close to that of the crystalline Ca-DTPMP precipitate (52.92) at comparable experimental conditions in a previous study[58]. The increase of the pIP values indicated the formation of a less soluble phase solid out of the amorphous material. The SEM microimages (Fig. 5.3) of these two types of solids reveal that the more soluble precipitate has amorphous morphology and the developed material is crystallized with rod-shaped structure. The XRD spectra (Fig. 5.4) provide further evidence for the amorphism and crystallinity of the undeveloped and developed Si-Ca-DTPMP solids, respectively.

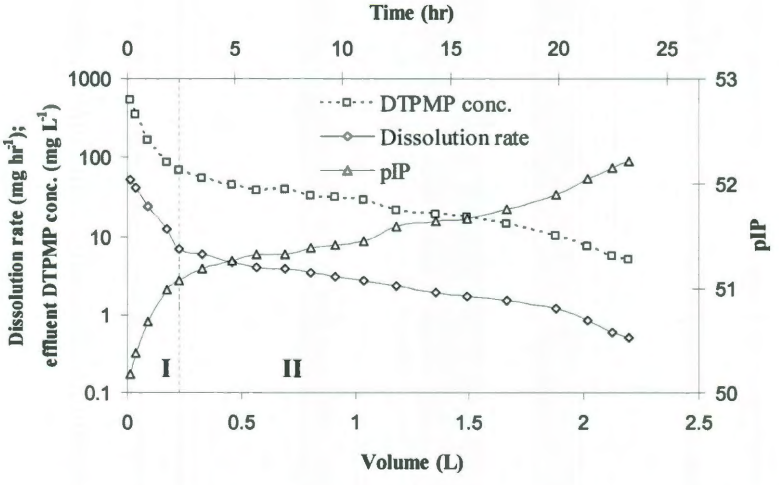


Figure 5.2. Diafiltration profiles of the silica based Ca-DTPMP slurry with brine solution, including effluent phosphonate concentration, dissolution rate and pIP variation as a function of the diafiltration volume and time. The dash dividing line between the Regions of I & II is located at 2.41 hr (0.23 L) of synthetic brine flushing.

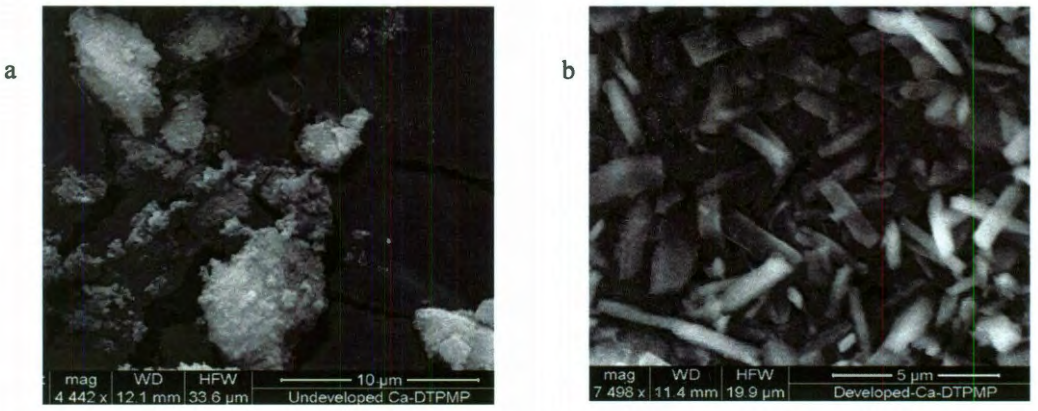


Figure 5.3. SEM microimages of (a) amorphous phase Si-Ca-DTPMP solid before diafiltration and (b) crystalline phase Si-Ca-DTPMP solid after the diafiltration treatment and sonication dispersion in surfactant solution.

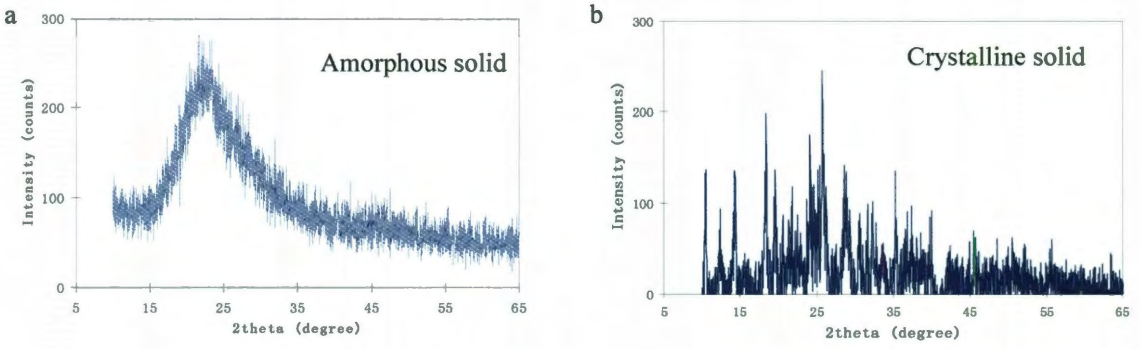


Figure 5.4 XRD profiles of (a) amorphous phase Si-Ca-DTPMP solid before diafiltration and (b) crystalline phase Si-Ca-DTPMP solid after diafiltration treatment.

Moreover, the diafiltration profile of the Si-Ca-DTPMP precipitate (Fig. 5.2) illustrates that the Si-Ca-DTPMP dissolution process can be characterized with two regions: "fast-dissolution" (I) and "slow-dissolution" (II) regions. As shown in Fig. 5.2 and summarized in Table 5.1b, the effluent phosphonate concentration dropped from 542.35 to 69.23 mg $L^{-1}$ within 0.23 L brine flushing in Region I (2.41 hr); while the DTPMP concentration dropped from 69.23 to 4.98 mg $L^{-1}$ in 1.97 L brine flushing (20.78 hr) in Region II. The calculated phosphonate

dissolution rate also displayed a similar pattern. By the end of the diafiltration experiment, about 70% of the added Ca-DTPMP precipitates developed into crystalline phase through diafiltration with a total of 2.19 L of synthetic brine within 23.2 hr. During the process of phase transition via diafiltration treatment, the initially formed amorphous solid can be regarded as the precursor phase of the crystalline precipitate. In Region I, the dissolution of the amorphous precursor took place simultaneously with the nucleation and growth of crystalline particles via internal structure rearrangement. The course of structure rearrangement and crystal growth proceeded to Region II until the majority of the Ca-DTPMP precipitates were converted into crystalline ordered structures. Further investigation is needed to obtain deeper insight of such phase transition processes.

Table 5.1b. Experimental results of the diafiltration experiment

| (b) Experimental results | | |
|---|---|---|
| Region I: | $V^a$ (L) | 0.23 |
| | $m^b$ (mg) | 45.48 |
| | $t^c$ (hr) | 2.41 |
| Region II: | $V^a$ (L) | 1.97 |
| | $m^b$ (mg) | 50.26 |
| | $t^c$ (hr) | 20.78 |
| At the end | % of inhibitor left | 71.84% |

[a]V denotes the volume of brine flushed in each region;
[b]m is the mass of phosphonates flushed out of the diafiltration cell in each region.
[c]t is the time of brine flushed in each region.

### 5.3.2 Characterization of the crystalline Si-Ca-DTPMP nanomaterials:

The crystalline Si-Ca-DTPMP slurry was dispersed in a surfactant solution as the solution was treated with an ultrasonic probe. The SEM microimage (Fig. 5.3b) shows that the crystals were rod-shaped solids with average major and minor axes of 2.1± 0.32 μm and 0.4±0.17 μm, which corresponds to an equivalent spherical

diameter of 475 nm, considering a sphere of equivalent surface area. During the sonication process, the SDBS adsorbed onto the surface of the precipitates to modify the surface chemistry, which can be illustrated by the variation of particle zeta potential in each synthesis step (Fig. 5.5). Initially, the zeta potential of the silica nanoparticles was -25 mV (step 0, Fig. 5.5); the addition of HCl to the silica nanoslurry increased the particle zeta potential to about -5 mV by neutralizing the negative charge on the particle surface (step 1, Fig. 5.5); by adding $CaCl_2$ to the silica nanoslurry, the $Ca^{2+}$ ions adsorbed onto the surface of the silica particles, indicated by the further increase of zeta potential to -1 mV (step 2, Fig. 5.5); the formation of Ca-DTPMP precipitates was accomplished by adding DTPMP solution into the Ca-silica mixture (step 3, Fig. 5.5); the sonication treatment of the particles in the presence of SDBS reduced the zeta potential of the particles to below -50 mV, which was thereafter stable against coagulation (step 5, Fig. 5.5). This observation is similar to the effect of the SDBS on the silica-zinc-DTPMP nanomaterials in a previous study[115], where the anionic SDBS surfactants modified the surface chemistry of the nanomaterial particles by increasing the electrostatic repulsive interactions.

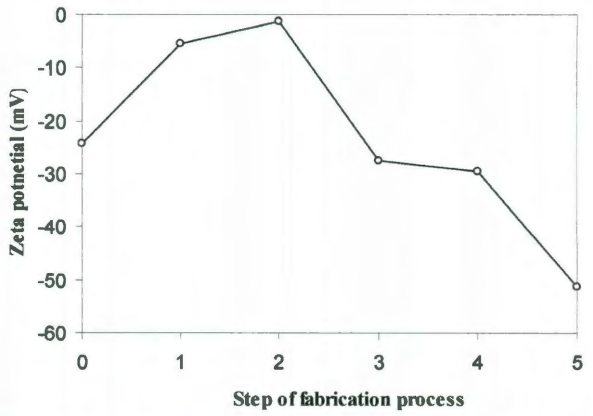


Figure 5.5. Zeta potential variations in each step of nanoslurry synthesis.
Step 0: Prepare the diluted silica nanoslurry; Step 1: Adjust the silica nanoslurry pH to 4.5; Step 2: Add $CaCl_2$ solution to the silica nanoslurry; Step 3: Slowly add DTPMP solution to calcium-silica slurry; Step 4: Diafiltration of the silica based Ca-DTPMP slurry with brine solution; Step 5: Ultrasonic dispersion of the crystalline Si-Ca-DTPMP slurry with a sonication probe in the presence of SDBS surfactant.

The skeletal structure of the nanomaterial solids was investigated by FT-IR. The FT-IR spectrum of the crystalline phase solids (Fig. 5.6) show that the solids have multiply bands around 1000 $cm^{-1}$, which are assigned to phosphonate P–OH vibrations[144]. The presence of P-OH bond indicates of the existence of available coordination sites for phosphoryl oxygen atoms with metal ions, which is in accordance with the aforementioned Ca-DTPMP formula. The strong band at 1070 $cm^{-1}$ is due to the P-O-Ca stretching vibration[115]. The band at 1460 $cm^{-1}$ is attributed to the C-H bending in the $-CH_2-$ groups[97]. The strong broad band at 3400 $cm^{-1}$ corresponds to the adsorbed surface water molecules[102]. The TGA profile (Fig. 5.7) shows that the crystalline phase materials experienced weight loss from 35°C to 1100°C. The weight loss corresponding to the evaporation of adsorbed water was observed over the temperature range 30 to 105°C. The weight loss from 200°C to 700°C is attributed to the loss of lattice water and the

decomposition of organic fraction of the phosphonates[97, 144, 145]. The solid was not stable above 900°C and a loss of $P_2O_5$ was observed. It is difficult to accurately compute the weight loss of each constituent in that the phosphonate decomposition overlapped the dissociation of the lattice water in the solids[144]. Since the melting point of silica is around 1650 °C[146], the silica is not considered to be involved in the thermal decomposition process.

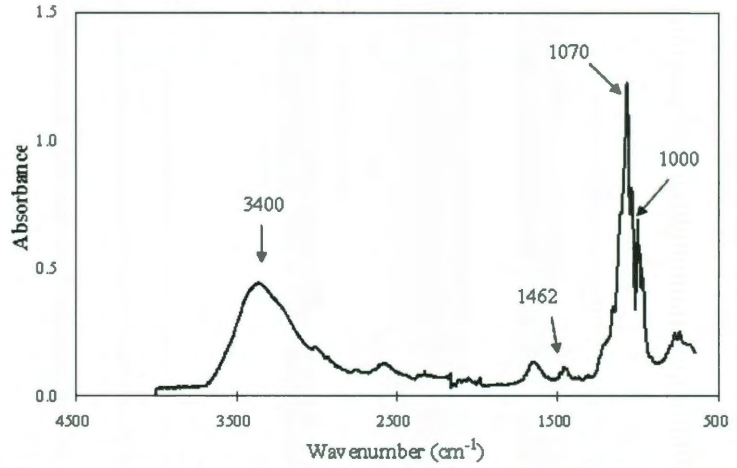


Figure 5.6 FT-IR spectrum of amorphous and crystalline Si-Ca-DTPMP precipitates.

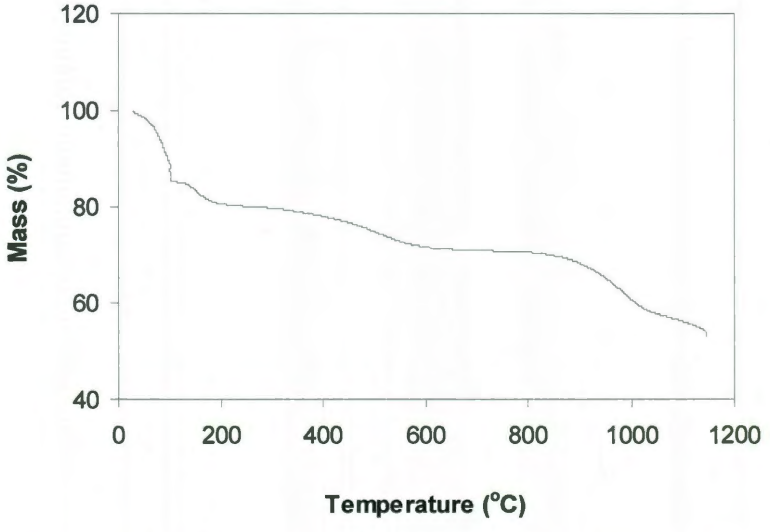


Figure 5.7 TGA profile of the crystalline phase Si-Ca-DTPMP solids.

### 5.3.3 Transport of the nanofluid in porous media:

Packed bed columns are used to investigate the transport of the crystalline Si-Ca-DTPMP nanomaterials in porous media. Calcite (Iceland spar) and Louise sandstone were chosen as column packing materials: calcite is the most reactive component to interact with the phosphonate inhibitors in the formation[4] and it is hypothesized that Si-Ca-DTPMP nanomaterials encounter the greatest resistance in calcite, compared with other types of formation materials; Louise sandstone is an actual core material commonly utilized in oilfield testing as surrogate formation rock to represent the complex and heterogeneous nature of formation materials[143]. Normally, sandstone is a mixture of different types of minerals, including quartz, feldspar, ankerite, clay and kaolinite[106]. EDAX characterization (Fig. 6-SI2) and elemental analysis of the Louise sandstone show that it contains substantial amounts of calcium, iron, manganese, magnesium and aluminum.

The transport of particles through porous media has been studied extensively and several models have been used to quantify such processes[80, 92, 125-127]. The transport process can be viewed either as the flow of nanomaterials in the bulk fluid via advection and diffusion mechanisms or as continuous particle removal by the porous medium collectors via a filtration/attachment process.

**5.3.3.1** ***Advection diffusion/dispersion:*** First, a tracer test (tritiated water) was carried out to measure PV and the hydrodynamic dispersion coefficient (D) of the packed column via the one dimensional advection dispersive equation (1D ADE).

$$R\frac{\partial C}{\partial t} = D\frac{\partial^2 C}{\partial x^2} - v\frac{\partial C}{\partial x} \tag{5.2}$$

where C (mg $L^{-1}$) is the aqueous phase effluent particle concentration at a given time; t (min) is the time; D ($cm^2$ $min^{-1}$) is the hydrodynamic dispersion coefficient; x (cm) represents the distance; R is the retardation factor accounting for the adsorption of the particles to the porous medium; and v (cm $min^{-1}$) is the linear pore velocity, which is calculated based on the flow rate Q (ml $min^{-1}$) at $v=Q/\pi r^2\varepsilon$, where ε represents the porosity of the medium, and r (cm) is the cross sectional radius of the column bed.

According to the breakthrough curves (BTC) of the tracer in each medium (Fig. 5.8a), the D values for each medium were obtained by fitting the ADE to the experimentally acquired breakthrough data using CXTFIT code[103], by setting the retardation factor to one (Table 5.2). The calculated D values in calcite and Louise sandstone are similar to each other (0.0897 vs. 0.0690 $cm^2$ $min^{-1}$) and the values of the dispersivity ($\alpha_{dis} = D/v$) in both media are 200 and 263 μm, on the magnitude of the particle size. The D values obtained in this study are similar to those in the previous transport studies with other types of metal-phosphonate nanomaterials at comparable hydrodynamic conditions[115, 136].

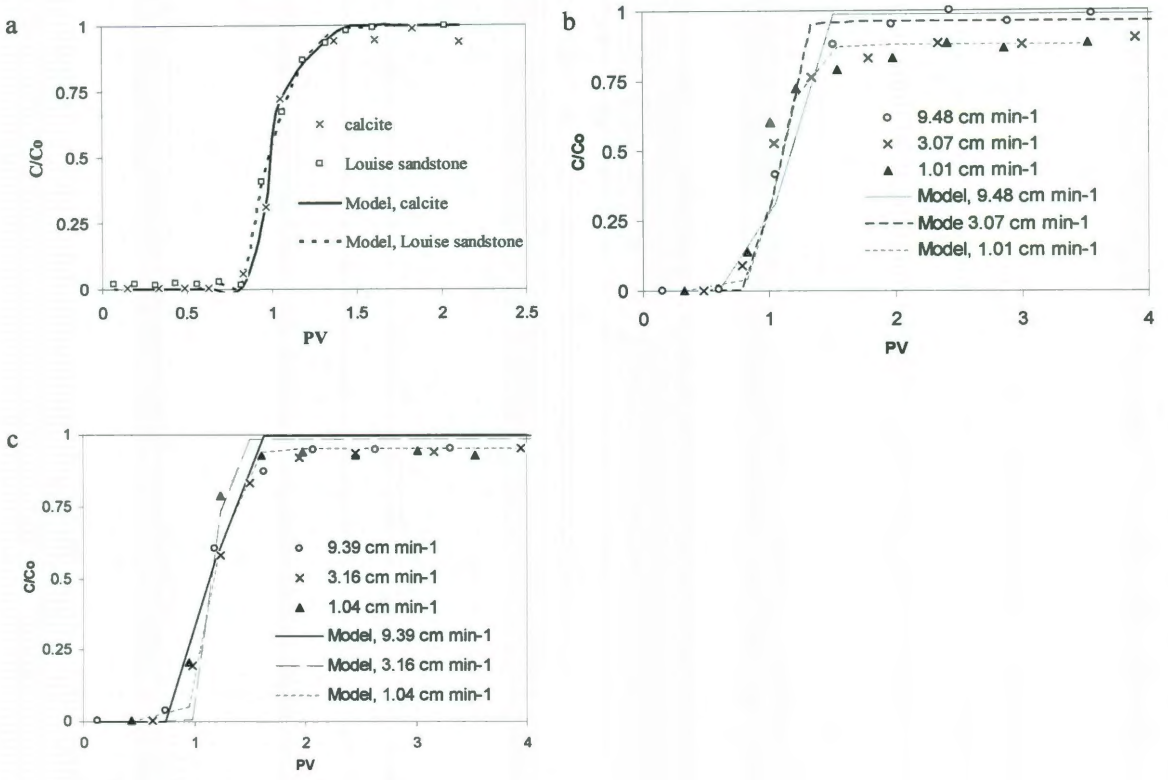


Figure 5.8. Breakthrough curves of (a) tracer (tritiated water) in calcite and Louise sandstone porous media; (b) Si-Ca-DTPMP nanomaterials in calcite at three different pore velocities; (c) Si-Ca-DTPMP nanomaterials in Louise sandstone at three different pore velocities.

The BTC of the Si-Ca-DTPMP nanomaterials in the porous media was generated by plotting the change in the normalized effluent concentrations as a function of the number of PV (Fig. 5.8b and Fig. 5-SI3). Due to the low solubility of the crystalline Ca-DTPMP solids, the dissolved phosphonate concentration accounted for less than 2% of the total phosphonate concentration in the nanofluid. At various flow velocities, the BTC of the Si-Ca-DTPMP nanomaterials through two types of core materials reached a plateau with different breakthrough levels ($C/C_o$) at almost 3 PV (Fig. 5.8). It is proposed that as particles flow through a porous medium, they are removed from solution to the medium surfaces at a constant

rate[80, 84]. At steady saturated flow conditions (where $\partial C/\partial t = 0$), the transport of particles through a porous medium can be described by the following ADE with an additional term ($J_d$) to account for first-order deposition[80, 84] :

$$R\frac{\partial C}{\partial t} = D\frac{\partial^2 C}{\partial x^2} - v\frac{\partial C}{\partial x} - J_d C \tag{5.3}$$

where $J_d$ ($min^{-1}$) denotes the first order deposition rate coefficient of the nanomaterials to the medium surfaces. The solution of Eq. 5.3 follows the effort of Parker and van Genuchten[103], where both the first-order removal of the particles from the aqueous phase and the zero-order production from the solid phase were considered. The solution for a clean bed filtration model can be obtained simply by forcing the zero-order production coefficient to be zero in the analytical solution (Eq. 5.4):

$$C(x,t) = \frac{1}{2}\exp\{\frac{(v-w)x}{2D}\}\mathrm{erfc}\{\frac{Rx-wt}{2(DRt)^{0.5}}\} + \frac{1}{2}\exp\{\frac{(v+w)x}{D}\}\mathrm{erfc}\{\frac{Rx+wt}{2(DRt)^{0.5}}\} \tag{5.4}$$

and $w = (v^2 + 4J_d D)^{0.5}$

The retardation factor R in Eq. 5.3 and 5.4 accounts for the retardation effect arising from the reversible sorption of nanomaterials to the porous medium. Since the R value is characteristic of the sorptive behavior of the nanomaterials to the medium surfaces, it should be independent of the pore flow velocity.

Table 5.2. Properties of the porous media and the parameters of the tracer tests

| Porous medium | Particle size (μm) | Particle density, $\rho_p$ (g cm$^{-3}$) | Bulk density, $\rho_b$ (g cm$^{-3}$) | Porosity, ε | Pore Velocity, v (cm min$^{-1}$) | dispersion coefficient, D (cm$^2$ min$^{-1}$) | $r^2$ |
|---|---|---|---|---|---|---|---|
| Calcite | 106-180 | 2.71 | 1.39 | 0.449±0.006 | 3.406±0.0499 | 0.0897±0.066 | 0.994 |
| Louise sandstone | 106-180 | 2.52 | 1.48 | 0.453±0.005 | 3.442±0.0434 | 0.0690±0.0762 | 0.999 |

The first-order deposition rate coefficient ($J_d$) can be elucidated from Derjaguin-Landau-Verwey-Overbeek (DLVO) theory. According to DLVO theory, a primary energy barrier exists between the particles and the surfaces, which inhibits the attachment of the particles to the surface. The deposition rate is related to the height of this energy barrier, increasing exponentially with decreasing height of the energy barrier[84, 85]. Since the pore flow velocity has no contribution on the height of the primary energy barrier, the flow velocity should not affect the deposition kinetics (the $J_d$ value). On the basis of the above arguments, both R and $J_d$ values should be independent of pore flow velocity. Therefore, the values of these two parameters in each medium were acquired by minimizing the difference between the calculated effluent concentrations based on Eq. 5.4 and the observed effluent concentrations from five BTC at various flow velocities via the least square method. The calculated R and $J_d$ values in each medium are list in Table 5.3. The standard deviations of the R and $J_d$ values were obtained by using non-linear the Excel code from Billo[147]. The calculation (Table 5.3) shows that the nanomaterials experienced comparable retardation effect in calcite and Louise sandstone media (1.08 vs 1.17), indicative of similar sorptive behavior of the nanomaterials to these two types of formation materials. The obtained R values were closed to one, indicating that sorption contributed only a small portion of the attachment of the nanomaterials to the formation medium surfaces. The obtained R values were closed to one, indicating that sorption contributed only a small portion of the attachment of the nanomaterials to the formation medium surfaces.

The $J_d$ value in calcite (0.0185 $min^{-1}$) was higher than that in Louise sandstone (0.0072 $min^{-1}$), which might be attributed to the higher activity of calcite in interacting with phosphonate inhibitors via surface complexation and the formation of inhibitor salt.

The transport of Si-Ca-DTPMP nanomaterials as well as the conventional scale inhibitors in the formation core materials should be a combination of both axial flow (flow following the streamline) and radial flow (flow along the radius of the perforation) in the formation porous medium. The radial flow velocity is dependent on the radius of perforation and can be reduced significantly with increasing radius[148]. In this study, the high end pore velocity of 9.4 cm $min^{-1}$ (136 m $day^{-1}$) was chosen to represent the velocity close to the wellbore and the low end value of 0.42 cm $min^{-1}$ (6 m $day^{-1}$) for the slow velocity farther into the formation. The pore velocity effect on the transport of nanomaterials is summarized in Table 5.3. In each medium, the breakthrough levels were decreased at the reduced pore velocities. At the same velocity, the Si-Ca-DTPMP nanomaterials reached a higher breakthrough level in sandstone medium than in calcite, revealing that the nanomaterials encountered greater resistance in the calcite medium. This phenomenon can be explained by the relationship between the breakthrough level and the values of v and $J_d$. (Eq. 5.5).

From the filtration theory, the value of $J_d$ at stead state can be calculated via[80, 81]:

$$J_d = -\frac{v}{L}\ln(C_e / C_o) \tag{5.5}$$

where L (cm) is the length of the porous medium bed; $C_e$ (mg $L^{-1}$) is the steady-state effluent concentration of the nanomaterials; and $C_o$ (mg $L^{-1}$) is the influent particle concentration. Hence, the breakthrough level at each pore velocity at the steady state can be calculated based on the $J_d$ values as:

$$\frac{C_e}{C_o} = \exp(-\frac{L \cdot J_d}{v}) \tag{5.6}$$

Eq. 5.6 indicates that in certain media (i.e., a fixed $J_d$ value), the decrease of pore velocity will lead to a lower breakthrough level; at the same pore velocity, the nanomaterials will reach a lower breakthrough level in the medium with a higher $J_d$ value. Therefore, the nanomaterials transport and attachment in formation can be managed by altering the injection velocity. During injection, these materials can be placed farther away from the injection point due to the low attachment to the formation surfaces at higher flow velocities. After the nanomaterials reach the target zone in the formation, the nanomaterials can be affixed to the mineral surfaces via sorption and deposition. The difference between the calculated breakthrough levels and the observed ones (Table 5.3) might arise from the steady state assumption in the calculation, which was not fully attained in the laboratory column experiments, where less than 4 PV of nanoslurry was pumped into the porous medium.

Table 5.3. Modeling fitting results of nanofluid breakthrough experiments from perspective of advection and diffusion

| Porous medium | Q (ml $min^{-1}$) | v (cm $min^{-1}$) | Observed $C/C_o$ | $J_d$ ($min^{-1}$) | R | $r^2$ | Calculated $C/C_o$ |
|---|---|---|---|---|---|---|---|
| Calcite | 1.459 | 9.484 | 0.971 | 0.0185±0.00325 | 1.078±0.0129 | 0.928 | 0.987 |
| | 1.041 | 6.766 | 0.923 | | | | 0.981 |
| | 0.473 | 3.072 | 0.891 | | | | 0.959 |
| | 0.156 | 1.013 | 0.884 | | | | 0.881 |
| | 0.0645 | 0.420 | 0.818 | | | | 0.736 |
| Louise Sandstone | 1.455 | 9.391 | 0.985 | 0.0072±0.00218 | 1.172±0.0105 | 0.949 | 0.995 |
| | 0.976 | 6.300 | 0.976 | | | | 0.992 |
| | 0.490 | 3.165 | 0.964 | | | | 0.984 |
| | 0.162 | 1.047 | 0.935 | | | | 0.952 |
| | 0.0639 | 0.413 | 0.896 | | | | 0.883 |

***5.3.3.2 Colloid filtration:*** In another approach, the nanomaterial transport process can be elucidated by the classical colloid filtration theory (CFT). The rationale of the CFT is to predict the collector removal efficiency based on the physicochemical conditions of the system. The deposition of the nanomaterials to the porous medium surfaces is assumed to take place in two subsequent steps: (1) collision of particles with a surface; (2) attachment of the particles to the surface. Hence, the attachment efficiency ($\alpha$) and the single collector removal efficiency ($\eta_0$) were introduced to quantify the attachment and deposition processes, respectively. The deposition due to Brownian diffusion, interception and sedimentation can be lumped into the $\eta_0$ term[80]:

$$\eta_0 = \eta_D + \eta_I + \eta_G \tag{5.7}$$

where $\eta_D$, $\eta_I$ and $\eta_G$ are the single collector efficiency components as a results of diffusion, interception and sedimentation, respectively. According to Tufenkji and Elimelech[149], these three components can be calculated as a function of several dimensionless groups as follows:

$$\eta_0 = 2.4A_s^{1/3}N_R^{-0.081}N_{pe}^{-0.715}N_{vdW}^{0.052} + 0.55A_sN_R^{1.55}N_{pe}^{-0.125}N_{vdW}^{0.125} + 0.475N_R^{-1.35}N_{pe}^{-1.11}N_{vdW}^{0.053}N_{gr}^{1.11} \tag{5.8}$$

where $N_R$ is the aspect ratio, $N_{Pe}$ is the Peclet number, $N_{gr}$ is the gravitation number and $N_{vdW}$ is the van der Waals number and $A_s$ is the porosity-dependent parameter of Happel's model (see supporting information for details).

The attachment efficiency (α) describes the fraction of collisions of nanomaterials with the porous medium that lead to attachment and is given by

$$\alpha = -\frac{2d_c}{3(1-\varepsilon)L\eta_0} \ln(\frac{C_e}{C_0}) \quad (5.9)$$

where $d_c$ is the diameter of the medium collector particles (150 μm). Based on the calculated $\eta_0$ values at various flow velocities in both media (Table 5.4), Brownian diffusion is the predominate mechanism for the nanomaterials deposition to the porous medium surface and the $\eta_D$ values are considerably larger than the other two terms, especially at high flow velocities (>3 cm $min^{-1}$). Such observations are in agreement with the results of the transport of various types of nanometer or sub-micron scaled particles in different types of porous media, including glass bead, Ottawa sand, soil, etc[150-153]. Furthermore, the gravitational sedimentation was a significant factor for particle removal, due to the high density of the nanomaterials (about 3 g $cm^{-3}$) and $\eta_G$ accounted for 9% and 12% of the total removal efficiency at lower flow velocities of 1 and 0.4 cm $min^{-1}$, respectively. The sedimentation effect in this study was similar to the transport of surface modified iron nanoparticles in glass beads and sand, where the sedimentation appeared to be important at lower velocities[154]. As indicated in Table 5.4, in calcite medium the decline of pore velocities from 6.8 to 0.4 cm $min^{-1}$ leads to 11.4% decrease in the average breakthrough level, which can be accounted for by 6.25 times increase of the $\eta_0$ values and reduction of α ($\times 10^{-2}$)

Table 5.4. Modeling fitting results from perspective of filtration and attachment.

| Porous medium | Q (ml $min^{-1}$) | v (cm $min^{-1}$) | Observed $C/C_o$ | $\eta_D(*10^{-2})$ | $\eta_I(*10^{-4})$ | $\eta_G(*10^{-3})$ | $\eta_0(*10^{-2})$ | $\alpha(*10^{-2})$ |
|---|---|---|---|---|---|---|---|---|
| Calcite | 1.459 | 9.484 | 0.971 | 0.360 | 5.874 | 0.156 | 0.435 | 1.658 |
| | 1.041 | 6.766 | 0.923 | 0.459 | 6.127 | 0.228 | 0.543 | 3.693 |
| | 0.473 | 3.072 | 0.891 | 0.807 | 6.763 | 0.547 | 0.929 | 3.084 |
| | 0.156 | 1.013 | 0.884 | 1.784 | 7.769 | 1.875 | 2.049 | 1.495 |
| | 0.0645 | 0.420 | 0.818 | 3.351 | 8.675 | 4.991 | 3.937 | 1.264 |
| Louise Sandstone | 1.455 | 9.391 | 0.985 | 0.360 | 5.749 | 0.158 | 0.434 | 1.628 |
| | 0.976 | 6.300 | 0.976 | 0.479 | 6.043 | 0.247 | 0.564 | 3.479 |
| | 0.490 | 3.165 | 0.964 | 0.784 | 6.586 | 0.529 | 0.903 | 3.109 |
| | 0.162 | 1.047 | 0.935 | 1.729 | 7.563 | 1.808 | 1.985 | 1.510 |
| | 0.0639 | 0.413 | 0.896 | 3.364 | 8.497 | 5.079 | 3.957 | 1.232 |

values from 3.693 to 1.264. The increase of pore velocity from 6.8 to 9.5 cm $min^{-1}$ results in 5.2% increase in breakthrough level, which is attributed to 20% decrease of $\eta_0$ value and 55% decrease of the $\alpha$ value. It appears that the $\eta_0$ value and the $\alpha$ value share comparable importance in dictating the nanomaterial removal by the formation porous medium.

In Fig. 5.9a is plotted the calculated collector removal efficiencies ($\eta_0$) with respect to the variation of particles sizes in calcite medium at 9.48 cm $min^{-1}$ pore velocity at the experimental conditions of this study. It reveals that with the increase of the particle size from tens of nanometer to micron level, the diffusion component ($\eta_D$) keeps decreasing, while the interception and sedimentation terms ($\eta_I$ and $\eta_{gr}$) increase. Within the particle size range of 1 μm, the Brownian diffusion is the major factor in the deposition of nanomaterials onto the medium surface. Some studies showed that the effect of the medium grain size can be significant for nanomaterials transport[154, 155]. However, the transport of various types of nanomaterials is greatly dependent on the hydrodynamic conditions and solution chemistry of the system and can deviate from each other considerably.

According to the DLVO theory, the forces that determine the attachment efficiency of the particles to collector surfaces (i.e. the value of $\alpha$) include the electric double layer and London-van der Waals forces (the DLVO forces[156, 157]) and non-DLVO forces[80]. The CFT assumes that the particles are irreversibly being

captured in the primary minimum of the interaction energy profile[158] because of the DVLO forces. As one type of the non-DLVO forces, the hydrodynamic drag force is assumed to have a negligible effect on the α value. However, as stated by Torkzaban et al[159], such an assumption can be invalid when particles are weakly affixed to the collectors in the secondary energy minimum, which is also considered to exert a prominent effect on the retention of the particles to the saturated porous medium because the particles retained in the secondary minimum are more sensitive to hydrodynamic drag force due to the weak binding with the collector surfaces. In this study, the α values were affected by the variation of pore velocities in both media from 9.5 to 0.45 cm $min^{-1}$ (Table 5.4), suggesting that deposition in the secondary energy minimum might have a pronounced effect. Some studies demonstrated that, at certain hydrodynamic and solution conditions the majority of the particles can be retained in the secondary energy minimum via weak chemical binding, e.g., the adhesion of *E. coli* bacteria in quartz sand media[160] and the polystyrene colloids in the glass beads[161].

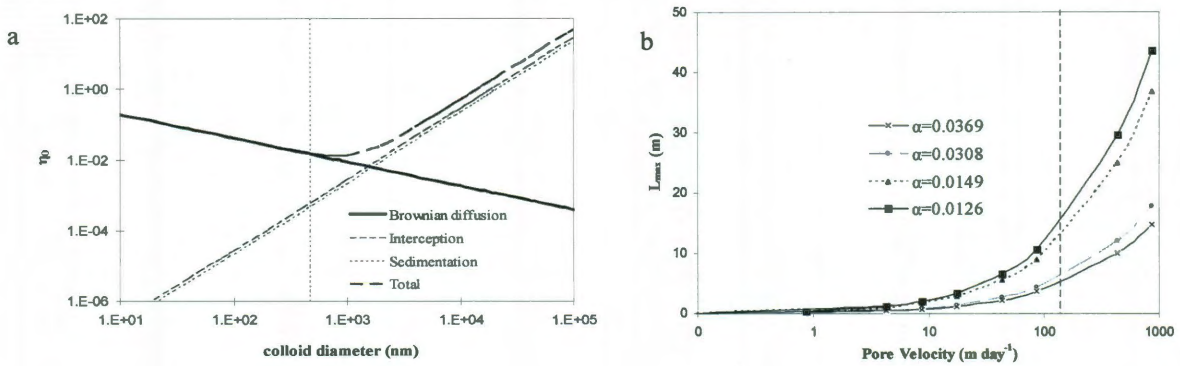


Figure 5.9. (a) the variation of collector removal efficiencies verse the colloid diameter (the dash line corresponds to the diameter of 475 nm); (b) the calculated $L_{max}$ verse pore velocities at various fixed α values (the dash line corresponds to the pore velocity of 136.5 m day$^{-1}$ or 9.48 cm min$^{-1}$).

It is of great importance to investigate the transport distance of the scale inhibitors into the formation porous medium. The farther the inhibitors can be delivered into the formation, the wider area of formation can be protected from scale formation. Based on the CFT model, the maximum transport distance ($L_{max}$) in the porous medium can be defined when 99% of the nanomaterials have been removed by the porous medium (i.e. $C/C_0$=0.01). Therefore, according to Eq. 5.9:

$$L_{max} = -\frac{2d_c}{3(1-\varepsilon)\alpha\eta_0}\ln(0.01) \qquad (5.10)$$

At the experimental conditions in this study, as for a fixed α value, the $L_{max}$ was calculated with respect to the variation of the pore velocities in calcite medium (Fig. 5.9b). Based on the above calculation, the nanomaterials can be delivered into the calcite porous medium with different transport distances, depending on the flow velocity and the attachment efficiency of the particles to the formation matrix. In the conventional squeeze, the acidic inhibitor pill will dissolve the carbonate minerals in the formation, leading to precipitation of calcium-inhibitor

salt and hence limited migration distance of inhibitors into the formation. The surfactant modified Si-Ca-DTPMP nanofluid (pH=6.7) is transportable through calcite porous medium without dissolving the minerals. It can be postulated from Fig. 5.9b that the mobility of the nanofluid in the formation porous medium can be managed by controlling the injection flow velocity. Similar strategy was proposed by He et al.[154] that the surface modified iron nanomaterials can be utilized for in situ dechlorination of organic pollutants in aquifers and the transport distance of iron nanomaterials in groundwater porous media can be manipulated by controlling the flow velocities.

**5.4 Conclusions:**

In the present study, it was found that the prepared crystalline Si-Ca-DTPMP nanofluid was capable of transporting through the porous media and that pore velocity played an important role in determining the particle breakthrough level, while, sorption of the nanomaterials to formation medium surface contributes to a small portion of the nanomaterials attachment to the surfaces. Calculation based on the CFT model indicates that the removal of the nanomaterials by the formation porous medium is probably diffusion controlled and that the migration distance of the nanomaterials is affected by pore velocities and attachment efficiency in the porous medium. It can be proposed that the attachment and migration of the obtained nanomaterials in the formation medium can be managed by altering the nanofluid injection strategy for potential field applications.

# Chapter 5 Supplementary information

## SI5.1 EDAX analysis of the crystalline phase Si-Ca-DTPMP nanomaterials:

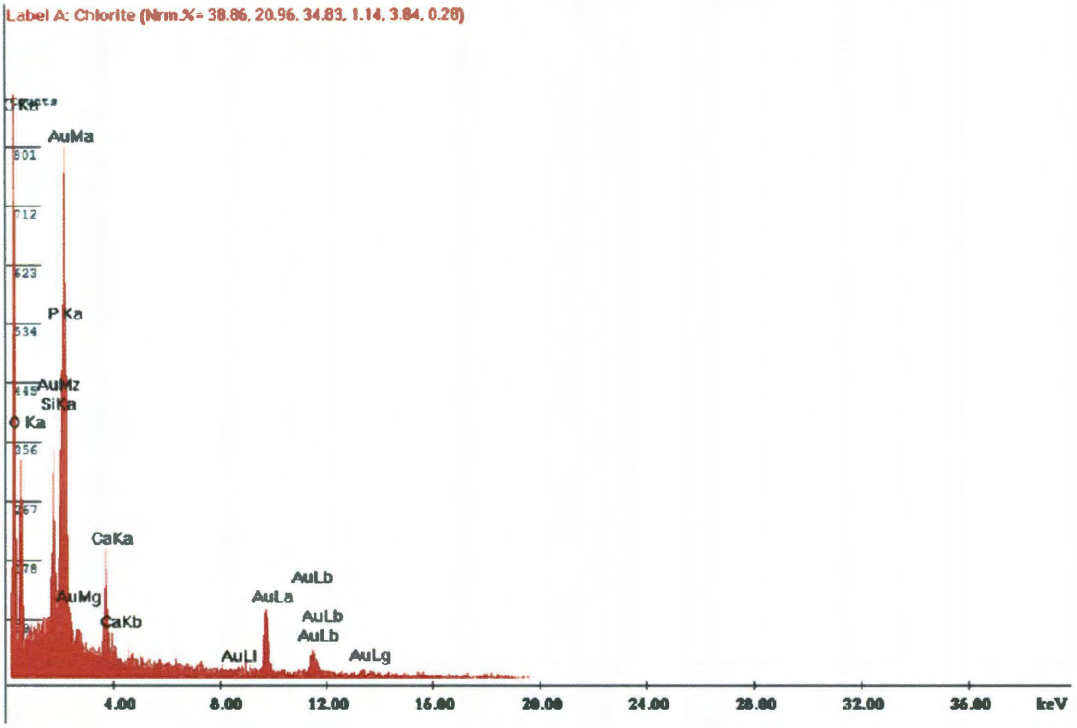


| Element | Wt % | At % | K-Ratio | Z | A | F |
|---|---|---|---|---|---|---|
| C K | 61.32 | 76.40 | 0.2298 | 1.0271 | 0.3647 | 1.0002 |
| O K | 21.50 | 20.11 | 0.0302 | 1.0127 | 0.1385 | 1.0000 |
| SiK | 1.81 | 0.97 | 0.0126 | 0.9774 | 0.7090 | 1.0020 |
| P K | 2.27 | 1.10 | 0.0171 | 0.9460 | 0.7949 | 1.0005 |
| CaK | 1.46 | 0.55 | 0.0124 | 0.9495 | 0.8918 | 1.0000 |
| AuL | 11.64 | 0.88 | 0.0898 | 0.7080 | 1.0906 | 1.0000 |
| Total | 100.00 | 100.00 | | | | |

Figure 5-SI1. EDAX analysis of the crystalline phase Si-Ca-DTPMP nanomaterials.

## SI 5.2 EDAX analysis of Louise sandstone materials:

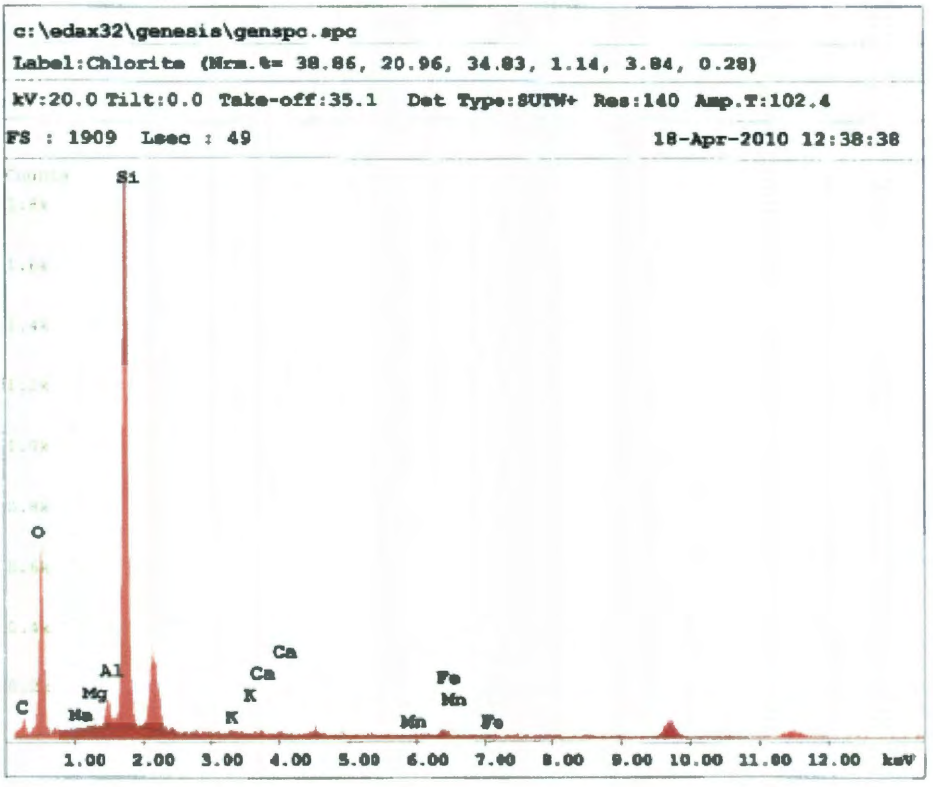


EDAX ZAF Quantification (Standardless)
Element Normalized
SEC Table : Default

| Element | Wt % | At % | K-Ratio | Z | A | F |
|---|---|---|---|---|---|---|
| C K | 15.95 | 24.92 | 0.0223 | 1.0363 | 0.1349 | 1.0004 |
| O K | 39.17 | 45.95 | 0.1062 | 1.0189 | 0.2659 | 1.0005 |
| NaK | 0.12 | 0.10 | 0.0005 | 0.9537 | 0.4218 | 1.0049 |
| MgK | 0.37 | 0.29 | 0.0022 | 0.9777 | 0.5827 | 1.0101 |
| AlK | 1.80 | 1.25 | 0.0126 | 0.9490 | 0.7243 | 1.0186 |
| SiK | 39.29 | 26.25 | 0.3131 | 0.9767 | 0.8158 | 1.0002 |
| K K | 0.44 | 0.21 | 0.0036 | 0.9255 | 0.8884 | 1.0015 |
| CaK | 0.49 | 0.23 | 0.0043 | 0.9475 | 0.9238 | 1.0013 |
| MnK | 0.49 | 0.17 | 0.0041 | 0.8452 | 0.9982 | 1.0000 |
| FeK | 1.89 | 0.64 | 0.0163 | 0.8601 | 1.0025 | 1.0000 |
| Total | 100.00 | 100.00 | | | | |

Figure 5-SI2. EDAX analysis of Louise sandstone materials.

## SI 5.3 Classical colloidal filtration theory (CFT):

The deposition due to Brownian diffusion, interception and sedimentation can be lumped into the $\eta_0$ value:

$$\eta_0 = \eta_D + \eta_I + \eta_G$$

where $\eta_D$, $\eta_I$ and $\eta_G$ are the single collector efficiency components as a results of diffusion, interception and sedimentation, respectively. Following the strategy of Tufenkji and Elimelech[149], these three components can be calculated as a function of several dimensionless groups as follows:

$$\eta_D = 2.4A_s^{1/3}N_R^{-0.081}N_{pe}^{-0.715}N_{vdW}^{-0.052}$$

where $A_s$ is the porosity-dependent parameter of Happel's model, $N_R$ is the aspect ratio, $N_{Pe}$ is the Peclet number, and $N_{vdW}$ is the van der Waals number. $A_s$ is the porosity-dependent parameter of Happel's model and is defined as

$$A_s = \frac{2(1-\gamma^5)}{2-\gamma+3\gamma^5-2\gamma^6}$$

where $\gamma = (1- \varepsilon)^{1/3}$, $\varepsilon$ is the porosity of the porous medium. $N_R$ is the ratio of particle diameter ($d_p$) to spherical collector diameter ($d_c$) (i.e. $N_R = \frac{d_p}{d_c}$ and $d_p$=475 nm, $d_c$=150 μm).

$$N_{Pe} = \frac{vd_c}{D_\infty}$$

where v (m $s^{-1}$) is the pore velocity, $D_\infty$ ($m^2$ $s^{-1}$) is the diffusion coefficient in an infinite medium, which, according to Stocks-Einstein relation, is defined as

$$D_\infty = \frac{kT}{3\pi\mu d_p}$$

where k is the Boltzmann constant ($1.38 \times 10^{-23}$ J $K^{-1}$); T (K) is the absolute temperature; μ (kg $m^{-1}$ $s^{-1}$) is the absolute viscosity of the fluid (water). The van der Waals number $N_{vdW}$ is defined as

$$N_{vdW} = \frac{A}{kT}$$

where A is the Hamaker constant (assumed to be $10^{-20}$ J). Moreover,

$$\eta_I = 0.55A_sN_R^{1.55}N_{pe}^{-0.125}N_{vdW}^{0.125}$$

$$\eta_G = 0.475N_R^{-1.35}N_{pe}^{-1.11}N_{vdW}^{0.053}N_{gr}^{1.11}$$

where $N_{gr}$ is the gravitational force number, defined as

$$N_{gr} = \frac{d_p^4(\rho_p-\rho_f)g}{3kT}$$

where $\rho_p$ is the density of the nanoparticles; $\rho_f$ is the density of fluid and g is the gravitational acceleration, 9.81 m $s^{-2}$.

## SI 5.4 Breakthrough curves in two types of media at 6 cm $min^{-1}$ and 0.4 cm $min^{-1}$, based on ADE model (Eq. 5.4)

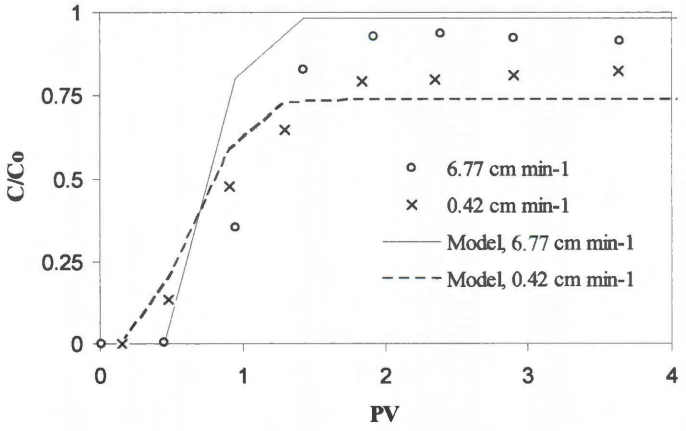


Figure 5-SI3a Breakthrough curves of the Si-Ca-DTPMP nanomaterials in calcite medium;

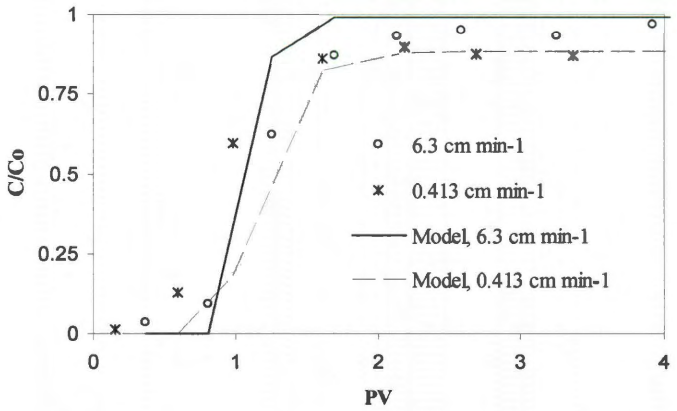


Figure 5-SI3b Breakthrough curves of the Si-Ca-DTPMP nanomaterials in Louise sandstone medium.

# CHAPTER SIX
# CRYSTALLINE CALCIUM-DTPMP NANOMATERIALS: ENHANCED TRANSPORT AND LONG TERM FLOW BACK[§]

**Abstract:**

In this study, crystalline phase calcium-phosphonate nanomaterials were obtained from an amorphous silica templated calcium-phosphonate precipitates, which were further developed into crystalline phases. The transport of the crystalline nanomaterial suspension was investigated in calcite and sandstone porous media using laboratory column breakthrough experiments. The nanomaterials were transportable through these porous media and the transport data can be interpreted using an advection-dispersion equation and classical colloidal filtration theory. By preflushing the formation porous media prior to nanomaterial suspension injection, the suspension experienced enhanced migration. A possible explanation can be derived from viewpoint of interaction energy of the nanomaterials with the medium particles calculated by using Derjaguin-Landau-Verwey-Overbeek (DLVO) theory. The long term flow back performance of the crystalline nanomaterials was evaluated in the laboratory squeeze simulation tests where the crystalline materials were first attached to the formation material surfaces and then gradually returned phosphonates into the brine solution during flow back. Due to the low solubility of the developed crystalline nanomaterials, a long return profile with relatively stable phosphonate return concentrations can be observed in

[§] The content of this chapter has been prepared to be submitted to *Ind. Eng. Chem. Res.*. It was reproduced here as prepared and the only changes here are the numbering of tables and figures, which have been renumbered to adhere to the format of this thesis.

both calcite and sandstone media, indicating of the potential advantage of applying these crystalline nanomaterials for the field operation.

**6.1 Introduction:**

As easily accessible hydrocarbons become less available, developments in offshore deepwater become more important for hydrocarbon production[113]. In the offshore deepwater production, scale formation is a serious flow assurance challenge with significant production reduction and high cost. The principle scale formation mechanisms in offshore production include: 1) the change in pressure and temperature; 2) the mixing of incompatible fluids and 3) the increase of salt concentration[8, 45, 114]. Phosphonates are widely used scale inhibitors in the oilfield to prevent scale formation. Conventionally, phosphonate inhibitors are applied in production wells via a squeeze treatment[1, 2]. In a squeeze treatment, an inhibitor pill solution is injected into a production formation, followed by a brine or diesel overflush to push the inhibitors farther away from the wellbore. The inhibitors attach to the formation rock surfaces by either sorption or precipitation. During production following a squeeze, the injected inhibitors will be gradually desorbed into the formation brine and flow back at certain concentrations. In many laboratory investigations and field observations[8, 9, 17, 19, 143], the inhibitor flow back concentrations quickly reach a peak value and decline to a low plateau level for a period of time. An adsorption squeeze is often carried out by injecting a neutralized pill into a sandstone formation. A precipitation squeeze is performed by pushing an acidic pill into a carbonate formation to form metal (mainly $Ca^{2+}$)-

phosphonate precipitates[9, 17]. Generally, the squeeze treatment has proven to be successful in terms of long protection time. However, it is observed that[9] the acidic pills are mostly precipitated near the wellbore, leading to a limited protection area; the neutralized pills migrate deeper into the formation, but only a small portion of the inhibitors can be retained by the formation medium, a large fraction being eluted out of the reservoir during the initial return. Some recent advances in oilfield scale control technologies include the utilization of viscosified fluids and non-aqueous inhibitor solutions[54]. Viscosified fluids were investigated to place scale inhibitors into formation via bullheaded application[107, 108]. Non-aqueous scale inhibitor solutions were developed in order to avoid possible damages induced by the aqueous squeeze treatment[109-112]. It is desirable to design the squeeze treatment in such a manner that maximum squeeze life can be achieved by forming a low soluble phase in the formation[8] and that the transport distance of the phosphonate inhibitors into the formation can be managed and controlled. Finally, it would be optimal for essentially all of the injected inhibitors to flow back at the same controllable concentration.

In our previous studies[22, 115, 136, 162], a suspension containing scale inhibitor nanomaterials was prepared to extend their use in the delivery of phosphonate inhibitors into the downhole formation. The nanomaterial suspension (nanofluid) was transportable through calcite and sandstone porous media at typical formation flow velocities. The flow back performance of the fabricated nanomaterials was

evaluated via a laboratory squeeze simulation test where the nanomaterials gradually released the phosphonates into the brine by a dissolution mechanism. Recently[162], a crystalline phase scale inhibitor nanofluid has been prepared by developing the amorphous phase Ca-phosphonate solids through a diafiltration treatment[58]. The transport experiments were conducted in a series of column flow-through experiments to investigate the migration behavior of the crystalline phase nanofluid in different types of formation media.

It has been observed that the surfactant preflush could affect the inhibitor return concentrations and a scale inhibitor squeeze modeling study was carried out to simulate the surfactant preflush effect by considering the process reversibility, volumes of surfactant injected, and the adsorption of the surfactant to the rock surface[123]. In the preceding study, an enhanced transport performance of the aforementioned crystalline nanofluid in the calcite and sandstone porous media via a surfactant preflush treatment is reported. DLVO theory was utilized to calculate the interaction energy between the nanomaterials and the formation material particles to elucidate the enhanced transport phenomenon. Furthermore, the advantage of the crystalline nanomaterials over the inhibitor pill solution as well as the amorphous nanomaterials was demonstrated in the long term flow back performance of the crystalline solids in a series of laboratory squeeze simulation tests where phosphonates were returned at relatively stable concentrations for thousands of pore volumes, leading to a greatly extended squeeze lifetime.

## 6.2 Materials and methods:

**6.2.1 Chemicals** Commercial grade diethylenetriamine pentakis (methylenephosphonic acid) (DTPMP) with 50% activity was used as the scale inhibitor. Silica nanofluid (30% wt/wt) of 22 nm diameter and 135 $m^2 g^{-1}$ surface area was purchased from Nyacol Inc. (Ashland, MA). Chemicals such as calcium chloride, sodium chloride, nitric acid, sodium hydroxide, piperazine-1,4-bis (2-ethanesulfonic acid) sodium salt (PIPES) and sodium dodecylbenzene sulfonate (SDBS) were reagent grade and purchased from Fisher Scientific. Tritiated water was purchased from Sigma-Aldrich (Amersham Co. Arlington Height, IL). Deionized water (DI water) was prepared by reverse osmosis followed by a four stage ion exchange water purification process, consisting of a high capacity cation/anion column, two ultra pure ion exchange columns and an organics removal column (Barnstead Internationals, Dubuque, IA).

**6.2.2 Silica-calcium-DTPMP nanofluid synthesis** The preparation procedure of silica-calcium-DTPMP nanofluid was reported in a previous study[162]. Basically, a Ca-$SiO_2$ suspension was prepared by adding $CaCl_2$ solution to a $SiO_2$ nanofluid at 4.5 pH. Then, a basic DTPMP solution was added dropwise to the Ca-$SiO_2$ mixture under vigorously stirring at 70°C. The resultant silica-Ca-DTPMP slurry was diafiltered with a brine solution containing 0.8 M sodium chloride, 0.08 M sodium acetate and 0.1 M calcium chloride at 5.5 pH in order to develop the solid into a crystalline phase. The crystalline nanofluid was acquired by dispersing the

resulting crystalline solids by a probe sonicator (Sonics & Materials Inc, Newtown, CT) in a SDBS solution. The nanofluid was equilibrated by rotation in a tumbler for several days. Before characterization or transport studies, the crystalline silica-calcium-DTPMP (Si-Ca-DTPMP) nanofluid was sonicated for 15 minutes. A portion of the nanofluid was centrifuged at 8500 rpm for 15 minutes to separate the Si-Ca-DTPMP nanomaterial solids. The solid was dried in an oven at 100°C overnight to remove the interstitial water and then characterized by electron microscopy.

**6.2.3 Characterization of the Si-Ca-DTPMP nanomaterials** The scanning electron microscopy (SEM) micrographs of the solid samples were collected on FEI Quanta 400 ESEM FEG at 20 KeV for particle morphology and particle size measurement. The electrokinetic characterization of the nanofluid and the formation porous medium particles followed the method outlined by Tufenkji et al[163]. Eletrophoretic mobility of the nanofluid was measured at 70°C in KCl solution using a Zeta-PALS instrument (Brookhaven Instruments Corporation, Holtsville, NY). Zeta-potential was obtained by fitting the eletrophoretic mobility via the Smoluchowski equation[142]. In order to obtain the zeta potential of the porous medium, the medium materials were first sonicated in a KCl solution by a probe sonicator (Sonics & Materials Inc., Newtown, CT) at 100 Watt for 30 minutes. After the ultrasonic treatment, the supernatant was diluted in KCl solution and the electrokinetic mobility and zeta potential were determined similar

to that of the nanofluid. The effect of the presence of SDBS on particle zeta potential was evaluated by diluting the nanofluid or the supernatant of the medium materials suspension in a surfactant containing solution.

**6.2.4 Nanomaterials column breakthrough experiments** The experimental setup and procedure of the column breakthrough experiments were similar to our previous studies[22, 162]. Calcite (Iceland spar, Creel Chihuahua, Mexico) and Louise sandstone were utilized as the porous medium materials. Louise sandstone was collected as Louise Well, Frio formation located in Galvelston County, TX (9107-9110 ft). The composition of the Frio sandstone included less than 1% calcite, several percentage of clay and over 90% of quartz[143]. A non reactive tracer (tritiated water, $^3H_2O$) test was carried out to measure the dispersion coefficient of the packed column. Following the tracer tests, Si-Ca-DTPMP nanofluid transport experiments were conducted by pumping several pore volumes (PV) of the inhibitor nanofluid through the porous medium. The effect of SDBS preflush on the transport of nanomaterials through the porous medium was investigated by flushing the porous medium by a solution containing 0.75% SDBS and 0.25% KCl prior to the loading of the nanofluid. The phosphonate concentrations in the inhibitor nanofluid for transport experiments were between 0.2-0.3 % (wt/wt).

**6.2.5 Laboratory squeeze simulation test** The laboratory squeeze simulation tests of nanofluid in formation porous materials were conducted similar to the

procedure of the previous studies using totally contained squeeze simulation aparatus[9, 22, 115, 143]. Briefly, a column (7cm length, 0.66 cm ID) packed with Louise sandstone materials (approximately 3.8 g) was pre-saturated by a solution composed of 1M NaCl and 0.01 M $NaHCO_3$. Subsequently, half of a PV of the prepared Si-Ca-DTPMP nanofluids was injected into the column, followed by 0.5 PV overflush with 1M NaCl. After 24 hr shut-in period in which nanomaterials retained in the column attached to the surfaces of the minerals, the column was eluted with a synthetic brine solution (0.025M $CaCl_2$, 0.015 M $NaHCO_3$ and 1M NaCl, sparged with 100% $CO_2$) from the opposite direction, under 75 psi pressure. The prepared synthetic brine was in equilibrium with respect to calcite to simulate the flow back of connate fluids in the field following a squeeze treatment. The column experiments were conducted at 70°C with interstitial flow velocity of 45 m/day. The effluent solution was collected and analyzed for phosphonate concentrations to establish the flow back return curves. A similar squeeze simulation test was carried out in an Iceland spar medium as comparison.

**6.2.6 Analytical methods** Calcium, silica and phosphonate concentrations were analyzed by inductively coupled plasma-optical emission spectrometer (ICP-OES) (Optima 4300 Dv, Perkin Elmer). The wavelengths for calcium, silica and phosphorus measurements are 317.933, 251.611 and 213.617 nm, respectively. A solution containing 5 mg $L^{-1}$ yttrium (371.029 nm) was utilized as internal standard solution. Each sample measurement was repeated for five times and the

mean value of these measurements was reported. The standard deviation for every sample measurement was less than 0.5 %.

## 6.3 Results and discussions:

### 6.3.1 Nanomaterials and porous medium characterization:

In this study, KCl salt was employed as the background electrolyte in the course of transport studies to prevent clay swelling by maintaining the ion exchange selectivity and the mineral permeability[44]. The effect of electrolyte concentration on zeta potential and particle size of the synthesized Si-Ca-DTPMP nanomaterials was investigated at 70°C and 6.7 pH in the presence of 21.5 mM SDBS (Table 6.1). The Si-Ca-DTPMP particles were negatively charged and the salt concentrations appeared to have a negligible effect on either zeta potential or the particle size. Moreover, the SEM micrographs (Fig. 6.1) of the Si-Ca-DTPMP particles confirmed that the morphology and the particle size were not significantly altered by varying the KCl concentration, which is probably due to the presence of a surface coating of SDBS.

Table 6.1a The KCl concentration effect on zeta potential and particle size of the Si-Ca-DTPMP nanomaterials

| Added KCl concentration | Zeta potential (mV) | Particle size (nm) |
|---|---|---|
| 13.5 mM KCl | -61.46±6.97 | 480±150 |
| 33 mM KCl | -51.27±15.65 | 524±111 |

Table 6.1b The presence of KCl and SDBS effect on the zeta potential of the porous media

| Added KCl concentration | Calcite medium | | Sandstone medium | |
|---|---|---|---|---|
| | No SDBS | With SDBS | No SDBS | With SDBS |
| 13.5 mM KCl | -9.78±2.18 | -25.96±3.84 | -38.97±5.08 | -55.38±4.79 |
| 33 mM KCl | -8.58±0.75 | -27.47±1.38 | -35.45±4.89 | -65.31±5.45 |

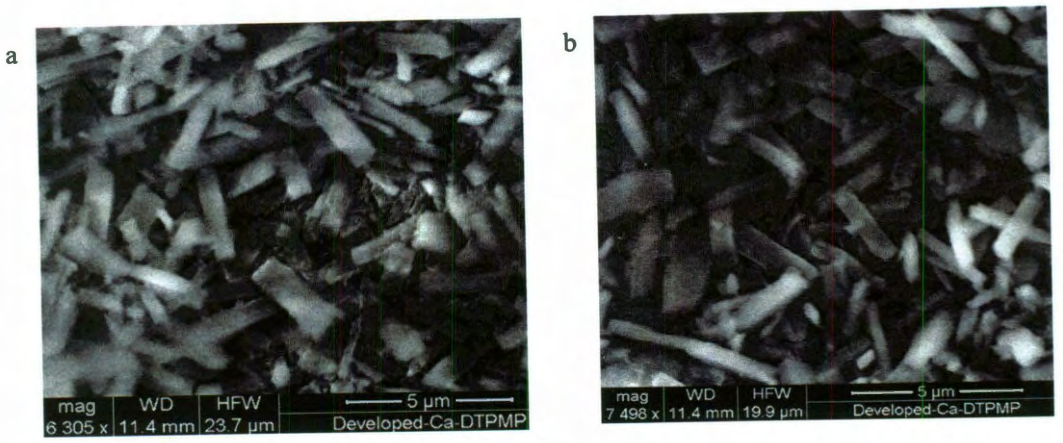


Figure 6.1 SEM micrographs of the Si-Ca-DTPMP nanomaterials at KCl concentration of (a) 13.5 mM and (b) 33 mM. The graph (b) was from the previous study[162].

The zeta potential of the formation porous materials was investigated at 70°C and 6.7 pH in the presence and absence of 7mM SDBS surfactants. Table 6.1b summarizes the effect of addition of SDBS and KCl on the zeta potential of the medium materials. In general, within the range of KCl concentrations considered, KCl did not play a notable role in determining the zeta potential of either calcite or sandstone materials. It was observed that, compared with divalent cations, the monovalent cations have a less pronounced effect on zeta potential of the dolomitic solids[164] and sepiolite[165] in that they adsorbed to these mineral surfaces via simple electrostatic attraction forces and accumulated as counterions in the electrical double layer, instead of adsorbing specifically onto the surfaces, potentially causing a charge reversal. On the other hand, the addition of anionic SDBS surfactant exhibited a more significant effect. The presence of SDBS in calcite and sandstone showed a similar trend in that the addition of SDBS resulted in more negative zeta potential values. Such an observation is in agreement with

the experimental results of the anionic surfactant on zeta potential of kaolinite, montmorillonite and quartz powder in the presence of monovalent alkali salt ions[166], which can be explained in terms of ion-exchange: the hydroxyl group on the mineral surfaces exchanged the anionic part of the surfactant, leading to the formation of additional hydrogen bonds between the minerals and the surfactants[166]. Another possible explanation is that electrostatic bridges between the anionic part of surfactants and the surface of mineral particles can be created by the presence of cations, leading to more negative zeta potential values[167]. The zeta potential values of both the nanomaterials and the porous media are utilized in the following surface interaction potential calculations.

### 6.3.2 Enhanced transport of nanomaterials through formation porous media:

A series of laboratory column breakthrough tests were conducted to investigate the surfactant preflush effect on the migration of inhibitor nanomaterials in the formation porous media by loading the Si-Ca-DTPMP nanofluid in the absence and presence of SDBS preflush (Fig. 6.2). At the beginning, similar to the previous study[115], the hydrodynamic dispersion coefficients in calcite and Louise sandstone media were acquired by fitting the 1-D advection-dispersion equation (ADE) to the tracer breakthrough data via CXTFIT code[103] (supplementary materials). The transport of Si-Ca-DTPMP nanomaterials through the formation porous medium can be described by the ADE with an additional term representing the first-order removal[78, 79, 128]. A retardation factor (R) was included to account

for the sorption of nanomaterials to the porous medium surfaces. Alternatively, from the perspective of classical colloidal filtration theory (CFT), the removal of colloidal particles by the porous medium can be characterized by the attachment removal efficiency ($\alpha$) and the removal efficiency ($\eta_0$) terms to account for the collision of nanomaterials with the porous medium surface and the attachment of the particles to the surface, respectively (refer to supplementary materials for details). The surfactant preflush effect was evaluated in both calcite and sandstone media at comparable hydrodynamic conditions and summarized in Table 6.2a. In calcite medium, compared with the transport study without a SDBS preflush wherein the breakthrough level was 0.89 at interstitial velocity of 3.07 cm $min^{-1}$, the surfactant preflush enhanced the breakthrough level to 0.97, leading to 4.05 times reduction of the $\alpha$ value. Similarly, in Louise sandstone medium the breakthrough level was enhanced by surfactant preflushing from 0.89 to 0.96 at the interstitial velocity of approximately 0.4 cm $min^{-1}$, resulting in the decrease of $\alpha$ value by a factor of 5.15.

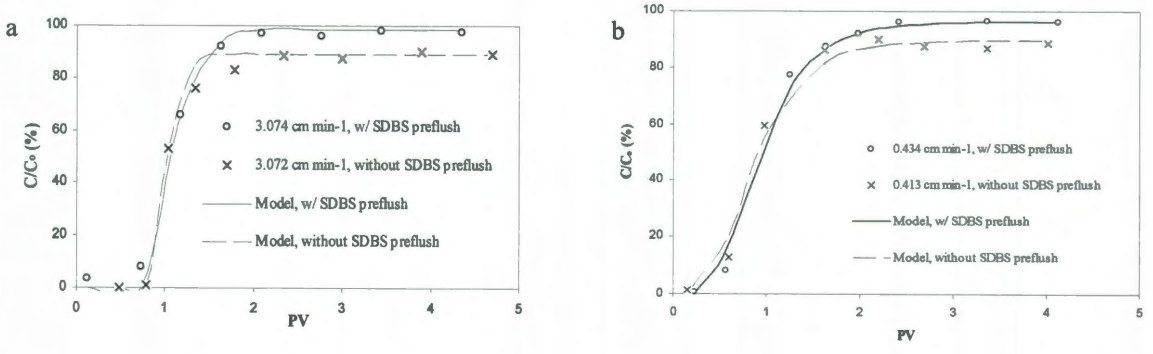


Figure 6.2 Breakthrough curves of nanomaterials in (a) calcite and (b) sandstone media. Solid curves are from CXTFIT model (see text).

Table 6.2 Summery of the nanofluid breakthrough experiments

(a) Parameters obtained from ADE and CFT model calculations

| Porous medium | Condition | Q (ml $min^{-1}$) | v (cm $min^{-1}$) | $C/C_o$ | $J_d$ ($min^{-1}$) | R | $\eta_0(*10^{-2})$ | $\alpha_{exp}(*10^{-2})$ | $\alpha_{theo}$ |
|---|---|---|---|---|---|---|---|---|---|
| Calcite | Preflush | 0.47 | 3.07 | 0.97 | 0.0066 | 1.04±0.025 | 0.93 | 0.76 | 0.79 |
| | No preflush | 0.47 | 3.07 | 0.89 | 0.051 | 1.03±0.029 | 0.93 | 3.08 | 0.78 |
| Louise Sandstone | Preflush | 0.067 | 0.43 | 0.96 | 0.0023 | 1.03±0.032 | 3.96 | 0.24 | 0.68 |
| | No preflush | 0.064 | 0.41 | 0.89 | 0.0064 | 1.05±0.033 | 3.96 | 1.23 | 0.71 |

(b) Potential values obtained from zeta potential measurement

| Porous medium | Condition | v (cm $min^{-1}$) | KCl=13.5 mM | | KCl=33 mM | |
|---|---|---|---|---|---|---|
| | | | $\varphi_{pri}$ | $\varphi_{sec}$ | $\varphi_{pri}$ | $\varphi_{sec}$ |
| Calcite | Preflush | 3.07 | 196.70 | -0.69 | 132.44 | -2.18 |
| | No preflush | 3.07 | 19.43 | -0.29 | 17.01 | -2.29 |
| Louise Sandstone | Preflush | 0.43 | 614.92 | -0.28 | 464.04 | -1.89 |
| | No preflush | 0.41 | 441.83 | -0.19 | 338.34 | -1.74 |

In order to gain insight into the surfactant preflush effect on the nanomaterials transport in porous medium, DLVO theory was utilized to calculate the total interaction energy between the nanomaterials and the porous medium particles in the presence and absence of surfactant preflush[157, 168]. DLVO theory considers the interaction energy between two particles as the sum of two operative factors: the electric double layer (EDL) repulsion energy and London-van de Waals (VDW) attraction energy[44, 142, 169]. The calculation of the EDL repulsion energy ($E_{EDL}$) follows the Hogg et al[170]:

$$E_{EDL} = \pi\varepsilon_0\varepsilon_r a_p\{2\varphi_p\varphi_c \ln[\frac{1+\exp(-\kappa d)}{1-\exp(-\kappa d)}] + (\varphi_p^2 + \varphi_c^2)\ln[1-\exp(-2\kappa d)]\} \qquad (6.1)$$

where $\varepsilon_0$ is the vacuum permittivity ($8.85\times10^{-12}$ F $m^{-1}$); $\varepsilon_r$ is the relative dielectric constant of water at 70°C with value of 65[171]; d (m) is the separation distance of nanomaterials with the porous medium surfaces and $\varphi_p$ (volt) and $\varphi_c$ (volt) are the surface potentials of nanomaterials and the formation porous medium particles, respectively. The surface potential that governs the electrostatic repulsion forces was taken to be equal to the measured zeta potential. $\kappa$ ($m^{-1}$) is the inverse Debye-Huckel length, given by

$$\kappa^{-1} = (\frac{\varepsilon_0\varepsilon_r k_B T}{2000e^2 I_c N_A})^{0.5} \qquad (6.2)$$

where $N_A$ is the Avogadro number ($6.022\times10^{23}$ $mol^{-1}$); $I_c$ (M) is the ionic strength (IS); $k_B$ is Boltzman constant ($1.38\times10^{-23}$ J $K^{-1}$); T (K) is the absolute temperature, e is the electron charge ($1.6\times10^{-19}$ C). On the other hand, the VDW attraction

energy ( $E_{VDW}$ ) was calculated using[172, 173]:

$$E_{VDW} = -\frac{Aa_p}{6d}[1+\frac{14d}{\lambda}]^{-1} \quad (6.3)$$

Where $\lambda$ is the characteristic wavelength of the interaction (assumed to be 100 nm[174]) and A (J) is the Hamaker constant of the nanomaterials-water-porous medium system. Because the necessary optical data regarding Si-Ca-DTPMP nanomaterials is not available, for simplicity, the Hamaker constant for hydroxyapatite was adopted in the calculation. Since Louise sandstone is composed primarily of silica (>90%), the Hamaker constant for nanomaterials-water-silica system is estimated based on the Hamaker constants of hydroxyapatite-water and silica-water systems via[175]:

$$A_{nanomaterials-water-silica} \approx (A_{silica-water-silica})^{0.5} \times (A_{HA-water-HA})^{0.5} \quad (6.4)$$

$A_{HA-water-HA}$ is assumed as $1\times10^{-21}$ J, in view of the simulation results of Cardenas et al[176] and the value of $A_{silica-water-silica}$ was chosen as $8.3 \times 10^{-21}$ J[177]. Hence, $A_{nanomaterials-water-silica}$ was estimated to be $2.9\times10^{-21}$ J. Similarly, in the calcite medium, the $A_{silica-water-silica}$ value was replaced by $A_{calcite-water-calcite}$ value of $2.2\times10^{-20}$ J[175, 178] and $A_{nanomaterials-water-calcite}$ was calculated to be $4.7\times10^{-21}$ J. Hence, the total interaction energy between the nanomaterials and the formation particles can be expressed as:

$$E_I = E_{EDL} + E_{vdW} = \pi\varepsilon_0\varepsilon_r a_p\{2\varphi_p\varphi_c \ln[\frac{1+\exp(-\kappa d)}{1-\exp(-\kappa d)}] + (\varphi_p^2+\varphi_c^2)\ln[1-\exp(-2\kappa d)]\} - \frac{Aa_p}{6d}[1+\frac{14d}{\lambda}]^{-1} \quad (6.5)$$

On the basis of the experimentally acquired zeta potentials values of the core materials and the nanomaterials, $E_I$ was calculated in each medium at different KCl concentrations. In Fig. 6.3 and 6.4 are plotted the nanomaterials-porous medium interaction energy in calcite and Louise sandstone media at 70°C as a function of the separation distance and KCl concentrations. According to DLVO calculation, the increase of ionic strength reduced the height of energy barrier. In calcite medium, sizable repulsive energy barrier existed between the nanomaterials and calcite medium and the presence of anionic surfactant enhanced the energy barrier at both KCl concentration of 13.5 mM and 33 mM, due to the more negative zeta potential of the calcite particles as listed in Table 6.2a. The substantially increased energy barrier in the presence of the SDBS surfactant inhibited the deposition of Si-Ca-DTPMP nanomaterials to the calcite surface, which explained the improved breakthrough level and correspondingly, the reduced attachment efficiency observed in the transport study. Similar phenomenon was observed in the study of the transport of cryptosporidium oocyst to the ultrapure quartz surfaces[179]. It was observed that bacteria, with less negative zeta potential, showed higher deposition kinetics to the surfaces, compared with the bacteria with more negative zeta potential. In this study, the DLVO calculation also predicted that at the condition of 2 M IS, which is commonly encountered in the field, the EDL energy profiles approaches to the surface and VDW attractive forces dominated, leading to particle aggregation and precipitation. As pointed by Hahn et al[180], the increase of ionic strength will ultimately change the deposition

from secondary minima to primary minima and eventually the energy barrier disappears. The scenario of high IS demonstrates one of the challenges of applications of nanomaterials in the oilfield. Similarly, Fig. 6.4 shows that in Louise sandstone medium the enhancement of the energy barrier between the nanomaterials and the sandstone surfaces can be observed in the presence of SDBS preflush. Again, a significant impact on interaction energy at 2 M IS can be observed in sandstone medium.

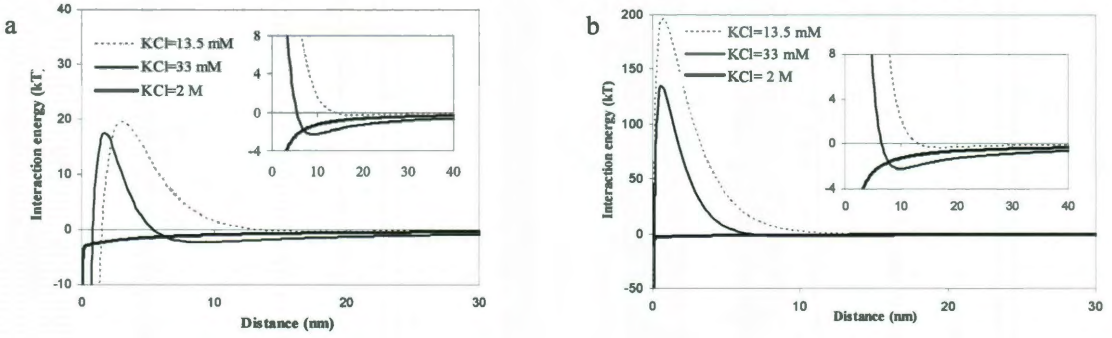


Figure 6.3 Interaction energy between the nanomaterials and calcite particles (a) in the absence of SDBS preflush and (b) in the presence of SDBS preflush. The inset shows the secondary minimum attractive region.

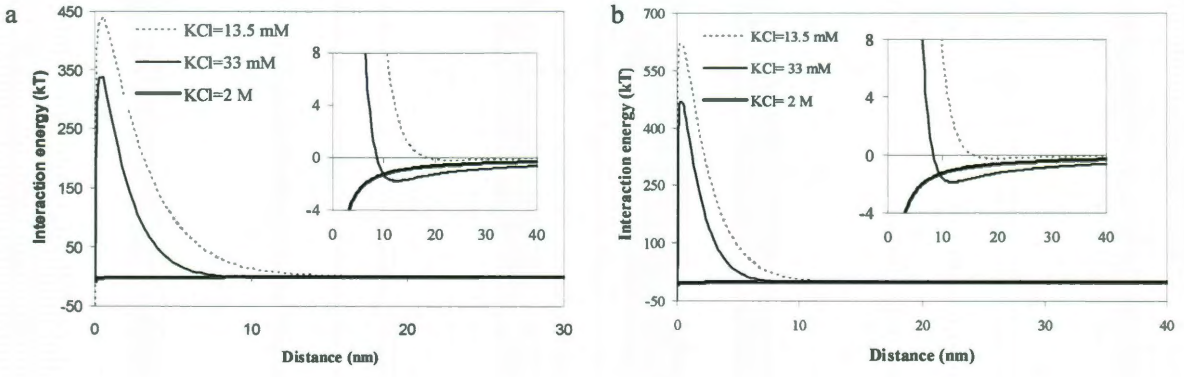


Figure 6.4 Interaction energy between the nanomaterials and Louise sandstone particles (a) in the absence of SDBS preflush and (b) in the presence of SDBS preflush. The inset shows the secondary minimum attractive region.

### 6.3.3 Laboratory inhibitor nanofluid squeeze simulation:

In order to evaluate the flow back performance of the crystalline Si-Ca-DTPMP nanomaterials and to simulate the inhibitor nanomaterials-formation core materials interaction at downhole conditions, several laboratory squeeze simulation tests were conducted by injecting the Si-Ca-DTPMP nanofluid into Louise sandstone and calcite columns via totally contained squeeze protocol[9, 143]. During the 24-hour shut-in period, the nanomaterials were allowed to adhere to the surfaces of the formation core materials via either sorption or surface complexation mechanism. Subsequently, the column was eluted with a synthetic brine in the reverse direction to simulate the field process[8, 9]. An inhibitor return curve is plotted in Fig. 6.5a as the change of the effluent phosphonate concentrations verse the volume of return flow, normalized by the column pore volume.

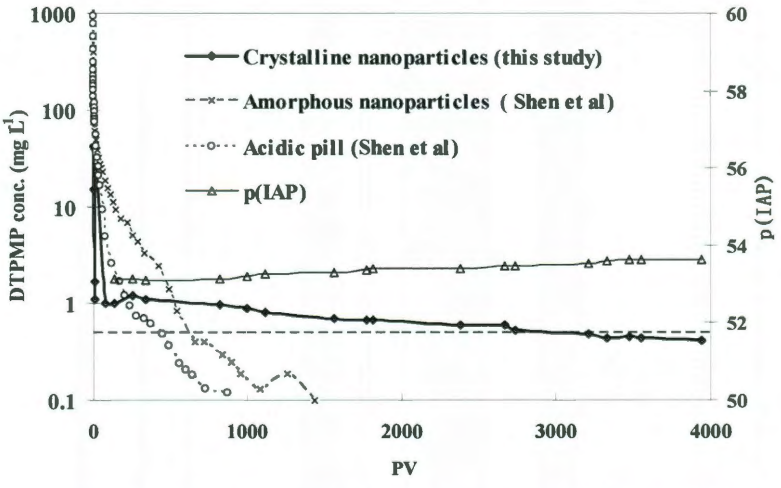


Figure 6.5a The long term flow back performance of the crystalline Si-Ca-DTPMP nanofluid in squeeze simulation tests in Louise sandstone: three returns curves by employing a crystalline nanofluid in this study, an acidic pill solution and an amorphous nanomaterial fluid in the previous study (the dashed line represents 0.5 mg $L^{-1}$ of DTPMP)

Table 6.3 summarizes the physiochemical conditions of squeeze simulation tests of crystalline phase Si-Ca-DTPMP in this study and also one type of amouphous Ca-DTPMP nanomaterials and for comparison one acidic phosphonate pill from a previous study[22], all in Louise sandstone. These three return experiments were conducted by injecting half a PV of inhibitor slurry (or solution) into the porous medium with active DTPMP concentrations of 0.8%. In Fig. 6.5a is plotted the return curves of these three squeeze simulation tests at comparable experimental conditions. The acidic pill solution showed that the DTPMP return concentrations were as high as a thousand milligrams per liter or higher in the initial several pore volumes, followed by a gradual decline to sub mg $L^{-1}$ level within a few hundred PVs. The retention mechanism of phosphonate inhibitors in the calcite-bearing materials is proposed to be the formation of calcium-inhibitor salt when a considerable amount of phosphonates was injected into the formation materials.

Table 6.3 Physiochemical conditions of each squeeze simulation test

| Experiment | Medium | [a]$Ca^{2+}$ (M) | Flow rate (ml/hr) | solution pH | Temperature (°C) | PV (ml) | DTPMP injected (mg) |
|---|---|---|---|---|---|---|---|
| Nanofluid (this study) | sandstone | 0.1 | 90 | 5.5 | 70 | 1 | 4.1 |
| Amorphous nanofluid( Shen et al[22]) | sandstone | 0.1 | 90 | 5.5 | 70 | 8 | 32 |
| Acidic pill(Shen et al[22]) | sandstone | 0.1 | 90 | 5.5 | 70 | 8 | 32 |
| Nanofluid (this study) | calcite | 0.1 | 90 | 5.5 | 70 | 1 | 3.9 |

[a] The concentrations listed here are the $Ca^{2+}$ concentrations in the stock synthetic brine solutions.

Table 6.4 Summary of the experimental results of each squeeze simulation test

| Experiment | Porous media | DTPMP injected (mg) | Total volume returned (PV) | $V_{30}$[a] (PV) | $V_{80}$[a] (PV) | % of inhibitor returned[b] | NSL (bbl/kg)[c] |
|---|---|---|---|---|---|---|---|
| Nanofluid (this study) | sandstone | 4.1 | 3940 | 820 | 2670 | 80 | 5960 |
| Amorphous nanofluid (Shen et al[22]) | sandstone | 32 | 1440 | 14.75 | 200 | 79 | 1210 |
| Acidic pill (Shen et al[22]) | sandstone | 32 | 870 | 2.75 | 47 | 87 | 775 |
| Nanofluid (this study) | calcite | 3.9 | 5915 | 2141 | 4587 | 85 | 9700 |

[a] $V_{30}$ and $V_{80}$ denote the PV of brine returned when 30% and 80% of the total amount of inhibitors flushed out;
[b] indicates the ratio of the amount of inhibitor returned in the squeeze test to the mass of inhibitor injected
[c] NSL was calculated by assuming the MIC of 0.36 mg/L.

Kan et al[9, 143] indicated that these formed calcium-inhibitor salts were initially amorphous (or microcrystalline) phases. Similar to the conventional acidic pill squeeze, the return of the amorphous phase Ca-DTPMP nanomaterials exhibited a similar figure as that of the acid pill. As indicated in Table 6.4, in these two scenarios, 80% of the injected inhibitors flushed out at 47 PV and 200 PV, respectively, leading to a limited squeeze life time. In light of the above arguments, it can be concluded that the return behavior of the amorphous Ca-DTPMP nanomaterials were similar to that of the acidic pill solution in terms of the shape of phosphonate return profiles.

According to Kan et al[143], the inhibitor return data can be fitted to an advection-dispersive type of equation as follows:

$$C_{aq}(M) = C_{aq}^{unreacted}\cdot\left(a.e^{-0.5(\frac{PV-1}{b})^2}\right) + \sum_{i=1}^{3} C_{eq}^{ppt,i}\{1-\frac{1}{2}.erfc[\frac{R_i - PV}{2(D_i\cdot R_i\cdot PV)^{0.5}}]-\frac{1}{2}\cdot e^{(\frac{1}{D_i})}\cdot erfc[\frac{R_i + PV}{2(D_i\cdot R_i\cdot PV)^{0.5}}]\} \quad (6.6)$$

where, $C_{aq}$ (M) is the aqueous phase (effluent) phosphonate concentration; a and b are Gaussian distribution coefficients; $D_i$ is a dimensionless constant representing the corresponding relative spread of the solid phase i; $R_i$ is the retardation factor of dissolution of solid phase i; and PV represents the number of pore volumes. The first term in Eq. 6 denotes the return of the unreacted phosphonate and the second term represents the return after the initial several PV. These parameters are functions of temperature, ionic strength, brine pH, $Ca^{2+}$ concentration and the pill

acidity and concentration. The DTPMP speciation model developed by Tomson et al[59] was utilized to calculate the speciation of phosphonates. The detailed calculation methods are included in the software package of SqueezeSoftPitzer[143]. Two DTPMP return profiles predicted by the software are plotted in Fig. 5b for squeeze simulation tests with an acidic pill (5.7 moles excess $H^+$) and a neutralized pill (6.7 pH) both in sandstone medium. It was found that the simulated return profiles of the acidic and neutralized pills were in a similar shape of the experimentally acidic pill return[22], where phosphonate inhibitors were released in a large quantity in the first 100 PVs, leading to a limited squeeze lifetime. Such a return profile is characteristic of the returns of various types of phosphonates in carbonate-bearing formation materials, as encountered in field observations or in the laboratory investigations at similar physiochemical and fluid dynamic conditions[8, 9, 143].

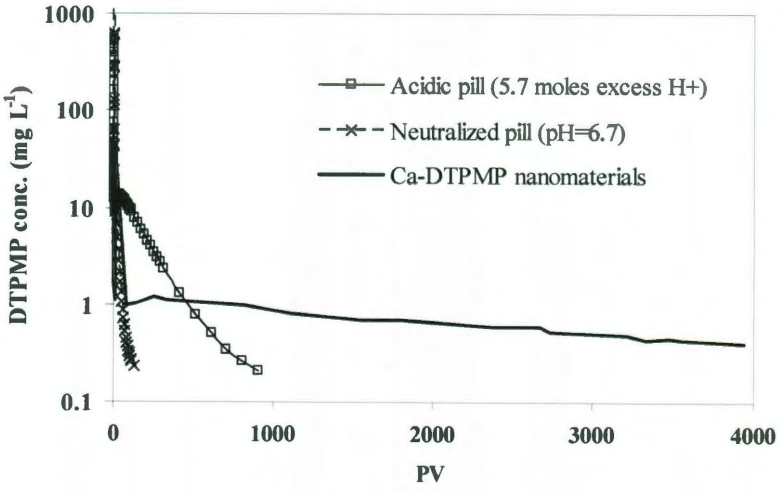


Figure 6.5b The long term flow back performance of the crystalline Si-Ca-DTPMP nanofluid in squeeze simulation tests in Louise sandstone: return curves obtained from SqueezeSoftPitzer software by using an acidic pill and a neutralized pill, respectively.

The flow back performance of the developed crystalline phase Si-Ca-DTPMP nanomaterials in sandstone medium (Fig 6.5) displayed a totally different return profile: the phosphonate concentrations varied from 50 mg $L^{-1}$ for the first several PVs, representing the initial return of the aqueous phosphonates and the inhibitor nanomaterials returned phosphonates at relatively stable concentrations between 0.5 and 1 mg $L^{-1}$ for as long as 4000 PVs until the end of phosphonate return, wherein the majority of injected inhibitors were flushed out of the column. Table 6.4 shows that 30% and 80% of the injected inhibitors returned at 820 PV and 2670 PV, respectively; while as for the case of the acidic pill, these two figures were only 2.75 and 47 PVs. To the best of our knowledge, it is the first time that such long term inhibitor flow back performance with stable return concentrations is reported.

The release of phosphonate inhibitors from metal-phosphonate precipitates in various laboratory and field studies is assumed to be dominated by the dissolution of the attached metal-phosphonate precipitates from the surfaces of the formation core materials into the production brine[58]. With respect to the Ca-DTPMP of interest in this study, considering the stoichiometry of the solid of $Ca_3H_4$DTPMP, the corresponding negative logarithm of ion activity product (pIAP) is of the form[162]:

$$pIAP = -\log_{10}[(Ca^{2+})^3\{H^+\}^4(DTPMP^{10-})] \qquad (6.7)$$

where parentheses refer to molar concentration and braces for activity. The free calcium ion ($Ca^{2+}$) and $DTPMP^{10-}$ species concentrations were obtained from the total aqueous phase phosphonate concentrations through a speciation model, which considers the acid/base and complex solution chemistry as a function of pH, temperature and ionic strength[59]. Kan et al[58] confirmed that this model can be utilized to predict the field phosphonate return concentrations observed from several oil and gas wells with wide ranges of production conditions and they reported the negative logarithm of solubility product ($pK_{sp}$) of crystalline phase Ca-DTPMP precipitate with value of 54.0±0.26, obtained at similar experimental conditions (1 M NaCl, 5.5 pH and 70°C). In Fig. 6.5a is plotted the calculated pIAP as a function of the volumes of brine flushing. During the squeeze simulation, the calculated pIAP values changed insignificantly, indicating that the injected Ca-DTPMP precipitates were maintained as crystalline phase solids till the end of the phosphonate return. The average of the experimentally obtained pIAP values after 4000 PVs was 53.66±0.20, which is comparable to the reported crystalline phase solid $pK_{sp}$ value of 54.0±0.26[58]. This phenomenon revealed that the effluent solution acquired from the squeeze simulation was in equilibrium (saturated) with the crystalline phase Ca-DTPMP solid[44, 181]. Evidently, the long term flow back performance with stable inhibitor return concentrations for the developed crystalline Si-Ca-DTPMP nanomaterials is attributable to the release of the phosphonates from the crystalline phase solid, governed by its low solubility in brine solutions. The development of the nanomaterials into their crystalline

phase regulated the phosphonate return concentrations, leading to an enhanced inhibitor squeeze lifetime.

In another experiment, a similar squeeze simulation test using crystalline nanomaterials was performed with a calcite (Iceland spar) column (Fig. 6.6), since calcite is the primary formation material responsible for phosphonate retention[143]. Similar to the long term return profile in Louise sandstone column, the nanomaterials returned phosphonates at a relatively stable concentration around 0.5 mg $L^{-1}$ for nearly 6000 PV, which is due to the low dissolution of the crystalline phase Ca-DTPMP solid in calcite. The calculated pIAP values were essentially constant with average of 53.59±0.14. Since the inhibitor return concentration by the end of the squeeze simulation in calcite medium was 0.36 mg $L^{-1}$, hence, a minimum inhibitor concentration of 0.36 mg $L^{-1}$ was assumed, which is commonly encountered in the oilfield[58]. It should be noted that all of the DTPMP concentrations reported in the preceding study are "active" concentrations, whereas "as product" this 0.36 mg $L^{-1}$ might be from 0.72 mg $L^{-1}$ to 3.6 mg $L^{-1}$, depending upon fluid conditions and application needs. The effectiveness of 0.36 mg $L^{-1}$ DTPMP scale inhibitor for barite and/or calcite scale control can be evaluated via a simple calculation strategy using Scalesoftpitzer software, developed by Tomson et al[61, 182]. The calculation was carried out by choosing the brine with compositions and field production conditions as list in Table 6-S2 (supplementary materials). It was found that with 0.36 mg $L^{-1}$ DTPMP

presence, at the outlined conditions, calcite scale can be inhibited up to 0.53 SI unit and barite up to 1.23 SI units, where SI standards for saturation index and is defined logarithm of the saturation ratio[45].

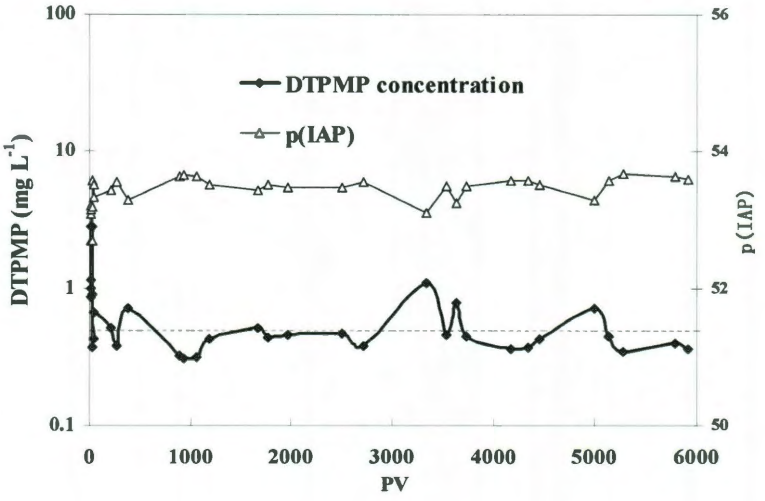


Figure 6.6 The long term flow back performance of the crystalline Si-Ca-DTPMP nanofluid in calcite (Iceland spar) medium (the dashed line represents 0.5 mg $L^{-1}$).

The concept of a "normalized squeeze lifetime", developed by Kan et al[116], can be utilized to better illustrate the potential implication of the prepared nanomaterials. A NSL can be calculated from the ratio of effective return volumes and the mass of inhibitors injected, as defined in the literature[116]:

$$\mathrm{NSL} = \frac{\text{return volume (liter)} \times 10^6 (\text{mg kg}^{-1})}{\text{inhibitor mass (mg)} \times 159 (\text{liter bbl}^{-1})} = \frac{6 \text{ liter} \times 10^6 \text{ mg kg}^{-1}}{3.89 \text{ mg} \times 159 \text{ liter bbl}^{-1}} = 9700 (\text{bbl kg}^{-1}) \quad (6.8)$$

which indicated that in field applications, scale formation control of the produced brine water with volume up to 9700 barrels can be managed by injecting a dose of crystalline phase nanoslurry containing only 1 kg of active DTPMP component. The obtained NSL value in this study is considerably extended over the

conventional squeeze simulation results (summarized in Table 6.4). By assuming a brine production rate of 1000 bbl $day^{-1}$ and a formation pore volume equivalent of 200 bbl for a production well, the well protection time (PT) can be calculated as follows:

$$PT = \frac{\text{number of PV} \times \text{formation PV}}{\text{production rate (bbl day}^{-1})} = \frac{6000\,\text{PV} \times 200\,(\text{bbl/PV})}{1000\,(\text{bbl/day})} = 1200\,\text{days} \approx 3.3\,\text{yrs} \quad (6.9)$$

which indicates that the protection time of one treatment might last as long as 3.3 years for a well with production rate of 1000 bbl $day^{-1}$ in a single squeeze treatment.

**6.4 Conclusions:**

In the present study, the enhanced migration of the crystalline Si-Ca-DTPMP nanomaterials in calcite and Louise sandstone porous medium can be achieved via a surfactant preflush treatment and such phenomenon can be understood by calculating the interaction energy of the nanomaterials and the porous medium particles. The laboratory squeeze simulation tests of such materials show that the developed crystalline solids return phosphonate inhibitors at a relatively constant concentration for thousands of PVs, which is of considerable advantage over the pill solutions. The long term flow back performance of the crystalline nanomaterials can be explained by their fixed low solubility in brine solution. The calculated NSL values of these materials in calcite and sandstone materials were also enhanced, which shows the potential advantage of utilizing these novel

inhibitor nanomaterials for the scale control applications, where the inhibitor return concentration can be controlled by manipulating the morphological structure and solubility property of the applied nanomaterials.

# Chapter 6 Supplementary information

## SI 6.1 Characterization of porous medium via tracer breakthrough test:

A tracer (tritiated water) test was carried out to measure the PV and the hydrodynamic dispersion coefficient (D) of the packed column. According to the breakthrough curves of the tracer in each medium (Fig. 6-SI1), the D values for each medium can be obtained by fitting the one-dimensional advection-dispersion equation (1-D ADE) (Eq. S-1) to the acquired data using CXTFIT code[103], by setting the retardation factor (R) to one:

$$R\frac{\partial C}{\partial t} = D\frac{\partial^2 C}{\partial x^2} - v\frac{\partial C}{\partial x} \qquad \text{(S-1)}$$

where C (mg $L^{-1}$) is the effluent nanomaterials concentration at a certain time; t (min) denotes the time.

Table 6-S1. Properties of the porous media and parameters from the tracer tests

| Porous medium | Particle size (μm) | Particle density $\rho_p$(g cm$^{-3}$) | Bulk density $\rho_b$ (g cm$^{-3}$) | Porosity, ε | Pore Velocity, v (cm min$^{-1}$) | dispersion coefficient, D (cm$^2$ min$^{-1}$) | $r^2$ |
|---|---|---|---|---|---|---|---|
| Calcite | 106-180 | 2.71 | 1.39 | 0.449±0.006 | 3.406±0.0499 | 0.0897±0.066 | 0.994 |
| Louise sandstone | 106-180 | 2.52 | 1.48 | 0.453±0.005 | 3.442±0.0434 | 0.0690±0.0762 | 0.999 |

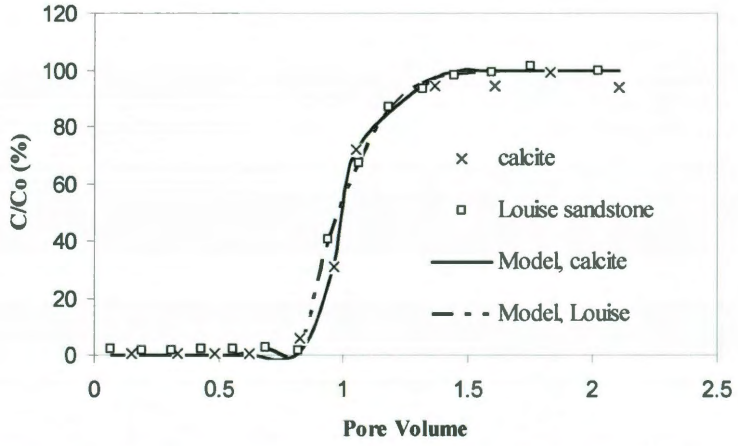


Figure 6-S1 Tracer (tritiated water) breakthrough tests in calcite and Louise sandstone media[162].

**SI 6.2 Describing nanomaterials transport by ADE and filtration theory:**

The transport of Si-Ca-DTPMP nanomaterials through the formation porous medium can be described by the ADE with an additional term representing the first-order removal[78, 79, 128]:

$$R\frac{\partial C}{\partial t} = D\frac{\partial^2 C}{\partial x^2} - v\frac{\partial C}{\partial x} - J_d C \qquad \text{(S-2)}$$

where $J_d$ ($min^{-1}$) is the first-order removal rate coefficient and can be calculated as[80, 81]:

$$J_d = -\frac{v}{L}\ln(C_e / C_o) \qquad \text{(S-3)}$$

where L (cm) is the length of the porous medium; $C_e$ (mg $L^{-1}$) is the steady-state effluent concentration of the nanomaterials; and $C_o$ (mg $L^{-1}$) is the influent particle concentration. The solution of Eq. S-2 follows the effort of Parker and van Genuchten[103], where both the first-order removal and zero-order production in the solid phase were considered. The solution for a clean bed filtration model can be obtained simply by forcing the zero-order production coefficient to be zero in the analytical solution, which is in the following manner:

$$C(x,t) = \frac{1}{2}\exp[\frac{(v-w)x}{2D}]\text{erfc}[\frac{Rx - wt}{2(DRt)^{0.5}}] + \frac{1}{2}\exp[\frac{(v+w)x}{D}]\text{erfc}[\frac{Rx + wt}{2(DRt)^{0.5}}] \qquad \text{(S-4)}$$

$$\text{and} \quad w = (v^2 + 4J_d D)^{0.5}$$

The retardation factor R in Eq. S-2 accounts for the retardation effect arising from the sorption of nanomaterials to the porous medium. Since the R value is characteristic of the sorptive behavior of the nanomaterials to the medium surfaces, it should be independent of the pore flow velocity.

From the perspective of filtration theory, the removal of colloidal particles by the porous medium can be characterized by the removal efficiency ($\eta_0$) term, which summarizes the

removal resulted from diffusion, interception and sedimentation[149]. Following the calculation of the $\eta_0$value, the attachment removal efficiency ($\alpha$) can be obtained via:

$$\alpha = -\frac{2d_c}{3(1-\varepsilon)L\eta_0}\ln(\frac{C}{C_0}) \quad \text{(S-5)}$$

where $\varepsilon$ denotes the porosity of the medium; $d_c$ represents the diameter of the medium particle and L is the length of the porous medium bed.

**SI 6.3 Brine composition and field conditions for Scalesoftpitzer calculation:**

$$SI = \log_{10}\frac{(Ca^{2+})(CO_3^{2-})}{K_{sp}(T,P)} \quad \text{for calcite scale} \quad \text{(S-6)}$$

$$SI = \log_{10}\frac{(Ba^{2+})(SO_4^{-})}{K_{sp}(T,P)} \quad \text{for barite scale} \quad \text{(S-7)}$$

Table 6-S2 Brine composition used for Scalesoftpitzer software calculation.

| Parameters | Units | Input |
|---|---|---|
| **$Na^+$** | (mg/l) | **19,872.00** |
| **$K^+$** | (mg/l) | **500.00** |
| **$Mg^{2+}$** | (mg/l) | **54.00** |
| **$Ca^{2+}$** | (mg/l) | **6,500.00** |
| **$Sr^{2+}$** | (mg/l) | **700.00** |
| **$Ba^{2+}$** | (mg/l) | **550.00** |
| **$Fe^{2+}$** | (mg/l) | **12.00** |
| **$Zn^{2+}$** | (mg/l) | **10.00** |
| **$Cl^-$** | (mg/l) | **43,000.00** |
| **$SO_4^{2-}$** | (mg/l) | **5.00** |
| **$SiO_2$** | (mg/l) $SiO_2$ | **10.00** |
| **Alkalinity** | (mg/l) | **281.00** |
| **TDS (Measured)** | (mg/l) | **70,000.00** |
| **$CO_2$ Gas Analysis** | (%) | **1.04** |
| **$H_2S$ Gas Analysis** | (%) | **0.0283** |
| **Total $H_2S_{aq}$** | ($mgH_2S/l$) | **4.32** |
| **pH, measured (STP)** | pH | **7.16** |
| **Initial T** | (F) | **340.0** |
| **Final T** | (F) | **77.0** |
| **Initial P** | (psia) | **7,000.0** |
| **Final P** | (psia) | **14.7** |

# CHAPTER SEVEN
# CONCLUSIONS AND FUTURE WORK

In this investigation, nanomaterials containing phosphonate scale inhibitors were fabricated via various means including surfactant-assisted, silica templating and polymer based synthesis methods. The nanomaterials were prepared by firstly mixing the cations ($Ca^{2+}$ and $Zn^{2+}$) solutions with basic phosphonate solutions forming metal-phosphonate precipitates. The obtained precipitates were surface modified by surfactant coating to enhance the stability of the nanomaterial suspension at 70°C in saline conditions. Furthermore, Ca-DTPMP amorphous precipitates can be developed into a crystalline phase by diafiltration with brine solutions. The physiochemical properties of the prepared nanomaterials were investigated by various means including TEM, SEM, XRD, FT-IR and TGA analyses. The prepared nanomaterials expand their use in the delivery of phosphonate inhibitors into formation core materials for scale control. The transportability of the prepared nanomaterials through formation core materials was evaluated by laboratory column flow-through experiments. It was found that the nanomaterials generally demonstrated a good transport performance through formation porous media with increasing flow velocities. The nanomaterials transport can be enhanced with pre-flushing the core materials by a surfactant solution. The potential application of the synthesized scale inhibitor nanomaterials for oil field scale treatment has been examined by a series of laboratory squeeze simulations, in which process the inhibitor nanomaterials were loaded into the

formation materials and deposited onto the formation surfaces and slowly returned phosphonates into the synthetic brine during flow back. In terms of protection time and squeeze lifetime, the prepared nanomaterials returned phosphonates as well as conventional aqueous scale inhibitors. The developed crystalline phase Ca-DTPMP nanomaterials were able to return phosphonate inhibitors at a stable concentration over a long period of time, which is controlled by the solubility product.

As for the future work, investigation should be carried out to prepare novel inhibitor materials, capable of returning phosphonates at designated inhibitor concentrations required by production. Moreover, the transportability of the nanomaterials in consolidated core materials should be studies in that the consolidated core materials are similar to the actual formation core materials in terms of the porosity and pore size. Field applications could be started once the nanomaterials are able to transport through tight formation core materials and return phosphonates into the production water with inhibitor concentration higher than the minimum inhibitor concentration for a long period of time.

# REFERENCES


1. Cowan, J. C.; Weintritt, D. J., *Water-formed Scale Deposits*. Gulf Pub. Co.: Houston, Texas, 1976.
2. Ostroff, A. G., *Introduction to oilfield water technology*. 2nd ed.; National Association of Corrosion Engineers: Houston, Texas, 1979.
3. Freguson, R. J., Dequest organophosphorous compounds. *J. Ind. Water Treatment* 1993, 25, (2)
4. Tomson, M. B.; Oddo, J. E., *Calcium scale handbook*. 1996.
5. Chen, T.; Neville, A.; Yuan, M. D., Assessing the effect of Mg2+ on CaCO3 scale formation-bulk precipitation and surface deposition. *Journal of Crystal Growth* 2005, 275, (1-2), e1341-e1347.
6. Chen, T.; Neville, A.; Sorbie, K.; Zhong, Z., Using Synchrotron Radiation Wide-Angle X-Ray Scattering (WAXS) To Study the Inhibition Effect of DiEthyleneTriaminePenta (MethylenePhosphonic Acid) (DETPMP) on CaCO3 Scale Formation In *SPE International Oilfield Scale Symposium*, Aberdeen, UK, 2006.
7. Martinod, A.; Neville, A.; Sorbie, K.; Zhong, Z., Assessment of CaCO3 Inhibition by the Use of SXRD on a Metallic Substrate. In *NACE International*, New Orleans LA, 2008.
8. Tomson, M. B.; Kan, A. T.; Fu, G.; Shen, D.; Nasr-El-Din, H. A.; Al-Saiari, H.; Al-Thubaiti, M., Mechanistic Understanding of Rock/Phosphonate Interactions and the Effect of Metal Ions on Inhibitor Retention. *SPE 100494* 2008, 13, (3).
9. Tomson, M. B.; Kan, A. T.; Fu, G., Control of Inhibitor Squeeze via Mechanistic Understanding of Inhibitor Chemistry. *SPE J* 2006, 11, (3), 283-293.
10. Kan, A. T.; Fu, G.; Tomson, M. B., Adsorption and precipitation of an aminoalkylphosphonate onto calcite. *Journal of Colloid and Interface Science* 2005, 281, (2), 275-284.
11. Kan, A. T.; Fu, G.; Shen, D.; Al-Saiari, H.; Tomson, M. B., Enhanced inhibitor treatments with the addition of transition metal ions. *SPE 114060* 2008.
12. Wolf, N. O.; Carlberg, B. L. Reservoir scale inhibitor. 1991.
13. Jordan, M. M.; Sorbie, K. S.; Chen, P.; Armitage, P.; Hammond, P.; Taylor, K., The Design of Polymer and Phosphonate Scale Inhibitor Precipitation Treatments and the Importance of Precipitate Solubility in Extending Squeeze Lifetime. In *SPE International Symposium on Oilfield Chemistry*, Houston, Texas, 1997.
14. Tantayakom;, V.; Fogler;, H. S.; Chavadej, S., Study of Scale Inhibitor Reactions in Precipitation Squeeze Treatments In *SPE International Symposium on Oilfield Chemistry*, The Woodlands, Texas, 2005.
15. Sorbie, K. S.; Jiang, P.; Yuan, M. D.; Chen, P.; Jordan, M. M.; Todd, A. C., The Effect of pH, Calcium, and Temperature on the Adsorption of Phosphonate Inhibitor Onto Consolidated and Crushed Sandstone In *SPE Annual Technical Conference and Exhibition*, Houston, Texas, 1993.
16. Jordan, M. M.; Sorbie, K. S.; Jiang, P.; Yuan, M. D.; Todd, A. C.; Hourston, K. E., Phosphonate Scale Inhibitor Adsorption/Desorption and the Potential for Formation Damage in Reconditioned Field Core. In *SPE Formation Damage Control Symposium*, Lafayette, Louisiana, 1994.
17. Jordan, M. M.; Sorbie, K. S.; Griffin, P.; Hennessey, S.; Hourston, K. E.; Waterhouse, P., Scale Inhibitor Adsorption/Desorption vs. Precipitation: The Potential for Extending Squeeze Life While Minimising Formation Damage In *SPE European Formation Damage Conference*, The Hague, Netherlands, 1995.
18. Yuan, M. D.; Sorbie, K. S.; Todd, A. C.; Atkinson, L. M.; Riley, H.; Gurden, S., The Modelling of Adsorption and Precipitation Scale Inhibitor Squeeze Treatments in North Sea Fields In *SPE International Symposium on Oilfield Chemistry*, New Orleans, Louisiana, 1993.
19. Malandrino, A.; Yuan, M. D.; Sorbie, K. S.; Jordan, M. M., Mechanistic Study and Modelling of Precipitation Scale Inhibitor Squeeze Processes In *SPE International Symposium on Oilfield Chemistry*, San Antonio, Texas, 1995.
20. Heath, S. M.; Wylde, J. J.; Archibald, M.; Sim, M.; Collins, I. R., Development of Oil Soluble Precipitation Squeeze Technology for Application in Low and High Water Cut Wells In *SPE International Symposium on Oilfield Scale*, Aberdeen, United Kingdom, 2004.
21. McRae, J. A.; Heath, S. M.; Strachan, C.; Matthews, L.; Harris, R., Development of an Enzyme Activated, Low Temperature, Scale Inhibitor Precipitation Squeeze System. In *SPE International Symposium on Oilfield Scale*, Aberdeen, United Kingdom, 2004.
22. Shen, D.; Zhang, P.; Kan, A. T.; Fu, G.; Farrell, J.; Tomson, M. B., Control Placement of Scale Inhibitors in the Formation With Stable Ca-DTPMP Nanoparticle Suspension and its Transport in Porous Media. *SPE* 2008, 114063.

23. Song, S.; Ma, J.; Yang, J.; Cao, M.; Li, K., Selected-Control Synthesis of Metal Phosphonate Nanoparticles and Nanorods. *Inorganic Chemistry* 2005, 44, (7), 2140-2142.
24. Cheetham, A. K.; Férey, G.; Loiseau, T., Open-Framework Inorganic Materials. *Angew chem international edition* 1999, 38, (22), 3628.
25. Gong, X.; Liu, J.; Baskaran, S.; Voise, R. D.; Young, J. S., Surfactant-Assisted Processing of Carbon Nanotube/Polymer Composites. *Chemistry of Materials* 2000, 12, (4), 1049-1052.
26. Chan, H. B. S.; Budd, P. M.; Naylor, T., Control of mesostructured silica particle morphology. *Journal of Materials Chemistry* 2001, 11, (3), 951-957.
27. Puntes, V. F.; Zanchet, D.; Erdonmez, C. K.; Alivisatos, A. P., Synthesis of hcp. Co nanodisks. *Journal of the American Chemical Society* 2002, 124, (43), 12874-12880.
28. Saleh, N.; Kim, H.-J.; Phenrat, T.; Matyjaszewski, K.; Tilton, R. D.; Lowry, G. V., Ionic Strength and Composition Affect the Mobility of Surface-Modified Fe0 Nanoparticles in Water-Saturated Sand Columns. *Environmental Science & Technology* 2008, 42, (9), 3349-3355.
29. Kao, L.-H.; Hsu, T.-C., Silica template synthesis of ordered mesoporous carbon thick films with 35-nm pore size from mesophase pitch solution *Materials Letters* 2007, 62, (4-5), 695-698.
30. Zhao, X. S.; Su, F.; Yan, Q.; Guo, W.; Bao, X. Y.; Lv, L.; Zhou, Z., Templating methods for preparation of porous structures. *J. Mater. Chem.* 2006, 16, 637 - 648.
31. Shen, R.; Mu, B.; Du, P.; Liu, P., Polymeric Nanocapsule from Silica Nanoparticle@Cross-linked Polymer Nanoparticles via One-Pot Approach *Nanoscale Research Letters* 2009.
32. Fukuok, A.; Arakia, H.; Sakamotoa, Y.; Inagakib, S.; Fukushimab, Y.; Ichikawa, M., Palladium nanowires and nanoparticles in mesoporous silica templates. *Inorganica Chimica Acta* 2007, 350, (4), 371-378.
33. Chen, C.; Li, Y.; Liu, S., Fabrication of macroporous platinum using monodisperse silica nanoparticle template and its application in methanol catalytic oxidation. *Journal of Electroanalytical Chemistry* 2009, 632, (1-2), 14-19.
34. Atkins, P.; de Paula, J., *Physical Chemistry*. 7th ed.; W. H. Freeman: 2001.
35. Oddo, J. E.; Tomson, M. B., Method predicts well bore scale, corrosion. *Oil and Gas Journal* 1998 96, (23).
36. He, S.; Kan, A. T.; Tomson, M. B., Mathematical inhibitor model for barium sulfate scale control. *Langmuir* 1996, 12, (7), 1901-1905.
37. Gerbino, A. J. Quantifying the retention and release of polyphosphonates in oil and gas producing formations using surface complexation and precipitation theory. Ph.D. thesis, Rice Univeristy, Houston, TX, 1996.
38. Al-Thubaiti, M. M. New acidic ferrous and calcium phosphonate crystal phases in oilfield brine. M.S. thesis, Rice University, Houston, TX, 2003.
39. Kelland, M. A., *Production Chemicals for the Oil and Gas Industry*. CRC Press Taylor & Francis Group: Boca Raton, FL, 2009.
40. Graham, G. M.; Hennessy, A. J. B., Scale Inhibitor Surface Interactions Using Synchrotron Radiation Techniques. In *RSC Chemistry in the Oil Industry VIII Conference* Manchester, UK, 2003.
41. Graham, G. M.; Boak, L. S.; Sorbie, K. S., The Influence of Formation Calcium and Magnesium on the Effectiveness of Generically Different Barium Sulphate Oilfield Scale Inhibitors. *SPE Production & Facilities* 2003, 18, (1).
42. Burton, W. K.; Cabrera, N.; Frank, F. C., The Growth of Crystals and the Equilibrium Structure of their Surfaces. *Phil. Trans. R. Soc. Lond. A.* 1951, 243, (866).
43. Lasaga, A. C., *Kinetic Theory in the Earth Sciences*. Princeton Univeristy Press: 1989.
44. Stumm, W.; Morgan, J. J., *Aquatic Chemistry*. 3rd ed.; Wiley-Interscience: 1996.
45. Tomson, M. B.; Fu, G.; Watson, M. A.; Kan, A. T., Mechanisms of Mineral Scale Inhibition. *SPE J.* 2003, 192.
46. Sawada, K., *Crystalization processes*. John Wiley & Sons: New York, 1998.
47. Boak, L. S.; Gramham, G. M.; Sorbie, K. S., The influence of divalent cations on the performance of BaSO4 scale inhibitor species. In *SPE international symposium on oilfield chemistry :* , Houston, TX, 1999.
48. Xiao, J. A.; Kan, A. T.; Tomson, M. B., Prediction of BaSO4 Precipitation in the Presence and Absence of a Polymeric Inhibitor: Phosphino-polycarboxylic Acid. *Langmuir* 2001, 17, (15), 4668–4673.
49. Chen;, T.; Neville;, A.; Sorbie;, K.; Zhong, Z., Using Synchrotron Radiation Wide-Angle X-Ray Scattering (WAXS) To Study the Inhibition Effect of DiEthyleneTriaminePenta (MethylenePhosphonic

Acid) (DETPMP) on CaCO3 Scale Formation In *SPE International Oilfield Scale Symposium*, Aberdeen, UK, 2006.
50. Martinod;, A.; Neville;, A.; Sorbie;, K.; Zhong, Z., Assessment of CaCO3 Inhibition by the Use of SXRD on a Metallic Substrate. In *NACE International*, New Orleans LA, March 2008.
51. Amy T Kan; Gongmin Fu; Tomson, M. B., Adsorption and precipitation of an aminoalkylphosphonate onto calcite. *Journal of Colloid and Interface Science* 2005, 281, (2), 275-284.
52. Mason B. Tomson; Amy T. Kan; Gongmin Fu, D. S.; Nasr-El-Din;, H. A.; Hamad Al-Saiari; Musaed Al-Thubaiti, Mechanistic Understanding of Rock/Phosphonate Interactions and the Effect of Metal Ions on Inhibitor Retention. *SPE 100494* 2008, 13, (3).
53. Mason B. Tomson; Amy T. Kan; Fu, G., Control of Inhibitor Squeeze via Mechanistic Understanding of Inhibitor Chemistry. *SPE J* 2006, 11, (3), 283-293.
54. Yuan, M. D., The latest developments in scale control in oilfield. In *The science and technology of industrial*, Amjad, Z., Ed. CRC Press: Brecksville, Ohio, USA 2010.
55. Schwarzenbach, R. P.; Gschwend, P. M.; Imboden, D. M., *Environmental Organic Chemistry*. Hohn Wiley & Sons.: Hoboken, NJ, 2003.
56. Sawyer, C.; McCarty, P.; Parkin, P., *Chemistry for Environmental Engineering and Science* Mcgraw-Hill: New York, NY, 2003.
57. Kan;, A. T.; Gongmin Fu; Shen;, D.; Al-Saiari;, H.; Tomson, M. B., Enhanced inhibitor treatments with the addition of transition metal ions. *SPE 114060* 2008.
58. Kan, A. T.; Oddo, J. E.; Tomson, M. B., Formation of Two Calcium Diethylenetriaminepentakis(methylene phosphonic acid) Precipitates and Their Physical Chemical Properties. *Langmuir* 1994, 10, (5), 1450-1455.
59. Tomson, M. B.; Kan, A. T.; Oddo, J. E., Acid/Base and Metal Complex Solution Chemistry of the Polyphosphonate DTPMP versus Temperature and Ionic Strength. *Langmuir* 1994, 10, (5), 1442-1449.
60. Oddo, J.; Tomson, M. B. *Software package for predictive saturation indices for caco3 and common sulfate scales in gas and oil field systems* Chicaog, IL, 1994.
61. Kan, A. T.; Wu, X.; Fu, G.; Tomson, M. B., Validation of Scale Prediction Algorithms at Oilfield Conditions. In *SPE International Symposium on Oilfield Chemistry*, Woodlands, TX, USA. , 2005.
62. Kan, A. T.; Tomson, M. B., Scale prediction for oil and gas production. In *SPE International Oil and Gas Conference and Exhibition*, Beijing, China, 2010.
63. Pitzer, K. S., *Molecular Structure and Statistical Thermodynamics: Selected Papers of Kenneth S. Pitzer*. World Scientific Publishing Co. Ptz. Ltd.: 1993.
64. Peng, D. Y.; Robinson, D. B., A new two-constant equation of state. *Industrial and Engineering Chemistry: Fundamentals* 1976, 15, 59–64.
65. He, S.; Morse, J. W., The carbonic acid system and calcite solubility in aqueous Na-K-Ca-Mg-Cl-SO4 solutions from 0 to 90°C *Geochimica et Cosmochimica Acta* 1993, 57, (15), 3533-3554.
66. Kan, A. T.; Fu, G.; Tomson, M. B., Effect of Methanol on Carbonate Equilibrium and Calcite Solubility in a Gas/Methanol/Water/Salt Mixed System. *Langmuir* 2002, 18, (25), 9713–9725.
67. Steber, J.; Wierich, P., Properties of hydroxyethane diphosphonate affecting its environmental fate: degradability, sludge adsorption, mobility in soils, and bioconcentration. *Chemosphere* 1986, 15, (7), 929-945.
68. Steber, J.; Wierich, P., Properties of aminotris(methylenephosphonate) affecting its environmental fate: degradability, sludge adsorption, mobility in soils, and bioconcentration. *Chemosphere* 1987, 16, (6), 1323-1337.
69. Nowack, B.; Stone, A. T., Degradation of Nitrilotris(methylenephosphonic Acid) and Related (Amino)Phosphonate Chelating Agents in the Presence of Manganese and Molecular Oxygen. *Environ. Sci. Technol.* 2000, 34, (22), 4759–4765.
70. Nowack, B., The behavior of phosphonates in wastewater treatment plants of Switzerland. *Water Research* 1998, 32, (4), 1271-1279.
71. Tikhonova, L. I., *Russ. J. Inorg. Chem.* 1968, 13, 1384.
72. Bear, J., *Hydraulics of Groundwater.* McGraw-Hill Book. Company: New York, New York,, 1979. .
73. Charbeneau, R. J., *Groundwater hydraulics and pollutant transport*. Prentice Hall: 1999.
74. Bedient, P. B., *Ground water contamination: Transport and remediation* 2nd ed.; Prentice Hall PTR: 1999.
75. Miller, C. T.; Weber, W. J. J., Modeling organic contaminant partitioning in ground-water

systems. *Ground Water* 1984, 22, (5).
76. Pedit , J. A.; Miller, C. T., Heterogeneous Sorption Processes in Subsurface Systems. 1 Model Formulations and Applications. *Envlron. Scl. Technol.* 1994, 28, 2094-2104.
77. Clark, G. L. Flow rate effects on the sorption of methylated benzenes in saturated aquifer materials. Ph.D. dissertation, Rice University, Houston TX, 1990.
78. Chu, Y.; Jin, Y.; Yates, M. V., Virus Transport through Saturated Sand Columns as Affected by Different Buffer Solutions. *J Environ Qual.* 2000, 29, 1103-1110.
79. Jin, Y.; Yates, M. V.; Thompson, S. S.; Jury, M. A., Sorption of Viruses during Flow through Saturated Sand Columns. *Environ. Sci. Technol.* 1997, 31, (2), 548–555.
80. Ryan, J. N.; Elimelech, M., Colloid mobilization and transport in groundwater. *Colloids and Surfaces A: Physicochemical and Engineering Aspects* 1996, 107, 1-56.
81. de Jonge, L. W.; Kjaergaard, C.; Moldrup, P., Colloids and colloid-facilitated transport of contaminants in soils: An introduction. *Vadose Zone Journal* 2004, 3, (2), 321-3258.
82. Derjaguin, B.; Landau, L., Theory of the stability of strongly charged lyophobic sols and of the adhesion of strongly charged particles in solutions of electrolytes. *Acta Physico Chemica URSS* 1941, 14, 633.
83. Verwey, E. J. W.; Overbeek, J. T. G., *Theory of the stability of lyophobic colloids*. Elsevier: Amsterdam, 1948.
84. Kretzschmar, R.; Borkovec, M.; Grolimund, D.; Elimelech, M., Mobile Subsurface Colloids and Their Role in Contaminant Transport. *Advances in Agronomy* 1999, 66, 121-193
85. Ruckenstein, E.; Prieve, D. C., Adsorption and desorption of particles and their chromatographic separation. *AIChE Journal* 1976, 22, (2), 276 - 283.
86. J.C. Parker, M. T. v. G., *Determining Transport Parameters from Labotoary and Field Tracer Experiments*. Blacksburg, VA, Oct., 1984; Vol. Bulletin 84-3.
87. Kreft A.; A., Z., Physical meaning of dispersion-equation and its solutions for different initial boundary conditions. *Chemical. Engineering Science* 1978, 33, (11), 1471–1480.
88. Batu, V., *Applied Flow and Solute Transport Modeling in Aquifers: Fundamental Principles and Analytical and Numerical Methods*. Boca Raton, FL, 2006.
89. Kretzschmar, R.; Sticher, H., Transport of Humic-Coated Iron Oxide Colloids in a Sandy Soil:  Influence of Ca2+ and Trace Metals. *Environmental Science & Technology* 1997, 31, (12), 3497-3504.
90. He, F.; Zhang, F.; Qian, T.; Zhao, D., Transport of carboxymethyl cellulose stabilized iron nanoparticles in porous media: Column experiments and modeling. *Journal of Colloid and Interface Science* 2009, 334, (1), 96-102
91. Kretzschmar, R.; Borkovec, M.; Grolimund, D.; Elimelech, M., Mobile Subsurface Colloids and Their Role in Contaminant Transport *Advances in Agronomy* 1999, 66, 121-193.
92. Yao, K.; Habibian, M. T.; O'Melia, C. R., Water and waste water filtration. Concepts and applications. *Environmental Science & Technology* 1971, 5, (11), 1105-1112.
93. Tufenkji, N.; Elimelech, M., Correlation equation for predicting single-collector efficiency in physicochemical filtration in saturated porous media. *Environ. Sci. Technol.* 2004, 38, 529.
94. Zhang, P.; Shen, D.; Fan, C.; Kan, A. T.; Tomson, M. B., Surfactant-Assisted Synthesis of Metal Phosphonate Inhibitor Nanoparticles and Their Transport in Porous Media. In *SPE International Symposium on Oilfield Chemistry,* , The Woodlands, Texas, 2009.
95. Lecoanet, H. F.; Wiesner, M. R., Velocity Effects on Fullerene and Oxide Nanoparticle Deposition in Porous Media. *Environ. Sci. Technol.* 2004, 38, (16), 4377-4382.
96. Patterson, A. L., The Scherrer Formula for X-Ray Particle Size Determination. *Phys. Rev.* 1939, 56, (10), 978 - 982.
97. Zhang, X. J.; Ma, T. Y.; Yuan, Z. Y., Titania–phosphonate hybrid porous materials: preparation, photocatalytic activity and heavy metal ion adsorption. *J. Mater. chem.* 2008, 18, 2003-2010.
98. Mullin, J. W., *Crystallization*. Butterworth-Heinemann: Liacre Houston, Jordan Hill, OXford, 2001.
99. Rosen, M. J., *Surfactants and Interfacial Phenomena*. 3rd ed.; John Wiley & Sons, Inc.: Hooboken, New Jersey, 2004.
100. Stumm;, W.; Morgan, J. J., *Aquatic Chemistry*. 3rd ed.; Wiley-Interscience: 1996.
101. Kanel, S. R.; Nepal, D.; Manning, B.; Choi, H., Transport of surface-modified iron nanoparticle in porous media and application to arsenic(III) remediation. *Journal of Nanoparticle Research* 2007, 9, (5),

725.
102. Ren, T.; Yuan, Z.; Su, B., Surfactant-assisted preparation of hollow microspheres of mesoporous TiO2. *Chemical Physics Letters* 2003, 374, (1), 170-175.
103. Parker, J. C.; van Genuchten, M. T., *Determining Transport Parameters from Labotoary and Field Tracer Experiments*. Blacksburg, VA, 1984; Vol. Bulletin 84-3.
104. Kretzschmar, R.; Sticher, H., Transport of humic-coated iron oxide colloids in a sandy soil: Influence of Ca2+ and trace metals. *Environ. Sci. Technol.* 1997, 31, 3497.
105. Online calculator http://www.colorado.edu/ceae/environmental/ryan/cven6414/eta.xls.
106. Kan, A. T.; Yan, L.; Bedient, P. B.; Oddo, J. E.; Tomson, M. B., Sorption and Fate of Phosphonate Scale Inhibitors in the Sandstone Reservoir: Studied by Laboratory Apparatus With Core Material, SPE 21714. In *SPE Production Operations Symposium*, Oklahoma City, Oklahoma, 1991.
107. Stalker, R.; Graham, G. M.; Oliphant, D.; Smillie, M., Potential Application of Viscosified Treatments For Improved Bullhead Scale Inhibitor Placement in Long Horizontal Wells - A Theoretical and Laboratory Examination In *SPE International Symposium on Oilfield Scale*, Society of Petroleum Engineers Aberdeen, United Kingdom, 2004.
108. James, J. S.; Frigo, D. M.; Townsend, M. M.; Graham, G. M.; Wahid, F.; Heath, S. M., Application of a Fully Viscosified Scale Squeeze for Improved Placement in Horizontal Wells. In *SPE International Symposium on Oilfield Scale*, Society of Petroleum Engineers Aberdeen, United Kingdom, 2005.
109. Miles, A. F.; Vikane, O.; Healey, D. S.; Collins, I. R.; Saeten, J.; Bourne, H. M.; Smith, H. M., Field Experiences Using 'Oil Soluble' Non-Aqueous Scale Inhibitor Delivery Systems, SPE 87431. In *SPE International Symposium on Oilfield Scale*, Society of Petroleum Engineers Aberdeen, United Kingdom, 2004.
110. Guan, H.; Sorbie, K. S.; Yuan, M.; Smith, K., Non-Aqueous Squeeze Treatments in Sandstones: Core Flood Studies and Modeling, Paper 04386. In *Corrosion*, NACE International: New Orleans, LA, 2004.
111. Jordan, M.; Sørhaug, E.; Elrick, M.; Marlow, D., The Development of a Scale Management and Monitoring Program for a High-Temperature Oil Field During the Production-Decline Phase of the Life Cycle. In *International Symposium on Oilfield Chemistry*, Society of Petroleum Engineers: Houston, Texas, 2007.
112. Vazquez, O.; Mackay, E. J.; Sorbie, K. S., Modelling of Nonaqueous and Aqueous Scale-Inhibitor Squeeze Treatments. In *International Symposium on Oilfield Chemistry*, Society of Petroleum Engineers: Houston, Texas, 2007.
113. Collins, I., scale management and risk assessment for deepwater development. *World Oil* 2003, 62.
114. Jordan, M. M.; Mackay, E. J., Scale control in deepwater fields: use an interdisciplinary approach to control scale. *World Oil* 2005.
115. Zhang, P.; Shen, D.; Fan, C.; Kan, A. T.; Tomson, M. B., Surfactant-Assisted Synthesis of Metal Phosphonate Inhibitor Nanoparticles and Their Transport in Porous Media. *SPE J.* 2009, in press.
116. Kan, A. T.; Fu, G.; Shen, D.; Al-Saiari, H.; Tomson, M. B., Enhanced Scale-Inhibitor Treatments With the Addition of Zinc. *SPE J.* 2009, 14, (4), 617-626.
117. Cotton, F. A.; Murillo, C. A.; Bochmann, M., *Advanced Inorganic Chemistry*. 1999.
118. Popov, K.; Ronkkomaki, H.; Lajunen, L. H., Critical evaluation of stability constants of phosphonic acids. *Pure & Appl. Chem.* 2001, 73, (10), 1641.
119. Sawada, K.; Araki, T.; Suzuki, T., Complex formation of amino polyphosphonates. 1. Potentiometric and nuclear magnetic resonance studies of nitrilotris(methylenephosphonato) complexes of the alkaline-earth-metal ions. *Inorg. Chem.* 1987, 26, (8), 1199–1204.
120. Sawada, K.; Araki, T.; Suzuki, T., Complex formation of aminopolyphosphonates. 2. Stability and structure of nitrilotris(methylenephosphonato) complexes of the divalent transition metal ions in aqueous solution. *Inorg. Chem.* 1989, 28, (13), 2687–2688.
121. Motekaitis, R. J.; Murase, I.; Martell, A. E., Equilibriums of ethylenediamine-N,N,N',N'-tetrakis(methylenephosphonic) acid with copper(II), nickel(II), cobalt(II), zinc(II), magnesium(II), calcium(II), and iron(III) ions in aqueous solution. *Inorg. Chem.* 1976, 15, (9), 2303–2306.
122. Rossen, W. R., Foams in enhanced oil recovery. In *Foams: Theory, Measurements and Applications*, Prud'homme, R. K.; Khan, S., Eds. Marcel Dekker, New York, 1996.
123. Vazquez, O.; Mackay, E. J.; Al Shuaili, K.; Sorbie, K. S.; Jordan, M. M., Modeling a Surfactant

Preflush with Non-Aqueous and Aqueous Scale Inhibitor Squeeze Treatments. In *Europec/EAGE Conference and Exhibition*, Society of Petroleum Engineers: Rome, Italy, 2008.
124. Veeramasunenia, S.; Yalamanchili, M. R.; Miller, J. D., Measurement of Interaction Forces between Silica and α-Alumina by Atomic Force Microscopy. *Journal of Colloid and Interface Science* 1996, 184, (2), 594-600
125. Clark, M. M., *Transport Modeling for Environmental Engineers and Scientists*. John Wiley & Sons, Inc: New York, NY, 1996.
126. Rodier, E.; Dodds, J. A., An experimental study of the transport and capture of colloids in porous media by a chromatographic technique. . *Colloids Surfaces A: Physicochem. Eng. Aspects* 1993, 73, 77–87.
127. Saleh, N.; Sirk, K.; Liu, Y.; Phenrat, T.; Dufour, B.; Matyjaszewski, K.; Tilton, R. D.; Lowry, G. V., Surface modifications enhance nanoiron transport and NAPL targeting in saturated porous media. *Environ. Eng. Sci.* 2007, 24, 45.
128. He, F.; Zhao, D.; Liu, J.; Roberts, C. B., Stabilization of Fe-Pd nanoparticles with sodium carboxymethyl cellulose for enhanced transport and dechlorination of trichloroethylene in soil and groundwater. *Ind. Eng. Chem. Res.* 2007, 46, 29.
129. Chou, L.; Garrels, R. M.; Wollast, R., Comparative study of the kinetics and mechanisms of dissolution of carbonate minerals. *Chem. Geol.* 1989, 78, 269.
130. Brady, P. V.; Walther, J. V., Kinetics of quartz dissolution at low temperatures. *Chemical Geology* 1990, 82, 253.
131. Pokrovsky, O. S.; Schott, J.; Thomas, F., Dolomite surface speciation and reactivity in aquatic systems *Geochimica et Cosmochimica Acta* 1999, 63, (19-20), 3133-3143
132. Clausen, L.; Fabricius, I.; Madsen, L., Adsorption of pesticides onto quartz, calcite, kaolinite, and α-alumina. *Journal of environmental quality* 2001, 30, 846-857.
133. Behra, P.; Lecarme-Théobaldb, É.; Buenoc, M.; Ehrhardt, J. J., Sorption of tributyltin onto a natural quartz sand *Journal of Colloid and Interface Science* 2003, 263, (1).
134. Hoskin, D. H.; Rollmann, D. L.; Shoemaker, G. L.; Schmitt, K. D. Use of polyalkoxy sulfonate surfactants for inhibition of scale formation 1986.
135. Tantayakom, V.; Fogler, H. S.; Chavadej, S., Study of Scale Inhibitor Reactions in Precipitation Squeeze Treatments In *SPE International Symposium on Oilfield Chemistry*, The Woodlands, Texas, 2005.
136. Zhang, P.; Kan, A. T.; Fan, C.; Work, S.; YU, J.; Lu, H.; Al-Saiari, H. A.; Tomson, M. B. In *Silica-Templated Synthesis of Zinc-DTPMP Nanoparticles, their transport in carbonate and sandstone porous media and sale inhibition SPE 130639*, SPE International Conference on Oilfield Scale, Aberdeen, UK, 2010; Aberdeen, UK, 2010.
137. Reddy, M. M.; Nancollas, G. H., The crystallization of calcium carbonate: IV. The effect of magnesium, strontium and sulfate ions *Journal of Crystal Growth* 1976, 35, (1), 33-38
138. Koutsoukos, P.; Amjad, Z.; Tomson, M. B.; Nancollas, G. H., Crystallization of calcium phosphates. A constant composition study *Journal of the American Chemical Society* 1980, 102, (5).
139. Lowenstam, H. A.; Weiner, S., Transformation of Amorphous Calcium Phosphate to Crystalline Dahillite in the Radular Teeth of Chitons *Science* 1985, 227, 51 - 53.
140. Christoffersen, J.; Christoffersen, M. R.; Kibalczyc, W.; Andersen, F. A., A contribution to the understanding of the formation of calcium phosphates *Journal of Crystal Growth* 1989, 94, (3).
141. Mahamid, J.; Sharir, A.; Addadi, L.; Weiner, S., Amorphous calcium phosphate is a major component of the forming fin bones of zebrafish: Indications for an amorphous precursor phase. *PNAS* 2008, 105, (12748-12753 ).
142. Hunter, R. J., *Foundations of colloid science*. Oxford University Press: New York, 2001.
143. Kan, A. T.; Fu, G.; Tomson, M. B., Prediction of Scale Inhibitor Squeeze and Return in Calcite-Bearing Formation. In *SPE International Symposium on Oilfield Chemistry*, The Woodlands, Texas, 2005.
144. Cabeza, A.; Yang, X. Q.; Sharma, C. V. K.; Aranda, M. A. G.; Bruque, S.; Clearfield, A., Complexes Formed between Nitrilotris(methylenephosphonic acid) and M2+ Transition Metals: Isostructural Organic−Inorganic Hybrids. *Inorg. Chem.* 2002, 41, (9), 2325–2333.
145. Odobel, F.; Bujoli, B.; Massiot, D., Zirconium Phosphonate Frameworks Covalently Pillared with a Bipyridine Moiety. *Chem. Mater.* 2001, 13, (1), 163–173.
146. Dean, J. A., *Lange's Handbook of Chemistry*. 15th ed.; McGraw-Hill 1999.
147. Billo, E. J., *Excel for Chemists: A Comprehensive Guide*. 2nd ed.; John Willey & Sons, Inc.: 2001.
148. Hoopes, J. A.; Harleman, D. R. F., Dispersion in Radial Flow from a Recharge Well. *Journal of Geophysical Research* 1967 72, 3595.

149. Tufenkji, N.; Elimelech, M., Correlation Equation for Predicting Single-Collector Efficiency in Physicochemical Filtration in Saturated Porous Media. *Environmental Science & Technology* 2004, 38, (2), 529-536.
150. Lecoanet, H. F.; Bottero, J. Y.; Wiesner, M. R., Laboratory Assessment of the Mobility of Nanomaterials in Porous Media. *Environ. Sci. Technol.* 2004, 38, 5164.
151. Li, Y.; Wang, Y.; Pennell, K. D.; Abriola, L. M., Investigation of the Transport and Deposition of Fullerene (C60) Nanoparticles in Quartz Sands under Varying Flow Conditions. *Environ. Sci. Technol.* 2008, 42, (19), 7174–7180.
152. Zhuang, J.; Jin, Y.; Flury, M., Comparison of hanford colloids and kaolinite transport in porous media *Vadose Zone* 2004, 3, 395-402.
153. Liu, D.; Johnson, P. R.; Elimelech, M., Colloid deposition dynamics in flow-through porous media: Role of electrolyte concentration. *Environ. Sci. Technol.* 1995, 29, 2963.
154. He, F.; Zhang, M.; Qian, T.; Zhao, D., Transport of carboxymethyl cellulose stabilized iron nanoparticles in porous media: Column experiments and modeling *Journal of Colloid and Interface Science* 2009, 334, (1).
155. Shani, C.; Weisbrod, N.; Yakirevich, A., Colloid transport through saturated sand columns: Influence of physical and chemical surface properties on deposition *Colloids and Surfaces A: Physicochemical and Engineering Aspects* 2008, 316, 142-150.
156. Derjaguina, B.; Landau, L., Theory of the stability of strongly charged lyophobic sols and of the adhesion of strongly charged particles in solutions of electrolytes *Progress in Surface Science* 1993, 43, (1-4), 30-59.
157. Verwey, E. J. W., Theory of the Stability of Lyophobic Colloids. *J. Phys. Chem.* 1947, 51, (3), 631–636.
158. Evans, D. F.; Wennerström, H., *The Colloidal Domain: Where Physics, Chemistry, Biology, and Technology Meet (Advances in Interfacial Engineering)*. 2nd ed.; Wiley-VCH: 1999.
159. Torkzaban, S.; Bradford, S. A.; Walker, S. L., Resolving the Coupled Effects of Hydrodynamics and DLVO Forces on Colloid Attachment in Porous Media. *Langmuir* 2007, 23, (19), 9652–9660.
160. Redman, J. A.; Walker, S. L.; Elimelech, M., Bacterial Adhesion and Transport in Porous Media: Role of the Secondary Energy Minimum. *Environ. Sci. Technol.* 2004, 38, (6), 1777–1785.
161. Bergendahl, J.; Grasso, D., Prediction of colloid detachment in a model porous media: hydrodynamics *Chemical Engineering Science* 2000, 55, (9), 1523-1532
162. Zhang, P.; Fan, C.; Lu, H.; Kan, A. T.; Tomson, M. B., Synthesis of the crystalline phase silica-based Ca-phosphonate nanomaterials and their transport in carbonate and sandstone porous media. *Ind. Eng. Chem. Res.* 2010, under review.
163. Tufenkji, N.; Elimelech, M., Deviation from the Classical Colloid Filtration Theory in the Presence of Repulsive DLVO Interactions. *Langmuir* 2004, 20, (25), 10818–10828.
164. Marouf, R.; Marouf-Khelifa, K.; Schott, J.; Khelifa, A., Zeta potential study of thermally treated dolomite samples in electrolyte solutions *Microporous and Mesoporous Materials* 2009, 122, (1-3), 99-104.
165. Alkan, M.; Demirbaş, Ö.; Doğan, M., Electrokinetic properties of sepiolite suspensions in different electrolyte media *Journal of Colloid and Interface Science* 2005, 281, (1), 240-248.
166. Kaya, A.; Yukselen, Y., Zeta potential of soils with surfactants and its relevance to electrokinetic remediation. *Journal of Hazardous Materials* 2005, 120, (1-3), 119-126
167. Yalçın, T.; Alemdar, A.; Ece, Ö. I.; Güngör, N., The viscosity and zeta potential of bentonite dispersions in presence of anionic surfactants *Materials Letters* 2002, 57, (2), 420-424
168. Derjaguin, B.; Landau, L., Theory of the stability of strongly charged lyophobic sols and of the adhesion of strongly charged particles in solutions of electrolytes. *Acta Physico Chemica URSS* 1941, 14, 633.
169. Adamson, A. W.; Gast, A. P., *Physical Chemistry of Surfaces*. 6th ed.; 1997.
170. Hogg, R.; Healy, T. W.; Fuerstenau, D. W., Mutual coagulation of colloidal dispersions. *Trans. Faraday Soc.* 1966, 62, 1638 - 1651.
171. Uematsu, M.; GFranck, E. U., Statci dielectri constants of water and steam. *J. Phys. Chem. Ref. Data* 1980, 9, (4).
172. Elimelech, M.; C.R., O. M., Effect of Particle Size on Collision Efficiency in the Deposition of Brownian Particles with Electrostatic Energy Barriers. *Langmuir* 1990, 6, 1153-1163.
173. Gregory, J., Approximate expressions for retarded van der waals interaction *Journal of Colloid*

*and Interface Science* 1981, 83, (1), 138-145
174. Schenkel, J. H.; Kitchener, J. A., A test of the Derjaguin-Verwey-Overbeek theory with a colloidal suspension. *Trans. Faraday Soc.* 1960, 56, 161 - 173.
175. Israelachvili, J., *Intermolecular and Surface Forces*. 2nd ed.; Academic Press Inc.: , . San Diego, CA, 1992.
176. Cardenas, M.; Valle-Delgado, J. J.; Hamit, J.; Rutland, M. W.; Arnebrant, T., Interactions of Hydroxyapatite Surfaces: Conditioning Films of Human Whole Saliva. *Langmuir* 2008, 24, (14), 7262–7268.
177. Lyklema, J., *Fundamentals of Interface and Colloid Science*. Academic Press: London, 1995; Vol. 2.
178. Cavaliera, K.; Larché, F., Effects of water on the rheological properties of calcite suspensions in dioctylphthalate *Colloids and Surfaces A: Physicochemical and Engineering Aspects* 2002, 197, (1-3), 173-181
179. Kuznar, Z. A.; Elimelech, M., Adhesion kinetics of viable Cryptosporidium parvum oocysts to quartz surfaces. *Environ. Sci. Technol.* 2004, 38, 6839-6845.
180. Hahn, M. W.; Abadzic, D.; O'Melia, C. R., Aquasols: On the Role of Secondary Minima. *Environ. Sci. Technol.* 2004, 38, (22), 5915–5924.
181. Lasaga, A., *Kinetic Theory in the Earth Sciences*. Princeton University Press: Princeton, NJ, 1998.
182. He, S.; Kan, A. T.; Tomson, M. B., Mathematical Inhibitor Model for Barium Sulfate Scale Control. *Langmuir* 1996, 12, (7), 1901–1905.